creative commons
COMMONS DEED

저작자표시-비영리-변경금지 2.0 대한민국

이용자는 아래의 조건을 따르는 경우에 한하여 자유롭게

- 이 저작물을 복제, 배포, 전송, 전시, 공연 및 방송할 수 있습니다.

다음과 같은 조건을 따라야 합니다:

저작자표시. 귀하는 원저작자를 표시하여야 합니다.

비영리. 귀하는 이 저작물을 영리 목적으로 이용할 수 없습니다.

변경금지. 귀하는 이 저작물을 개작, 변형 또는 가공할 수 없습니다.

- 귀하는, 이 저작물의 재이용이나 배포의 경우, 이 저작물에 적용된 이용허락조건을 명확하게 나타내어야 합니다.
- 저작권자로부터 별도의 허가를 받으면 이러한 조건들은 적용되지 않습니다.

저작권법에 따른 이용자의 권리는 위의 내용에 의하여 영향을 받지 않습니다.

이것은 이용허락규약(Legal Code)을 이해하기 쉽게 요약한 것입니다.

Disclaimer

dCollection

공학박사 학위논문

Design methodology and validation of low carbon energy system:

LNG, Hydrogen, and Carbon dioxide

저탄소 에너지 시스템의 설계 방법론과 검증:

액화천연가스, 수소, 이산화탄소

2022 년 8 월

서울대학교 대학원

조선해양공학과

정 병 찬

Design methodology and validation of low carbon energy system:

LNG, Hydrogen, and Carbon dioxide

저탄소 에너지 시스템의 설계 방법론과 검증:

액화천연가스, 수소, 이산화탄소

지도 교수 임 영 섭

이 논문을 공학박사 학위논문으로 제출함

2022 년 8 월

서울대학교 대학원

조선해양공학과

정 병 찬

정병찬의 공학박사 학위논문을 인준함

2022 년 8 월

위 원 장 서 유 택 (인)

부위원장 임 영 섭 (인)

위 원 노 명 일 (인)

위 원 이 웅 (인)

위 원 나 종 걸 (인)

Abstract

Design methodology and validation of low carbon energy system: LNG, Hydrogen, and Carbon dioxide

Byungchan Jung
Department of Naval Architecture and Ocean Engineering
The Graduate School
Seoul National University

This thesis deals with the design methodology and validation of the energy industry. Because of securing sustainable energy resources and mitigating climate change, an energy paradigm shift from fossil fuel to renewable energy is ongoing. As an intermittent energy transition, this thesis focused on developing proper numerical simulation models for predicting the transport phenomena that occur in the low carbon energy system from the perspective of chemical process system engineering. Each of the developed models was validated with the measured data and applied to the development of a design methodology for its system. It included a 1D LNG weathering prediction model, a 0D dynamic simulation model of a hydrogen refueling system, and a 3D CFD model of the CO_2RR flow pattern.

In an LNG storage tank, the composition of LNG changes with time owing to the generation of boil-off gas (BOG), which is called LNG weathering. It is a crucial characteristic in designing the entire LNG value chain. Because LNG exists in a non-equilibrium state in the tank, to analyze this phenomenon, we performed a long-term

(50 days) experiment in a large-scale tank (50 m^3) containing nitrogen and hydrocarbons, under isobaric operation. And this study proposes a 1D prediction model of LNG weathering, which excludes vapor phase modeling. Because the measured vapor phase temperature cannot represent the entire vapor phase owing to thermal stratification, it is difficult to quantify the heat transfer and thermodynamic equilibrium at the interface rigorously in a large-scale tank. To facilitate this approach, the net mass transfer was calculated using an empirical vapor-liquid equilibrium constant derived from the LNG terminal and the statistical rate theory which converts a temperature term into pressure, and the net heat transfer at the interface was also applied. The developed model was validated with experimental data and showed good agreement with experiments. Through the developed model, we found deviations of the conventional approach and proposes a design methodology to apply the prediction model to different scenarios using the BOG generation parameter (c) and equilibrium constant (K_{N_2}).

The need for nationwide distribution of optimized refueling facilities and associated infrastructure has emerged to cope with the increase in demand for fuel cell electric vehicles. Thus, this study investigated the complicated interdependency of the design variables of the main HRS components. To evaluate the performance of the HRS, we developed a 0D dynamic simulation model covering the whole sequence of the HRS which includes hydrogen filling tank and pressure recovery of buffer storage tanks. The developed model was validated by actual HRS operating data in South Korea. And this study proposed a novel design methodology for reducing CAPEX and OPEX considering all actual constraints. First, with pre-defined HRS capacity and vehicle, a compressor is sized concerning fill-up demand

and available pressure of hydrogen source and it can operate during refueling to reduce the size of a buffer storage volume. Next, a buffer storage system is designed with 5 variables to reduce energy consumption and complete back-to-back filling. Because the higher pressure tank is recovered to some extent in the back-to-back filling scenario depending on the performance of the compressor, it is required to focus on increasing the size volume of the lower pressure level.

Electrochemical conversion of CO_2 to valuable chemicals is a sustainable method of producing chemicals with reducing greenhouse gases and a potential solution for resolving renewable energy supply as well as demand mismatch. A 3D CFD model was developed to quantify the effect of the flow pattern on mass transfer for improving the production rate of CO. We experimentally measured the production rate of CO in a large-scale electrochemical CO_2 reduction reactor with the flow pattern designed by CFD and also experimented to investigate other extrinsic properties that facilitate the mass transfer rate by varying pH and interface. This result shows that the convective mass transfer improves the production rate, and we proposed a general guideline for the flow pattern design for a large-scale electrochemical CO_2 reduction reactor that maximizes convective mass transfer through a GDE and keeps flow in the reactor uniform.

Keyword: Energy, Liquefied natural gas, Hydrogen, Carbon dioxide, Modeling, Design methodology, Validation

Student Number: 2016-21139

Contents

Abstract ..... **i**
Contents ..... **iv**
List of Tables ..... **vi**
List of Figures ..... **vii**
Chapter 1. Introduction **1**
1.1. Research subject 1
1.2. Research background 4
1.2.1. LNG storage 4
1.2.2. Hydrogen distribution 8
1.2.3. CO_2 conversion 12
1.3. Research objective 16
Chapter 2. LNG Storage **19**
2.1. Experimental apparatus and procedures 19
2.2. Computational model description 23
2.2.1. Model assumptions and overall algorithm 23
2.2.2. Heat transfer modeling 26
2.2.3. Boil-off modeling 29
2.2.4. Mass and energy balance 30
2.2.5. Equation of state for properties 32
2.3. Results and discussions 34
2.3.1. Experimental validation 34
2.3.2. Simulation study 40
2.3.3. Sensitivity analysis of parameter 45
2.3.4. Comparison of conventional and developed model 48
2.4. Conclusion 49
Chapter 3. Hydrogen Distribution **50**
3.1. Computational model description 50
3.2. Model validation using operational data 54
3.3. Development of design methodology 58

3.3.1. Overall design methodology of HRS 58
3.3.2. Design variables of buffer storage system 60
3.4. Investigation of design procedure 63
3.4.1. Compressor design 63
3.4.2. Number of stages and initial pressure 66
3.4.3. Sizing volume of buffer tank for one vehicle filling 68
3.4.4. Sizing volume of buffer tank for back-to-back filling 73
3.5. Conclusion 75
Chapter 4. CO_2 Conversion 76
4.1. CFD modeling 76
4.1.1. Mesh generation 76
4.1.2. Governing equations 78
4.1.3. Boundary conditions 80
4.1.4. Solution methodology 81
4.1.5. Design concept 82
4.1.6. Design case studies 85
4.1.7. Design criteria and case study selection 90
4.1.8. Scale-up effect on $\boldsymbol{u_{avg}}$ 98
4.1.9. Summary of CFD simulation 101
4.2. Experimental investigation 104
4.2.1. Experiments setup 104
4.2.2. Flow pattern investigation 106
4.2.3. Investigation of extrinsic properties 109
4.2.4. Experimental verification 113
4.3. Conclusion 116
Chapter 5. Concluding remarks 117
5.1. Summary of contributions 117
5.2. Limitations and future works 120
Nomenclature 122
References 126
Abstract in Korean (국문초록) 136

List of Tables

Table 3-1. Simulation assumptions. 65
Table 3-2. Minimum required volume and energy consumption depending on compressor operation during refueling. 69
Table 4-1. Analysis of pressure difference. 94
Table 4-2. Summary of CFD simulation results. 101

List of Figures

Figure 1-1. Research scope of low carbon energy system. 3
Figure 1-2. Schematic diagram of hydrogen refueling station. 9
Figure 2-1. Process flow diagram of LNG weathering observation system.....21
Figure 2-2. Changes in tank pressure over time in experiment. 22
Figure 2-3. Schematic model algorithm for calculating BOR and BOG composition variation over time. 25
Figure 2-4. Schematic of mass and heat transfer in tank.....28
Figure 2-5. Profiles of experimental data and simulation results (a) LNG temperature (b) level. 36
Figure 2-6. Profiles of normalized experimental data and simulation results. 38
Figure 2-7. Profiles of experimental LNG compositions with simulation results...39
Figure 2-8. Profiles of normalized evaporation rate for each component. 43
Figure 2-9. Comparison of vapor compositions with respect to presence or absence of NG modeling.....43
Figure 2-10. Profile of measured temperature difference between LNG and NG zones. 44
Figure 2-11. Comparison of removed energy from LNG with quantified BOG enthalpy at initial point.....44
Figure 2-12. Profiles of simulated results based on sensitivity analysis of $\boldsymbol{c}$. 46
Figure 2-13. Profiles of simulated results based on sensitivity analysis of $\boldsymbol{K_{N_2}}$. ...47
Figure 2-14. Comparison of conventional model and developed model.....48
Figure 3-1. Profiles of operating data and simulation results (a) pressure of HRS facility (b) station and vehicle pressure (c) vehicle temperature. 57
Figure 3-2. Overall HRS design procedure. 58
Figure 3-3. Graphical description of design variables of buffer storage system for one vehicle filling.....61
Figure 3-4. Average number of the allowable cycle with respect to pressure amplitude for Type 2 cylinder. 62
Figure 3-5. Performance chart of designed reciprocating compressor. 64

Figure 3-6. Total energy consumption depending on the number of stages. 67
Figure 3-7. Pressure profile for analyzing the effect of compressor operation. 69
Figure 3-8. Results of volume analysis according to compressor operation. 70
Figure 3-9. Pressure profile of 3 stages depending on operation compressor. 72
Figure 3-10. Pressure profile of back-to-back filling scenario (4 vehicles). 74
Figure 4-1. Computational domain for CFD simulation. 79
Figure 4-2. Flow channel designs selected for case studies. 83
Figure 4-3. Results of CFD simulation: velocity contour for each design geometry. 84
Figure 4-4. Velocity vector of the design geometry near the center of the GDL. ...88
Figure 4-5. Design of flow channel of the electrochemical cell for CO_2RR: (a) separate paths, (b) single-path with flow retrace, and (c) unidirectional uniform distribution flow with segregation.....91
Figure 4-6. Cell geometries with different sizes (a) $\boldsymbol{G7, 5cm^2}$, (b) $\boldsymbol{G7, 10cm^2}$, (c) $\boldsymbol{G7, 50cm^2}$, (d) $\boldsymbol{G8, 5cm^2}$, (e) $\boldsymbol{G8, 10cm^2}$, and (f) $\boldsymbol{G8, 50cm^2}$.....99
Figure 4-7. Scale effect on $\boldsymbol{u_{avg}}$. 100
Figure 4-8. Scale effect on the flow uniformity according to standard deviation of normalized velocity ($\boldsymbol{\sigma_{\overline{u}}}$).....100
Figure 4-9. Picture of actual CO_2RR experimental device.....104
Figure 4-10. Process flow diagram of the electrochemical CO_2 reduction experiment in a large-scale electrolyzer (50 cm^2). 105
Figure 4-11. Chronopotentiometry results (a) reference design (b) UDF design. .107
Figure 4-12. LSV results for reference design and UDF design with range from cell voltage 0 V to 3 V at v = 50 mVs^{-1}.....107
Figure 4-13. Partial current density of reference design and UDF design with respect to flow rate variations.....108
Figure 4-14. Experimental results of pH, interface, and flow pattern effect to mass transfer on CO_2RR. 110
Figure 4-15. Experimental current density data (points) regressed with CFD simulation (dotted lines) under different flow rates. 114

Chapter 1. Introduction

1.1. Research subject

An energy paradigm shift from fossil fuel to renewable energy is ongoing for achieving the goals of securing sustainable energy resources (infinite energy resources) and mitigating climate change [1]. Compared to coal and oil, natural gas (NG) has several advantages over other fossil fuels; it is less carbon intensive, and it is used in a variety of sectors (e.g., household, electric power, transportation, and industrial sector) [2]. Thus NG has been suggested as a bridge fuel for the energy transition from fossil-based energy systems to net-zero emission energy systems [3]. With synergies of NG value chain and infrastructure, hydrogen has been highlighted as one of the future energy sources due to its high energy enrichment and eco-friendliness [4]. Although hydrogen can be produced through fossil resources or water electrolysis with electricity, the majority of hydrogen production is derived from fossil fuels because of economic feasibility [5, 6].

Carbon dioxide emissions are the primary driver of global warming in the atmosphere, which leads to climate change [7]. Because the energy sector accounts for almost three-quarters of greenhouse gas emissions [8], managing carbon dioxide emissions is necessary to reduce greenhouse gas emissions in the fossil fuel value chain.

This thesis focused on NG and hydrogen energy mix with CO_2 utilization as a low carbon energy system for an intermittent energy transition scenario, shown in Figure 1-1. NG is extracted from subsurface reservoirs, treated by process facilities, and liquefied by a liquefaction plant. Gas carriers transfer liquefied natural gas (LNG)

to the import terminal (LNG transportation and distribution), and LNG-powered vessels are refueled at the bunker stations (LNG storage). The most important phenomena in LNG storage tanks were selected as one of the research subjects which occur during LNG transportation, distribution, and storage. Next, hydrogen is produced through the methane reforming process, which was already sufficiently studied as Technology Readiness Level (TRL) 9 [9], so it was excluded from the study. Instead, this study had an interest in a hydrogen refueling system that transports and distributes hydrogen energy (H_2 transportation and distribution). Finally, the low carbon energy value chain is completed only when the carbon dioxide emitted by the methane reforming process is treated [10]. Because an amine-base CO_2 capture process is also TRL 9 [11], it is also excluded from the research subjects. Alternatively, this study aimed to investigate the electrochemical conversion of carbon dioxide (CO_2 conversion).

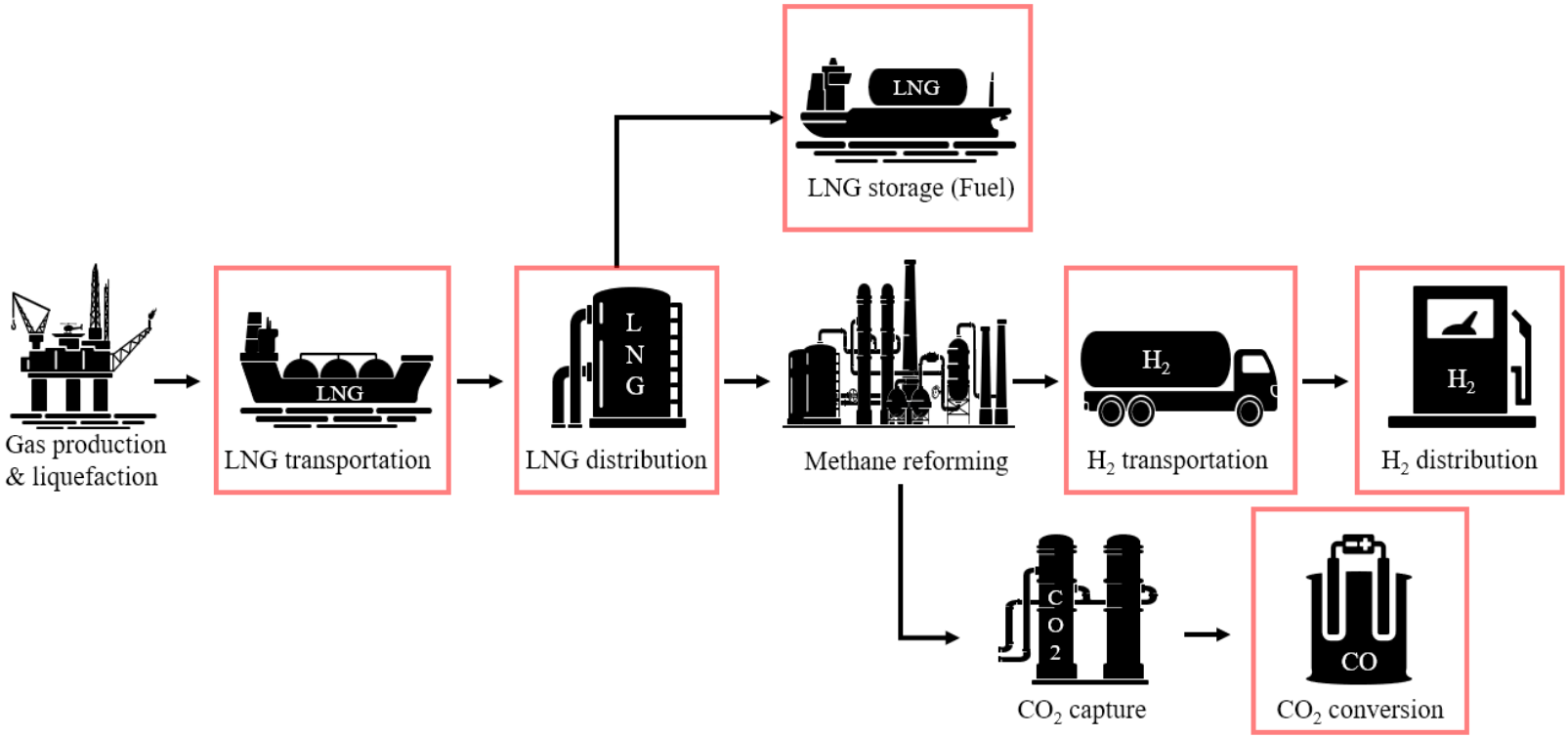

Figure 1-1. Research scope of low carbon energy system.

1.2. Research background

1.2.1. LNG storage

Recently, NG has been receiving attention as an eco-friendly energy source owing to intensified environmental regulations, resulting in the replacement of conventional heavy fuel oil with LNG for marine fuels [12-15]. In an LNG storage tank, the composition of LNG changes with time owing to the production of boil-off gas (BOG), which is called LNG weathering, and it is a crucial characteristic in designing the specifications of a BOG management, LNG storage, and LNG-fueled system. LNG is a preferred form for transporting NG because of its high density; however, it requires a low temperature below -162ºC. Concurrently, it is impossible to prevent heat ingress to an LNG storage tank completely, leading to BOG generation, which should be removed to prevent tank rupture. Because mainly the volatile components, such as nitrogen and methane, in the composition of LNG evaporate, the composition of the relatively heavier components gradually increases in the remaining LNG. This causes two important issues: boil-off rate (BOR) and BOG composition change over time [16-21].

Although some experimental studies have been conducted on the thermal behavior of LNG and NG, they have limitations. Kountz [22] measured the data of LNG composition, temperature, and mass changes with time; however, the author did not investigate the evolutionary trend of the BOG properties. Chen et al. [23] conducted experiments on the temperature and pressure changes in a 150,000-gal tank; however, the experiments were not performed at the typical LNG transportation and storage condition, i.e., approximately 1 bar. Although some other studies

analyzed actual operational data, only the information at the ports of origin and arrival was used to verify the prediction model for LNG weathering, without considering time-varying aspects [18, 19, 24]. Recently, there were some studies considering actual tank geometries. Lin et al. [25] built experimental equipment of Type-C LNG tank and studied the BOR and temperature distributions with various filling ratios using liquid nitrogen. Krikkis and Qu et al. [26, 27] studied the temperature, pressure, and BOR of a tank based on actual ship transportation data and the temperature distribution in a 40 m^3 Type-B mock-up tank, respectively [28, 29]. However, these studies utilized only liquid nitrogen; therefore, it was impossible to analyze the weathering features of an LNG and the composition change of the BOG and LNG over time. Perez et al. and Al Ghafri et al. [30, 31] measured the temperature, pressure, and composition changes of an LNG tank over time; nevertheless, the size of the experimental equipment was smaller compared to that of the industrial-scale tank.

In addition, many studies have developed numerical simulation models to predict the behavior of LNG and BOG in storage tanks. One of the simulation approaches is to use computational fluid dynamics (CFD) to rigorously analyze the mass and heat transfer of LNG in a storage tank [32-35]. Although CFD is a powerful tool for solving fluid flows with liquid and vapor interactions locally, it requires a long time to yield steady-state solutions. However, LNG tank operations, such as storage and transportation, typically take more than 10 days or even months; thus, a CFD approach is rarely appropriate for analyzing LNG and NG behavior during long-term operations. Additionally, auto-stratification, in which density difference causes bulk LNG to be divided into multiple layers, does not occur in LNG compositions

containing nitrogen less than 0.5 mol% during transportation [36]. This suggests that LNG having a low nitrogen content is almost homogeneous owing to free convection, and the local distribution is minor. Thus, using a CFD approach to predict evolutionary BOR and BOG composition changes would be an overburdened study.

Another approach is to use thermodynamic models to focus on the overall behavior of LNG and BOG in a tank, instead of local behavior [18, 19, 37], which is reasonable for predicting the composition change and evaporation rate in long-term operations. However, the classical thermodynamic model assuming a vapor-liquid equilibrium condition in an LNG tank is unfeasible when the size of an LNG tank is large because of the existence of a temperature gradient in the vertical direction in an actual scenario [31]. Miana et al. [19] predicted the evaporation rate of tank by incorporating a constant value that measured the initial volume of LNG in the tank divided by the volume at the discharging port. Because the BOR is fully related to the LNG properties, tank shape, and storage system conditions, a rigorous prediction model is required to estimate the BOG behavior well, instead of simply assuming the BOR. Furthermore, in some studies, a non-equilibrium model has been developed to predict LNG, BOR, and composition change. Migliore et al. [24] used non-equilibrium thermodynamic modeling and showed that the vapor phase temperature can be as much as 8ºC higher than the liquid phase temperature. Wang et al. [38] studied evaporation rate, the parameters of which are the temperatures of all phases. Because thermal stratification occurs in the vertical direction inside an NG zone, it is difficult to define the representative temperature of NG. Moreover, it is impossible to install many thermocouples in an industrial-use tank to measure the temperature of the interfacial phase at the exact locations in all height ranges, which

makes modeling an NG zone difficult.

In addition, various studies have investigated suitable energy balance equations to simulate the behavior in an LNG tank by thermodynamic modeling. Particularly, the issues of modeling the heat exchange at the interface could be divided into the vapor to liquid heat transfer and the enthalpy of the BOG. One of the assumptions regarding the interfacial heat transfer between the liquid and vapor phases is a rate that is 95% of the heat entering the vapor phase in the tank [30, 39], and another is the constant overall heat transfer coefficient at the interface ($4.0\ Wm^{-2}\ K^{-1}$) [31]. The other assumptions of interfacial heat transfer are conduction and convection [40]. Similarly, different methods are employed to estimate the enthalpy of the BOG. Wang et al. [38] employed the enthalpy of NG as the enthalpy of the BOG. Arjomandnia et al. [41] and Wang et al. [42] used the heat of vaporization energy as the enthalpy of the BOG.

1.2.2. Hydrogen distribution

Hydrogen has promising potential for energy transition toward low and zero carbon energy systems [43]. Hydrogen fuel cells generate electricity through an electrochemical reaction that has high efficiency and zero emissions at the point of use. It can be used to provide power across a wide range of applications (e.g., transport, industry, and power sector) Especially, fuel cell electric vehicles (FCEV) are superior to battery electric vehicles in terms of specific energy (mass and volume), greenhouse gas emissions, refueling time, and energy efficiency for the longer driving distance [44]. To have these advantages, FCEV currently uses highly pressurized filling in the onboard hydrogen tank to increase energy density in the finite volume.

However, when the high-pressure hydrogen is rapidly injected into the FCEV storage tank, the temperature of the filling hydrogen increases due to two factors [45, 46]. First, as the hydrogen goes through the valves between storage tanks, the hydrogen temperature rises because of the negative Joule-Thomson coefficient. Second, when the hydrogen enters the FCEV storage tank, the fluid work of the hydrogen changes into the internal energy causing the temperature of hydrogen to increase, which is called heat of compression.

The Society of Automotive Engineers (SAE) has been developing the SAE J2601 refueling protocol, which defines safety limits of pressure and temperature depending on the performance of hydrogen refueling for light and heavy duty gaseous hydrogen vehicles [47, 48]. The protocol covers applicable pressure classes, sizes of storage volume, and precooling temperature. It suggests a safe and fast filling

guideline: the average pressure ramp-up rate (APRR) and the refueling ending pressure with respect to initial vehicle pressure and ambient temperature.

The Korean government announced a goal of supplying 200,000 hydrogen vehicles and constructing 450 hydrogen refueling stations (HRS) by 2025. The need for nationwide distribution of optimized refueling facilities has emerged to cope with the increase in filling demand. Figure 1-2. shows a typical schematic diagram of an HRS in which the main configuration contains a tube-trailer as a hydrogen source to satisfy hydrogen demand, medium/high-pressure buffer storage to refuel FCEV, a compressor to recover the pressure of buffer storage, a precooler to cool down the hydrogen before dispensing into the FCEV, and a dispenser to control the filling rate of hydrogen. Typically, a tube-trailer operated in South Korea has a maximum pressure of 200 bar. A medium/high-pressure buffer storage comprises several sets of cylinders that store hydrogen at 500 and 950 bar, respectively. A precooler cools down hydrogen up to -40ºC (T40) according to SAE protocols.

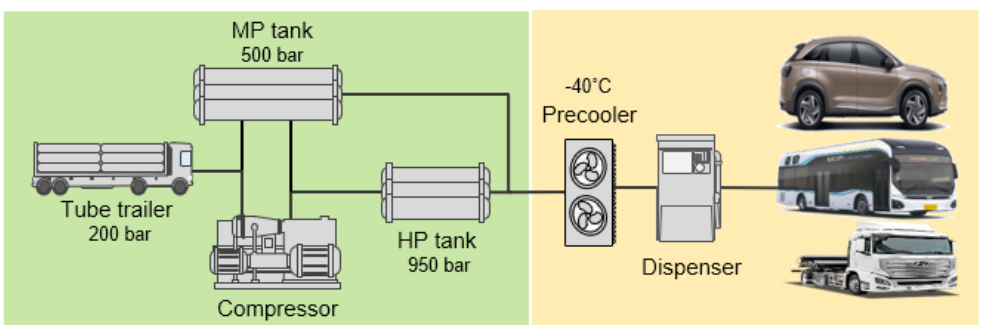

Figure 1-2. Schematic diagram of hydrogen refueling station.

A study on the optimized design of the compressor and buffer storage system is required for supplying HRS at a low-cost investment. Because a compressor and cascade buffer storage system accounts for about half of the total capital cost of

various HRS capacities [49, 50], and the capacity of both components has interdependence as a trade-off relationship i.e., the larger capacity of the compressor, the smaller capacity of the buffer storage system. Technically, when hydrogen is injected into directly vehicle tank by the compressor from hydrogen sources (e.g., tube trailer, pipeline, water electrolysis), the required capacity of the compressor becomes enormous which greatly increases the capital cost of an HRS. Therefore, as an alternative way to reduce the total capital cost, high-pressure buffer storage which is typically cheaper than a compressor is installed in the HRS as a status of high-pressure standby to meet the hydrogen fill-up demand.

To design hydrogen storage and refueling system, several studies have investigated the thermal behavior of hydrogen vehicle tanks during filling for safe and fast refueling [51-55]. Woodfield et al. showed the measured space average temperature during refueling can be predicted through the 0D model [56]. Bourgeois et al. developed a 0D model containing heat transfer calibration with experiments [55]. Zheng et al. showed temperature distributions in the tank are nearly uniform using the CFD simulation and experimental results [57]. However, all developed 0D models validated the thermal behavior of a vehicle tank without all refueling facilities. A validated model with a compressor is needed to conduct a performance evaluation of the entire process of HRS accurately (i.e., hydrogen filling and pressure recovery after filling completion).

Various studies have developed 0D or 1D thermodynamic analysis using a validated model of hydrogen filling and been carried out for optimizing HRS components (Buffer storage system). Since the compressor occupies the largest proportion of the total capital cost of an HRS, it should be designed carefully. Reddi

et al. [50] suggested how to size the capacity of the compressor, however, there are no additional studies related to compressor operation except for the filling sequence of the buffer storage system from higher to lower pressure recovery in order to prepare the next vehicle.

Rothuizen et al. [58] and Sadi et al. [59] showed that one-buffer system (direct filling system) that fills a vehicle tank directly has higher energy consumption compared to a multi-stages buffer system (cascade filling system) that fills a vehicle tank sequentially from a lower pressure buffer to a higher buffer tank. However, these studies did not perform the same time frame to compare the energy consumption of buffer storage configurations equally and considered only one vehicle refueling. The delay in filling time through the cascade storage system is the result of violating the guided filling time given by SAE protocols to save energy consumption. Elgowainy et al. [60] showed initial filling from the tube trailer to reduce the pressure difference between the station and the vehicle for reducing energy consumption.

Rothuizen et al. [61] demonstrated the optimal number of stages in the cascade system for one vehicle refueling is 3 to 4 and analyzed the energy-saving portion when the number of stages was increased up to ten with a certain pressure ratio and uniform volume of each stage. Xiao et al. [62] studied the overall energy consumption of one vehicle refueling depending on the pressure level of a three-stage cascade storage system fixing each stage of volume. Yu et al. [63] examined an optimal volume ratio of a three-stage cascade storage system fixing each pressure level. However, these studies performed energy optimization with only a few variables under roughly designed conditions without considering all design variables.

1.2.3. CO_2 conversion

Electrochemical conversion of CO_2 to valuable chemicals is a sustainable method of producing chemicals, a potential solution for resolving renewable energy supply as well as demand mismatch, and a method for reducing greenhouse gases. In particular, electrochemical CO_2 reduction (CO_2RR) can be easily scalable when a high-performance unit cell is available. This is because the capacity of the electrolyzer can be extended by applying a modular design. However, because most of the technologies are too expensive to replace the available processes, developing a commercially viable CO_2RR process is still a challenge. In addition, commercial-scale reactors are in the very early stages, although several pilot-scale CO_2RR projects are being carried out globally [64-66]. The major challenges in CO_2RR technology include high-energy requirements, product selectivity, reaction rate, and stability.

In recent years, significant research has been carried out to circumvent these challenges, and promising results have been reported on electrocatalyst development [67-70]. The developed electrocatalysts include metals, alloys, metal–nitrogen materials, and methods for their mass production [71]. Comprehensive reviews for the development of CO_2RR catalysts are available in the literature [72, 73]. Generally, designing and screening of the CO_2RR catalysts are carried out in batch or semi-batch electrolyzers such as H-cells. These types of electrolyzers are very useful for screening electrocatalysts and intrinsic kinetic studies because of their simple configuration, but they are not practical for evaluating the performance of the electrocatalyst in industrial-scale processes in which mass transfer and operating

conditions of the electrolyzer (such as reactant flow rate, temperature, pressure, and pH) play an important role. Generally, the current density of CO_2RR in H-cells can hardly exceed 100 mA/cm^2 because of the solubility and mass transport limitation of the CO_2.

Recently, using continuous flow gas-fed electrolyzers to overcome limitation issues of mass transport has gained attention, and various studies have reported very promising results [74, 75]. These types of electrolyzers can enhance the production rate via engineering electrolyzer configuration, electrode structure, and reactor operating conditions. Most gas-fed electrolyzers can be categorized as either hybrid or membrane reactors [76]. In the membrane reactor, a gas diffusion electrode (GDE) is placed next to the membrane. Thus, water-saturated CO_2 gas can be delivered to the cathode directly, avoiding unnecessary voltage loss caused by electrolytes. However, in the hybrid reactor, the GDE and membrane are separated by a catholyte layer. Thus, it is hard to scale up by stacking the unit cell, and the liquid layer induces a significant voltage drop. In a membrane reactor, the production rate depends on the mass transfer of CO_2 to the cathode/electrolyte interface, absorption of CO_2 and electron transfer on the cathode, and desorption and migration of products. Among them, mass transfer can be modified by optimizing the patterns in the flow plate, GDE structure, pH, and interface between the CO_2 and electrocatalyst [77]. Various studies have improved the current density of the electrolyzer by adopting 3D-structured GDE, adjusting the pH, and introducing complicated flow patterns [78, 79]. These modifications result in a higher mass transfer of CO_2 to the cathode and often produce a current density that is an order of magnitude higher than that of a conventional liquid-fed flow cell electrolyzer.

However, experimental measurement of the mass transfer rate of CO_2 to the interface is very challenging. This is because of the complex mass transfer and reaction mechanism as well as the zero-gap configuration. Therefore, various studies have focused on computational studies using computational fluid dynamics (CFD) to understand the electrochemistry occurring at a triple-phase boundary (TPB), mass transfer on the porous GDE, and mass diffusion–advection induced by complex flow patterns. CFD helps build a reliable physical model by incorporating continuity equations for mass, momentum, as well as energy balances, and the transport of species involved in the reaction including the momentum source term of the fluid flow generated in the porous medium. Additionally, the applicability of CFD in multidomain knowledge is useful for designing and optimizing an electrolyzer.

Recent studies have demonstrated promising progress toward managing successful CFD modeling applications for designing and optimizing fuel cells [80-82]. Nguyen et al. developed a CFD model to estimate the geometric factors of a graphene oxide-coated zinc nanoparticle electrocatalyst [83]. They demonstrated that the CFD model is consistent with experimental data and that faradaic efficiency (FE) can be controlled by graphene oxide coverage. In the case of water electrolysis, Tijani et al. conducted CFD analysis for distributing the flow of water evenly over the active area of an electrolyzer cell [84]. Upadhyay et al. studied anode flow pattern to understand the flow characteristics of a circular unit cell of proton exchange membrane (PEM) water electrolyzer [85]. Although these studies reveal the importance of reactant diffusion, their design cannot be directly applied to the CO_2RR electrolyzer design. The CO_2 reduction reaction generally occurs at the gas-liquid-solid three-phase interface. Therefore, gas-phase CO_2 diffusion to the catalyst

surface should be carefully considered and a new methodology enhancing CO_2RR need to be proposed.

Recently, Arquer et al. [75] developed a two-dimensional model for the CO_2RR. They modeled the CO_2 solubility, carbonate equilibria reaction, and concentration-dependent partial current. However, only the diffusive term was considered in the transport of species. Weng et al. developed a multiphysics model for predicting the overpotential of each compartment of a membrane electrolyzer producing CO and ethylene [86, 87]. They demonstrated that the GDE structure has a low mass transfer resistance; thus, the current density of CO could be one order of magnitude higher than that of a planner Ag electrode. These computational studies presented meaningful insights for improving the mass transfer rate of the reactant, but these models are limited to one or two dimensions. Hence, the geometrical effects on the reactor performance are rarely investigated. In addition, large-scale electrolyzers (>50 cm^2), whose performance is significantly affected by mass transfer, have not been comprehensively investigated.

1.3. Research objective

This dissertation focuses on developing proper numerical simulation models for predicting the transport phenomena that occur in the energy supply chain of low carbon energy with measurable variables from the perspective of chemical process system engineering: liquefied natural gas, hydrogen, and carbon dioxide. Each of the developed models was validated with the actual measured data and was utilized to suggest a design methodology for its system.

In the field of engineering, physics, and chemistry, the study of transport phenomena has an interest in the exchange of mass, energy, charge, momentum, and angular momentum using experiments and computational simulation [88]. Nowadays many studies have tried to analyze transport phenomena in three dimensions. However, a time-consuming 3D model is sometimes not suitable for system design, and it is difficult to fabricate a measurement device for the validation of the 3D model due to physical and economic limitations. For example, in the actual size of the LNG storage tank where non-equilibrium exists, three thermometers are usually installed: top, middle, and bottom. Therefore, even if the solution of the non-equilibrium in a large-scale tank by CFD is attainable, it is not easy to verify whether the solution is feasible or not by typical measurement facilities. Thus, proper numerical simulation models that can predict phenomena well using measurable variables are important in the engineering discipline. Similarly, since it is difficult to observe the flow inside the CO_2RR reactor directly using an experimental device, most studies have applied CFD simulation [85, 89] and investigated mass transfer effect indirectly by production rate, which is measurable physical quantities. On the contrary, some studies try to obtain a solution of reduced dimension by installing

several thermocouples in the hydrogen storage tank to obtain the space average temperature [56]. If the temperature of the hydrogen storage tank can be predicted well through the 0D model without a complex analysis of three dimensions, it is much more effective in system engineering. In summary, it is efficient from an engineering point of view to be able to predict phenomena by reducing the dimension and complexity of the prediction model as much as possible for validating the model with measurable variables.

In chapter 2, a 1D numerical model was developed to predict LNG weathering. Although the vapor phase temperature and the heat exchange at the interface have been utilized to predict the non-equilibrium thermodynamic behavior of LNG and BOG, the roughly measured vapor phase temperature cannot represent the entire vapor phase owing to thermal stratification, and it is difficult to quantify the heat transfer and thermodynamic equilibrium at the interface rigorously in a large-scale tank. To validate the developed model, an experiment was conducted, and the behavior of LNG and BOG was observed in a large-scale storage tank (50 m^3) under isobaric operation for long periods (50 days).

In chapter 3, a 0D numerical model was developed to evaluate the performance of HRS and validated with the actual operating HRS data. Because of the complicated interdependency of the main HRS components, most of the previous studies have investigated only a few selected variables to identify the trends of HRS performance under roughly designed conditions. Thus, this study examined the influence of all variables as much as possible, defined the hierarchy of importance between variables, and suggested a design methodology for sizing the main HRS components in consideration of actual constraints.

In chapter 4, a three-dimensional computational fluid dynamic model was developed to quantify the effect of the flow pattern on mass transfer that has a great influence on the reaction performance at the three-phase interface of CO_2RR. Instead of measuring mass transfer in the flow channel directly, we experimentally measured the production rate of CO in a large-scale electrochemical CO_2 reduction reactor (50 cm^2) depending on the flow patterns; one was designed by CFD simulation, and the other was referred from the literature. In addition, other extrinsic properties also were investigated experimentally to compare the relative influences of the flow pattern.

Chapter 2. LNG Storage[1]

2.1. Experimental apparatus and procedures

The storage tank used in the experiment was a vacuum-insulated cylindrical type-C with a total capacity of 50 m^3 (with a height and a diameter of 8.4 m and 2.8 m, respectively). The process flow diagram of the LNG weathering observation system is shown in Figure 2-1. Two thermometers, both having accuracy of ± 0.15ºC, were installed at 0.95 m from the bottom and 0.85 m from the top, respectively, to measure the temperature of both the liquid and gas phases inside the tank. The liquid level of the tank was measured through the pressure difference between the top and bottom of the tank. The pressure in the tank was constantly controlled at 0.08 barg using a pressure control valve located at the top of the tank, and the BOG was made to enter an Agilent 7890A Gas Chromatography (GC) system at 30 sccm (standard cubic centimeter per minute) using a mass flow controller. The remainder of the flow is vented through the atmosphere.

After LNG loading, the pressure was first gradually reduced from 0.3 barg to 0.02 barg and subsequently increased to 0.14 barg by closing the valve shown in Figure 2-2. Following this, the pressure was controlled to 0.08 barg using the control valve. The composition of the BOG was automatically measured every 2 hours and

---

[1] The work presented in Chapter 2 is based on Prediction model of LNG weathering using net mass and heat transfer in *Energy 247(2022): 123325* [90].

recorded for a total of 50 days, and LNG was sampled once a week using an LNG vaporizer. The composition of the BOG was not measured during the LNG sampling, and the sampling line was flushed using a vacuum pump between GC measurements of the LNG and BOG sampling. In the GC system, a capillary column was used as the separation column, and the composition of the mixture gas, comprising nitrogen (N_2), methane (C1), ethane (C2), propane (C3), i-butane, and n-butane, was measured using a thermal conductivity detector.

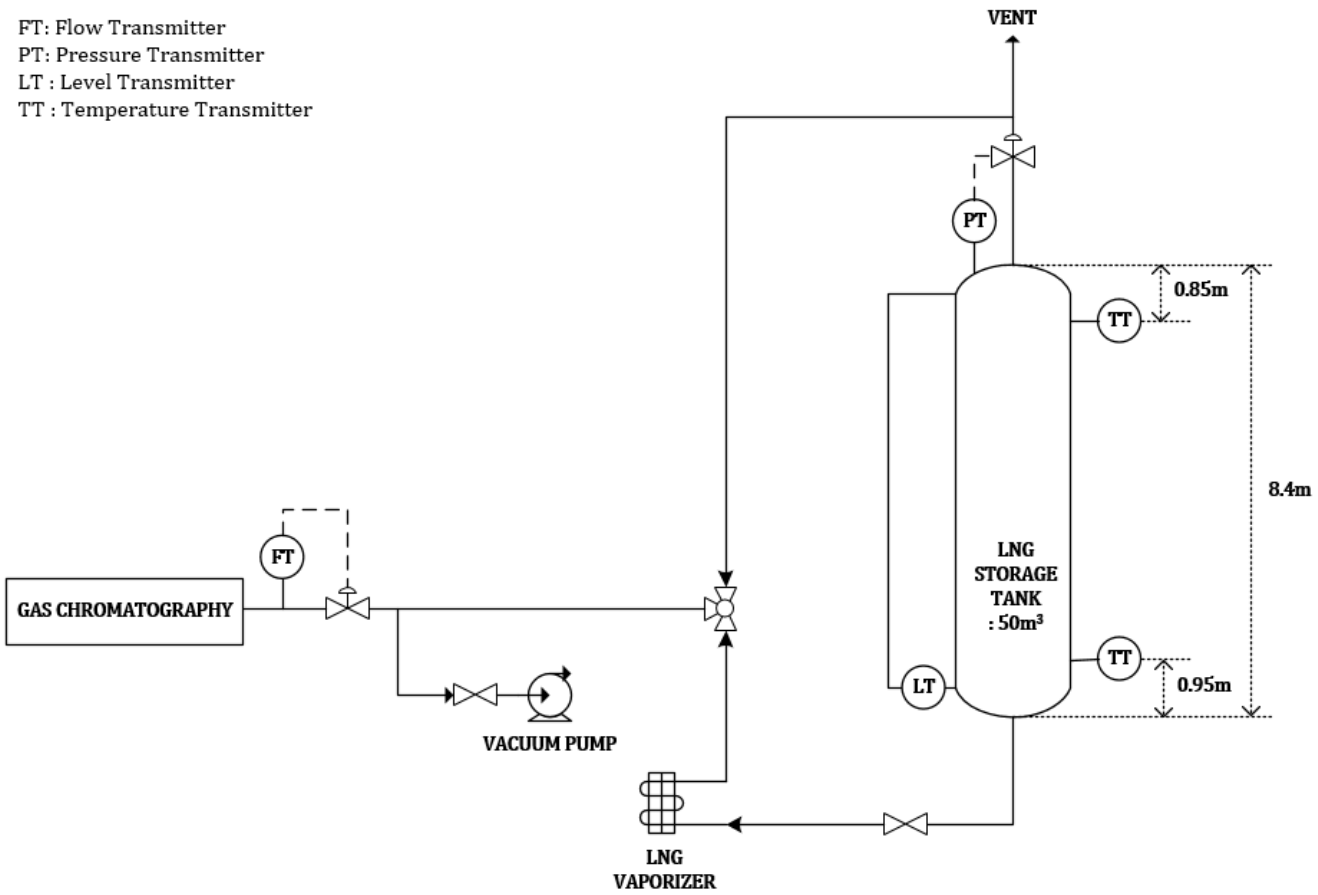

Figure 2-1. Process flow diagram of LNG weathering observation system.

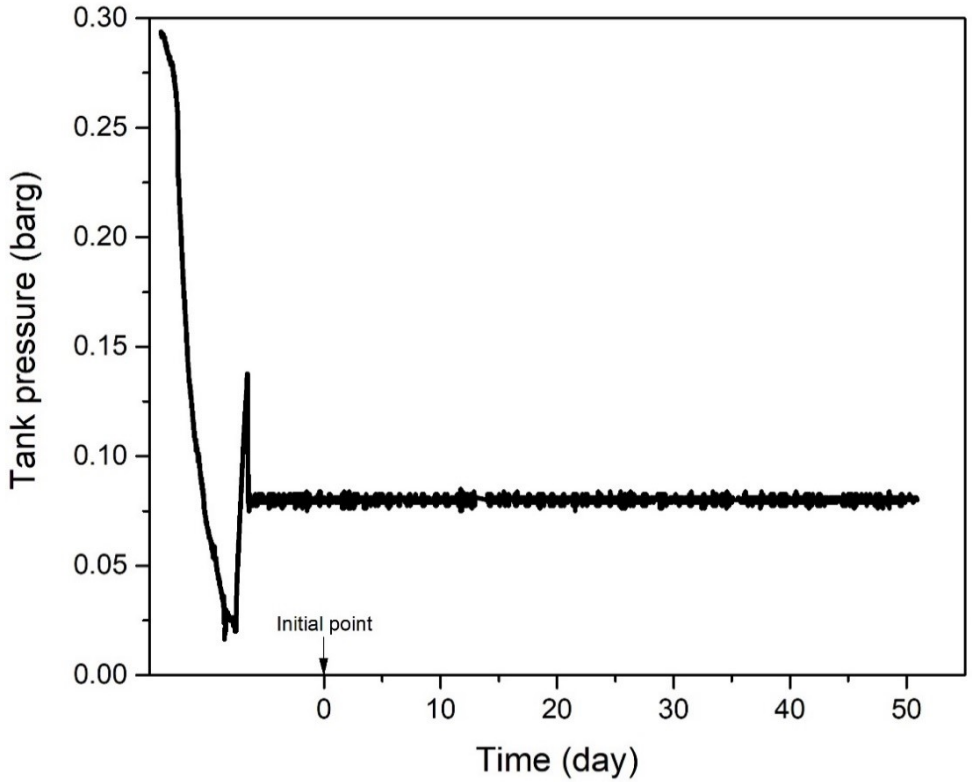

Figure 2-2. Changes in tank pressure over time in experiment.

2.2. Computational model description

2.2.1. Model assumptions and overall algorithm

A first-principles model containing parameters fitted by the experimental results was developed to facilitate the prediction of the thermal behavior of the large-scale storage tank. In the developed model, several assumptions are made to use non-equilibrium thermodynamic approaches. First, it is assumed that the liquid phase is homogeneous, i.e., it has no spatial temperature gradient. The liquid phase exists in a saturated state after loading LNG in the tank, which enables calculating the thermodynamic and transport properties of LNG based on the temperature and the composition only. Second, the developed model excluded vapor phase modeling; net evaporation of the BOG is assumed, excluding the condensation of NG for mass balance and the net heat transfer rate between the liquid and vapor phase for energy balance.

Figure 2-3 shows the overall algorithm of the developed model. The input data of the model are the initial LNG temperature (T_{LNG}), composition (x_i), tank pressure (P_{Tank}), differential pressure of the level ($Lev.$), ambient temperature (T_{Amb}), and tank specifications (e.g., size, area, volume, wall thickness, and thermal conductivity of the insulation). The above input data initialize the LNG density (ρ_{LNG}), mass (M_{LNG}), and liquid contact area with the wall (A_{LNG}). At each time step (5 min), the heat transfer rate to the liquid phase ($\dot{Q}_{LNG}$) is calculated from the overall heat transfer coefficient ($U_{overall}$) containing convection and conduction. After solving the boil-off equations using the vapor-liquid equilibrium constant, BOR ($\dot{M}_{BOG}$), and BOG composition (y_i) are computed. Subsequently, the heat and mass transfer in the

liquid phase are solved iteratively. The equations were then used to calculate and update the new states of the LNG mass, composition, enthalpy, temperature, density, level, and liquid contact area with the wall in the iteration loop with respect to the observed ambient temperature profile. This profile plays a vital role in the heat ingress into the tank.

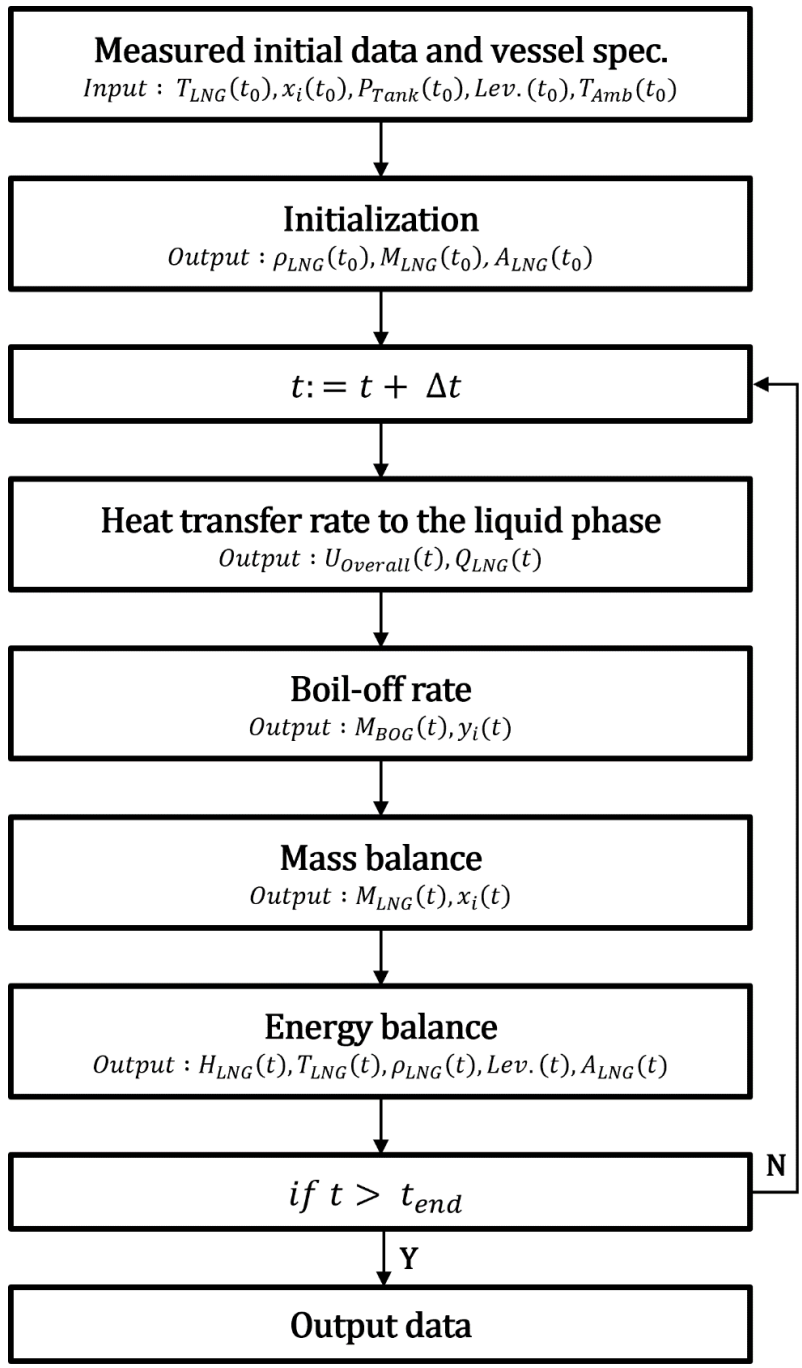

Figure 2-3. Schematic model algorithm for calculating BOR and BOG composition variation over time.

2.2.2. Heat transfer modeling

A schematic of the heat transfer from the environment to the LNG in the vertical tank is shown in Figure 2-4. The steady-state heat transfer rate to the liquid phase, as expressed in Eq. (2-1) was calculated using the overall heat transfer coefficient (Eq. (2-2)).

$$\dot{Q}_{LNG} = (UA)_{Overall} \cdot (T_{Amb} - T_{LNG}) \tag{2-1}$$

$$\frac{1}{(UA)_{Overall}} = \sum_{j=1}^{3} \frac{1}{h_j \cdot A_j} \tag{2-2}$$

This coefficient consists of inner and external convection, radiation from the sun, and conduction through the insulated walls. The external and internal convection heat transfer coefficients of the shell side were obtained by applying the Churchill-Chu correlation on the vertical plate in Eq. (2-3), which is a function of Rayleigh number (Ra) and Prandtl number (Pr) [91]. The convection heat transfer coefficient of the head was calculated based on the study of Radziemska et al. in Eq. (2-4) [92].

$$Nu_{Shell} = \frac{h_{Shell} \cdot L}{k} = \left[0.825 + \frac{0.387 \cdot Ra^{1/6}}{[1 + (0.492/Pr)]^{8/27}}\right]^2 \tag{2-3}$$

$$Nu_{Head} = 0.27 \cdot Ra^{1/4} \tag{2-4}$$

Moreover, the conduction heat transfer coefficient of the insulated walls with perlite (head, shell, and supports) was calculated by Eq. (2-5) with thickness d and conductivity of materials k. The Stefan-Boltzmann equation of radiation (Eq. (2-6)) was applied to Eq. (2-2) as a part of the outer heat transfer coefficient of the storage tank combined with the convection, where ε is a surface of emissivity, σ is the

Stefan-Boltzmann constant, and T_{Wo} is outer wall temperature [93].

$$\frac{1}{h_{Cond}} = \sum_{i=1}^{3} d_i/k_i \tag{2-5}$$

$$h_{rad} = \epsilon\sigma(T_{Wo}^2 + T_{Amb}^2)(T_{Wo} + T_{Amb}) \tag{2-6}$$

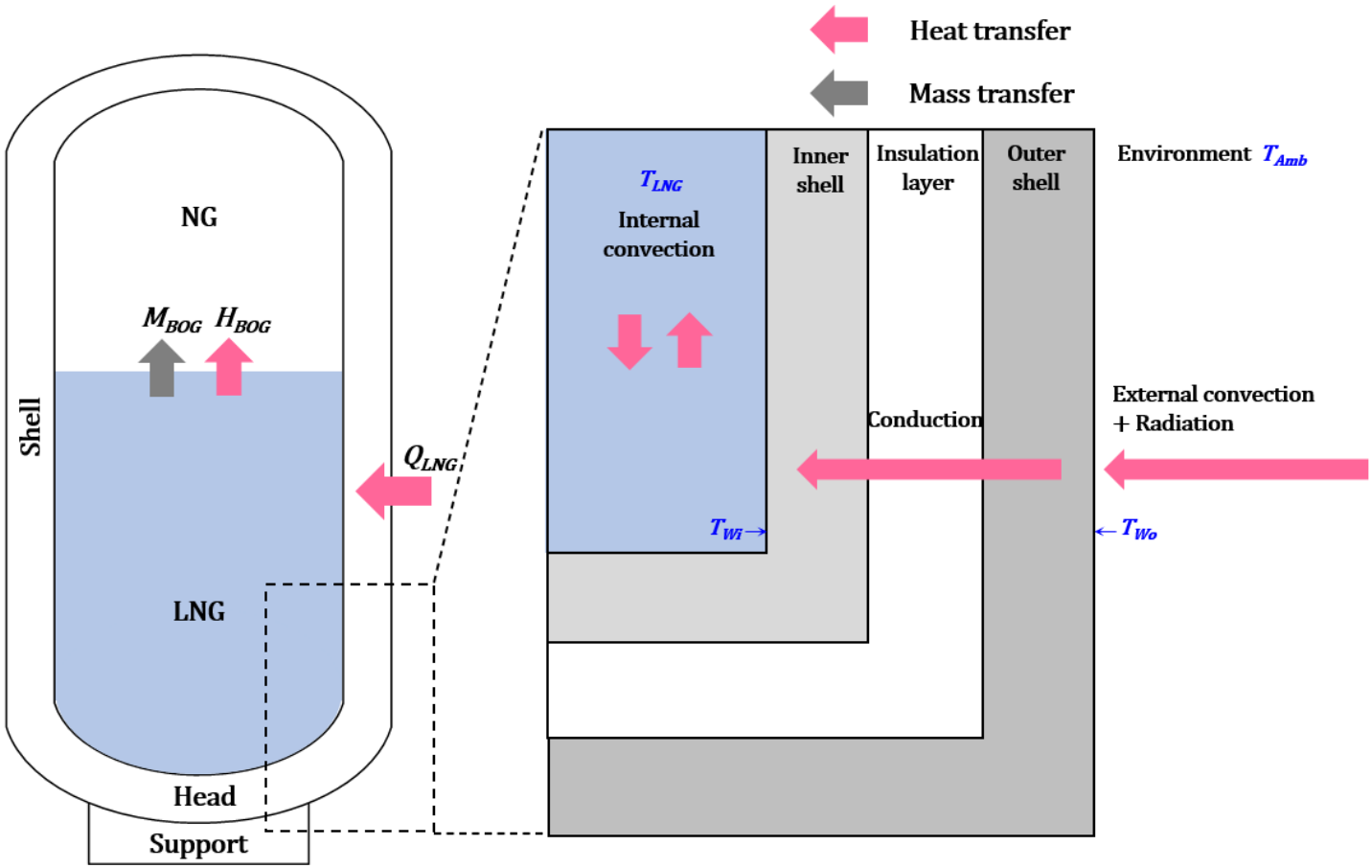

Figure 2-4. Schematic of mass and heat transfer in tank.

2.2.3. Boil-off modeling

In the proposed model, we employed the boil-off model (Eq. (2-7)) by Qu et al. [27] to avoid the overburden of computation of the local thermal equilibrium. Eq. (2-7) is based on the linearized form of the statistical rate theory for the net evaporation expression, which replaces the vapor temperature term with a pressure term. In the equation, $S_{Interface}$ is the free surface area, MW_{LNG} is the molecular weight of LNG, P_{Sat} is saturation pressure (bubble point pressure) of LNG and R is the universal gas constant. Using this equation, the proposed model can calculate the BOR without considering the vapor temperature. The accommodation coefficient, α proposed by Qu et al., was originally intended to consider the liquid motion effect on evaporation [27]. Without the accommodation coefficient, Eq. (2-7) contains only the driving force from the difference between the saturation pressure and the pressure of the tank for determining the evaporation rate, assuming that the ratio of the liquid to vapor temperature is close to unity. However, in a practical scenario, the interfacial temperature can present a discontinuity between the phases [94]. Therefore, we used the accommodation coefficient as expressed in Eq. (2-8), which is a linear function of the heat conduction part of the total heat flux and contains a constant empirical parameter (c) to mitigate the deviation between the theory and experiment.

$$\dot{M}_{BOG} = \alpha \cdot S_{Interface} \cdot \sqrt{\frac{MW_{LNG}}{2 \cdot \pi \cdot R \cdot T_{LNG}}} (P_{Sat}(T_{LNG}) - P_{Tank}) \tag{2-7}$$

$$\alpha = c \cdot \dot{Q}_{Conduction} \tag{2-8}$$

2.2.4. Mass and energy balance

The conservation of mass and composition in the LNG phase can be expressed as Eqs. (2-9) and (2-10) respectively, using the mass composition fractions of both phases: $\hat{x}$ and $\hat{y}$. The amount of evaporation determined using Eq. (2-7) was removed from the liquid phase. Moreover, it is necessary to specify the BOG composition. However, the BOG compositions computed using an equation of state (EOS) yielded a higher nitrogen content in the BOG compared to the experimental data. Alternatively, GIIGNL [95] proposed an empirical K_i value for the molar composition of each component in BOG. K_i, which is the vapor-liquid equilibrium ratio of a component, is expressed as y_i divided by x_i, where K_{N_2}= 20 ~ 26, K_{C1}= 1, K_{C2}= 0.005, and K_{C2+}= 0. The values were implemented in our developed model to quantify the BOG composition. The K_{N_2} value suitable for this simulation was 20 in accordance with the N_2 change of the BOG composition in the experiment.

$$\frac{dM_{LNG}}{dt} = -\dot{M}_{BOG} \tag{2-9}$$

$$\frac{d\hat{x}_{LNG}M_{LNG}}{dt} = -\hat{y}_{BOG}\dot{M}_{BOG} \tag{2-10}$$

As discussed in the introduction chapter, numerous papers have reported the energy balance equation of the interfacial heat transfer rate and the enthalpy of the BOG. In this paper, an equation considering that all heat entering LNG from the environment is transferred to the enthalpy of the BOG is designed. Specifically, the division of the equation into two terms is expressed as only a single term of the net heat transfer rate. According to Ghafri et al. [31], the amount of entering heat is used

to increase the bulk liquid temperature in the initial isobaric operation by natural convection. Subsequently, it is observed that the temperature distribution of the bulk LNG diminishes, and most of the heat ingress in LNG is used to evaporate the liquid. Because the experimental conditions of this study are similar to those mentioned in a previous study, Eq. (2-11) can be applied.

$$\frac{dH_{LNG}}{dt} = -H_{BOG} + \dot{Q}_{LNG} \tag{2-11}$$

2.2.5. Equation of state for properties

In this study, all thermodynamic and transport properties were calculated using REFPROP 10.0 released by the National Institute of Standards and Technology (NIST). Eq. (2-12) used in REFPROP is the explicit Helmholtz free energy as a function of density, temperature, and composition [96] and consists of an ideal gas mixture term ($a°$) and a residual part (a^r). The advantage of this equation is that most of the calculated thermodynamic properties fit the experimental data better compared to those estimated using the Peng-Robinson cubic EOS [97].

$$a(\rho, T, x) = a^{\circ}(\rho, T, x) + a^{r}(\delta, \tau, x) \tag{2-12}$$

where δ is the reduced mixture density ($\delta = \rho/\rho_r(x)$) and τ is the inverse reduced mixture temperature ($\tau = T_r(x)/T$). The ideal gas mixture term and residual part are given respectively

$$a^{\circ}(\rho, T, x) = \sum_{i=1}^{N} x_i \left[\alpha^{\circ}_{oi}(\rho, T) + \ln x_i\right] \tag{2-13}$$

$$a^{r}(\delta, \tau, x) = \sum_{i=1}^{N} x_i \alpha^{r}_{oi}(\delta, \tau) + \sum_{i=1}^{N-1} \sum_{j=i+1}^{N} x_i x_j F_{ij} \alpha^{r}_{ij}(\delta, \tau) \tag{2-14}$$

In Eq. (2-13), the dimensionless form of the Helmholtz free energy in the ideal-gas state of component i is given with critical parameters of the pure components ($\rho_{c,i}$ and $T_{c,i}$) by

$$\alpha^{\circ}_{oi}(\rho, T) = \ln\left(\frac{\rho}{\rho_{c,i}}\right) + \frac{R^*}{R}\left[n^{\circ}_{oi,1} + n^{\circ}_{oi,2}\frac{T_{c,i}}{T} + n^{\circ}_{oi,3}\ln\left(\frac{T_{c,i}}{T}\right)\right. \tag{2-15}$$

$$+\sum_{k=4,6} n^{\circ}_{oi,k} \ln\left(\left|\sinh\left(\vartheta^{\circ}_{oi,k}\frac{T_{c,i}}{T}\right)\right|\right) - \sum_{k=5,7} n^{\circ}_{oi,k} \ln\left(\left|\cosh\left(\vartheta^{\circ}_{oi,k}\frac{T_{c,i}}{T}\right)\right|\right)]$$

where R^* is 8.314510 *J/mol/K*.

In Eq. (2-14), the residual part of the reduced Helmholtz free energy of component i and a binary specific departure function with binary specific coefficients and parameters $(\alpha^r_{ij}(\delta,\tau))$ is given by

$$\alpha^r_{oi}(\delta,\tau) = \sum_{k=1}^{K_{Pol,i}} n_{oi,k}\delta^{d_{oi,k}}\tau^{t_{oi,k}} + \sum_{k=K_{Pol,i}+1}^{K_{Pol,i}+K_{Exp,i}} n_{oi,k}\delta^{d_{oi,k}}\tau^{t_{oi,k}}\, e^{-\delta^{c_{oi,k}}} \qquad (2\text{-}16)$$

$$\alpha^r_{ij}(\delta,\tau) = \sum_{k=1}^{K_{Pol,ij}} n_{ij,k}\delta^{d_{ij,k}}\tau^{t_{ij,k}} + \sum_{k=K_{Pol,ij}+1}^{K_{Pol,ij}+K_{Exp,ij}} n_{ij,k}\delta^{d_{ij,k}}\tau^{t_{ij,k}} \cdot \exp\left[-\eta_{ij,k}\left(\delta-\varepsilon_{ij,k}\right)^2 - \beta_{ij,k}\left(\delta-\gamma_{ij,k}\right)\right] \qquad (2\text{-}17)$$

Parameters of ideal-gas state of component i $(n^{\circ}_{oi,k}, \vartheta^{\circ}_{oi,k})$ in Eq. (2-15) and parameters of the residual part $(n_{ij,k}, d_{ij,k}, t_{ij,k}, \eta_{ij,k}, \varepsilon_{ij,k}, \beta_{ij,k}, \gamma_{ij,k})$ in Eq. (2-16) are listed in Ref. [96].

2.3. Results and discussions

2.3.1. Experimental validation

The main aim of this research was to investigate LNG weathering phenomenon by observing an LNG storage tank and developing a simulation program. The experimental and simulation results were compared to validate the feasibility of the proposed model for industrial application. Mean absolute percentage error (MAPE) is the average of the absolute difference between experimental and simulated value divided by the simulated value over time.

Estimating LNG temperature over time is the top priority task to build up a feasible computational model because it is used to calculate not only the saturation pressure but also the LNG density. Figure 2-5(a) shows the experimental data of LNG temperature. Although small fluctuations were observed in the LNG temperature by the changes in the ambient temperature, the overall tendency of increasing liquid temperature was simulated well. Because volatile components evaporate first and the remaining LNG comprises heavier components over time, the saturation temperature of LNG increases. Our proposed model predicted this tendency of increasing LNG temperature well using the energy balance equation in Eq. (2-11) with MAPE of 0.02%.

The level meter measures the differential pressure of the liquid in the tank, and the actual height of the liquid can be calculated from the LNG density. Subsequently, the storage volume of LNG can be evaluated based on the geometric information of the tank. Thereafter, the BOR can be estimated from the slope of the level data. Figure 2-5(b) shows that the observed level of LNG decreases linearly, and this

behavior matches well with our modeling results (MAPE of 0.46%). Therefore, the developed model predicted the BOR well.

To solve the mass and composition balance equations, Eqs. (2-9) and (2-10), the BOG composition needs to be specified into the BOR (Eq. (2-7)) predicted from level data. Figure 2-6 shows the normalized methane and nitrogen composition changes in the BOG with time, and each component was normalized with respect to the maximum and minimum molar composition for the given period, respectively. The red and blue solid lines show that the normalized simulation results of the methane and nitrogen compositions, respectively, match the normalized experimental results well (with MAPE of C1, 0.047%). A relatively smaller amount of nitrogen was observed compared to that of methane at the beginning, and the mole fraction of nitrogen decreased very rapidly. On the contrary, the mole fraction of methane in the BOG increased significantly from the beginning. It should be noted that other substances heavier than nitrogen and methane existed in the LNG phase; however, they were barely detected in the BOG. The molar composition of C2 in the BOG is of the order of 1-e2%, and C3 was barely observed in GC. These results showed that our approach of using equilibrium constants can provide reasonable results, even during long-term storage.

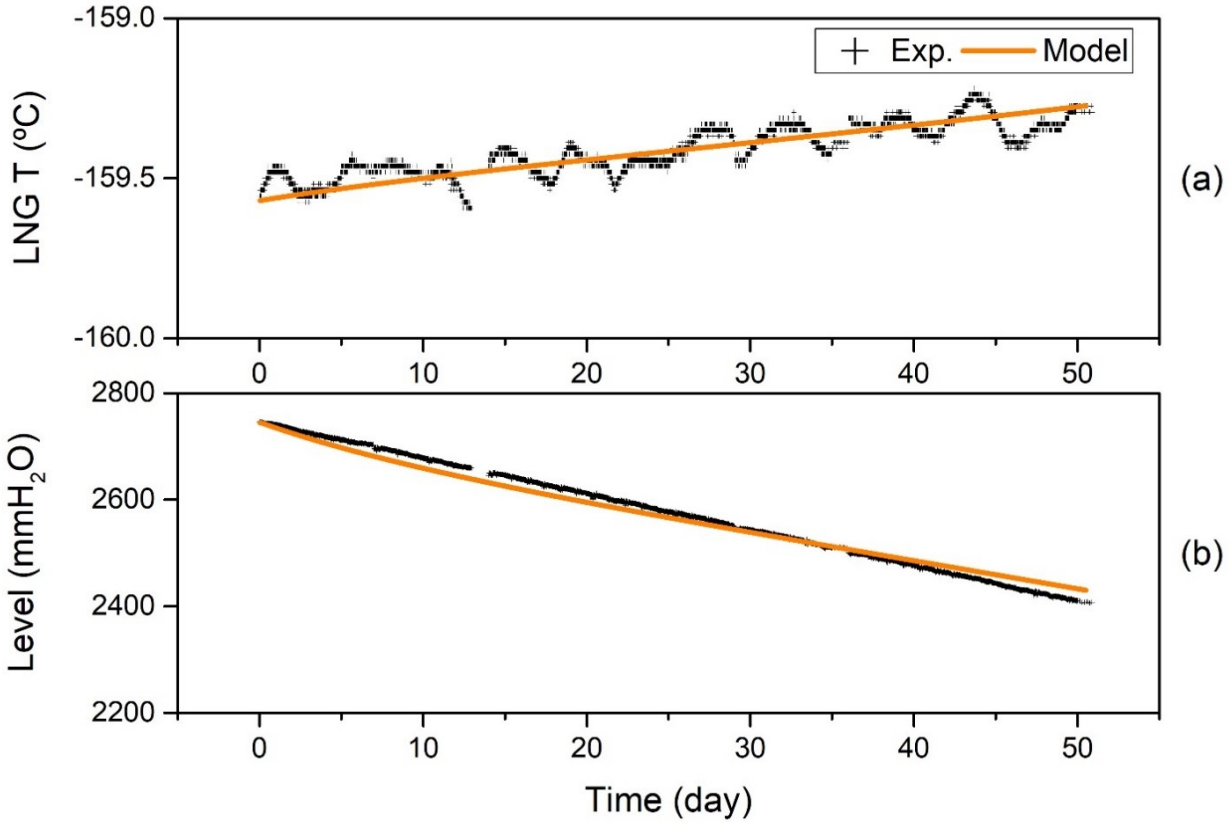

Figure 2-5. Profiles of experimental data and simulation results (a) LNG temperature (b) level.

It was seen that the measured compositions of methane and nitrogen in LNG fluctuated in each sampling period. Therefore, the experimental results of the LNG composition are presented in the form of squares in Figure 2-7 by calculating the average composition during each period of the LNG sampling. The results of tracking the change in the composition by simulation are shown as a solid line in Figure 2-7. The preferential evaporation of methane and nitrogen from LNG caused the depletion of these components in LNG, which was observed in both experiments and simulation with MAPE of C1, 2.98%. After 50 days, almost no nitrogen was detected in LNG. Contrary to the composition change of the BOG, the rate of change of C1 in the LNG composition is relatively low.

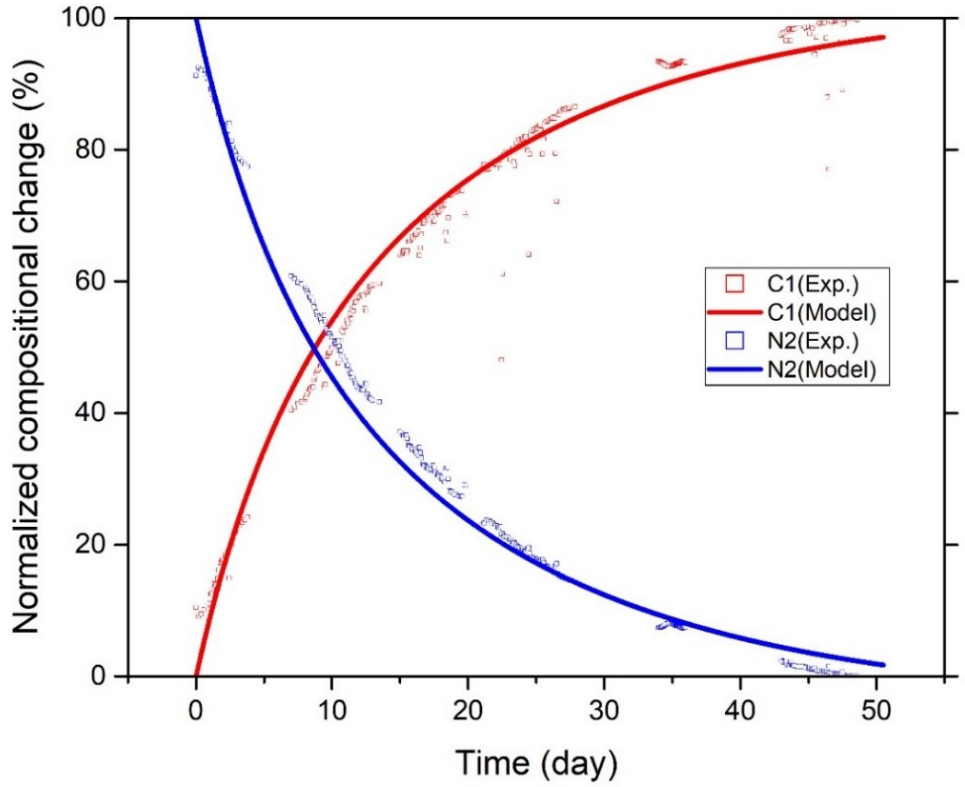

Figure 2-6. Profiles of normalized experimental data and simulation results.

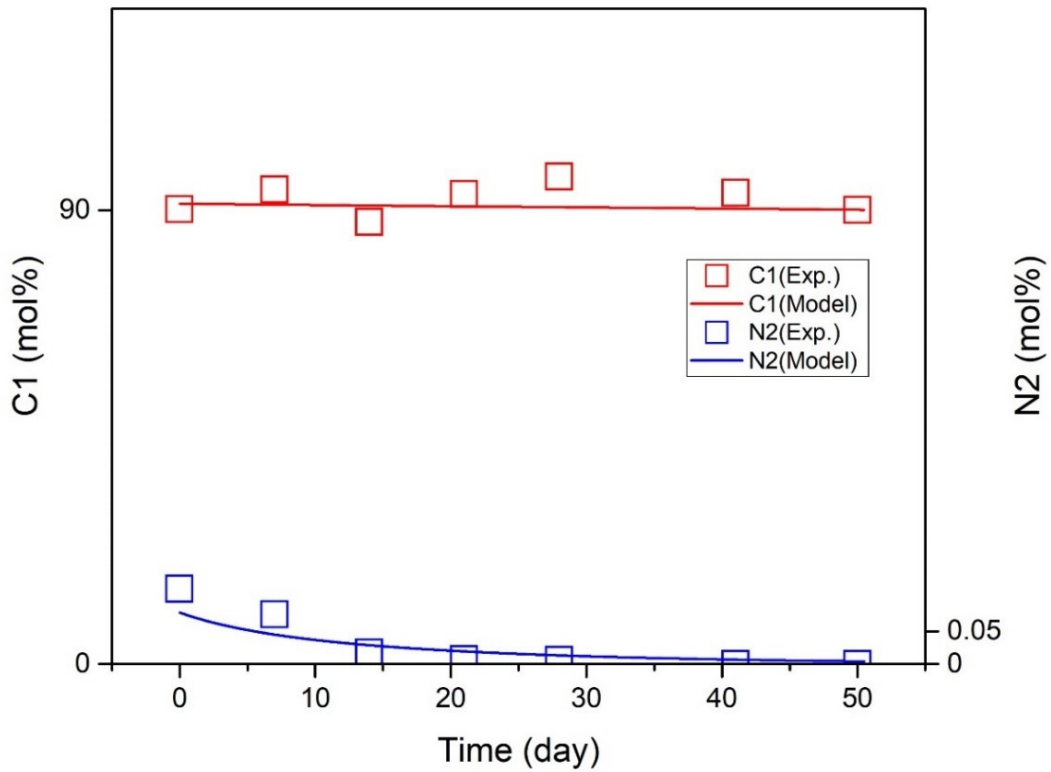

Figure 2-7. Profiles of experimental LNG compositions with simulation results.

2.3.2. Simulation study

Based on the above, the developed model results show good agreement with the experimental data of the LNG temperature, BOR, and BOG and LNG compositions. The simulated BORs using the developed model are shown in Figure 2-8 and were normalized with reference to the initial BOR. Contrary to the linear decrease in the level, as shown in Figure 2-5(b), the evaporation rate decreases drastically with time. The amount of reduction in the evaporation rate for each composition is related to the composition change of the BOG. The trend of the BOG decrease can be attributed to several factors: reduction in the LNG volume, heat ingress due to the diminishing contact area, and decreased driving force (increase in the LNG saturation pressure).

In the proposed model, the prediction of the evaporation rate and the composition of the BOG were separated, being not significantly affected by the time step. When the temperature and pressure of the system are specified for using the classical thermodynamic equilibrium based on cubic EOS, the size of the time step affects the amount of BOG generation and the composition of BOG simultaneously. The amount of BOG generation increases, and the molar composition of the BOG becomes heavier because a larger time step causes a larger heat ingress once in a loop. Therefore, the time step should be treated as an additional variable to match both actual trends in the simulation. However, it is difficult to predict them together using the classical thermodynamic equilibrium owing to the non-equilibrium state in the tank. Thus, our approach integrated with boil-off modeling and equilibrium constants would allow the prediction of the thermal behavior of a tank well. A numerical sensitivity analysis was conducted for the developed model, and a time

step of up to 30 min was found to be reliable in terms of the accuracy of the results.

A brief explanation of the modeling of the NG zone is as follows. Because the LNG volume is calculated from the level data, the remaining volume of the tank can be referred to as the NG volume. Subsequently, the mass of NG is specified using the measured temperature, pressure, and composition. Subsequently, BOG properties are calculated using the BOR equation and the BOG equilibrium constant. Following this, the mass of the evaporated BOG and the mass of the NG are mixed well instantly. The amount of mass discharged from the tank and the amount of mass remaining in the NG zone are computed with respect to the measured temperature and pressure of the next time step. Figure 2-9 compares the composition discharged from the tank and that directly generated from LNG. As shown in Figure 2-9, the difference in the compositions obtained using the model with and without the NG zone is very small. Mean absolute percentage error (MAPE) is the average of the absolute difference between simulated NG and BOG composition divided by the NG composition over time, and MAPE of C1 is 0.018%. Generally, compared to the composition change over time and the amount of evaporation, the volume of the vapor phase in the tank is relatively smaller. Therefore, the BOR and the composition of the BOG can be calculated without consideration of the NG zone.

Although observed NG temperature cannot stand for the entire NG temperature distribution, the temperature difference between the two phases, as shown in Figure 2-10, provides relevant insights. The temperature deviation started from 17ºC and increased gradually until approximately 24ºC at the end of the experiment. Thus, the ratio of liquid to vapor temperature is not unity. According to a previous study [94], a large temperature difference between the liquid and vapor enlarges the temperature

discontinuity across the interface. However, using α in Eq. (2-8) with the constant empirical parameter (c) shows the possibility of mitigating the deviation between the theoretical formula and the actual behavior, which was a 17ºC difference across the interface in the beginning and increased by 7ºC during long-term storage.

Figure 2-11 shows the energy removed from LNG based on the specified enthalpy of the BOG, which is normalized with respect to the amount of heat ingress to LNG. The mass-specific heat of vaporization and the saturated vapor enthalpy were calculated using the EOS with initial system information and were multiplied by the amount of evaporation to compare it to the heat ingress to LNG. In the developed model, it was assumed that all heat entering LNG from the environment is the enthalpy of the BOG, which was validated based on the results of the LNG temperature and the level prediction. However, establishing the energy balance equation using the heat of vaporization or the saturated vapor enthalpy requires additional heat transfer equations from NG to LNG, which necessitates NG zone modeling.

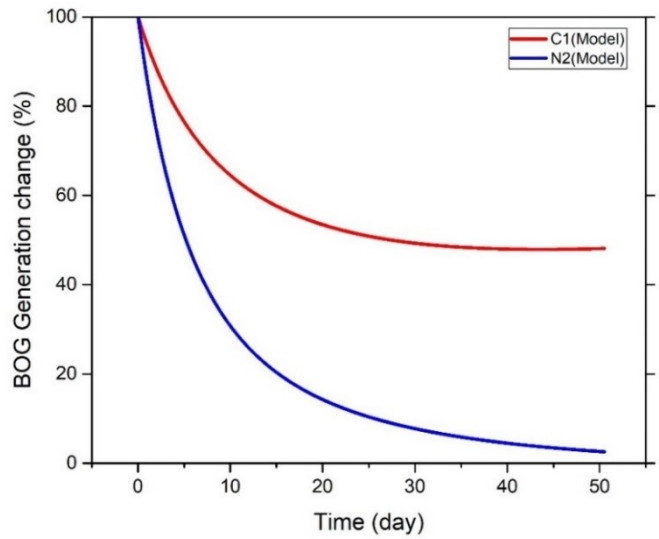

Figure 2-8. Profiles of normalized evaporation rate for each component.

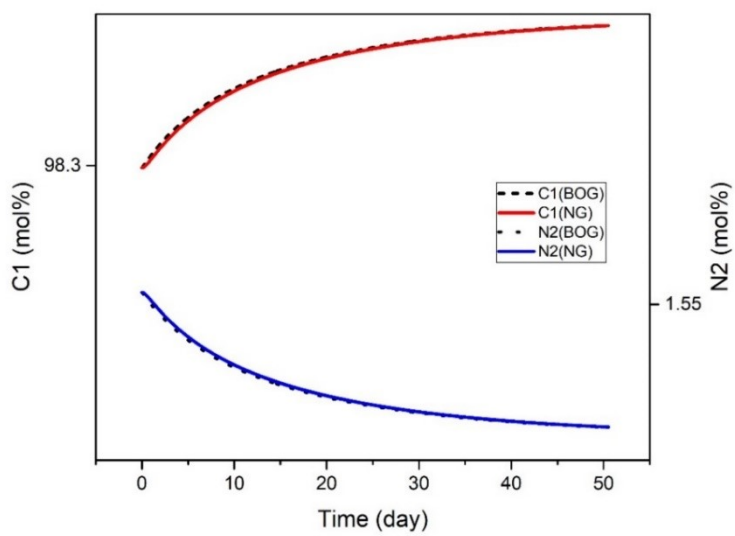

Figure 2-9. Comparison of vapor compositions with respect to presence or absence of NG modeling.

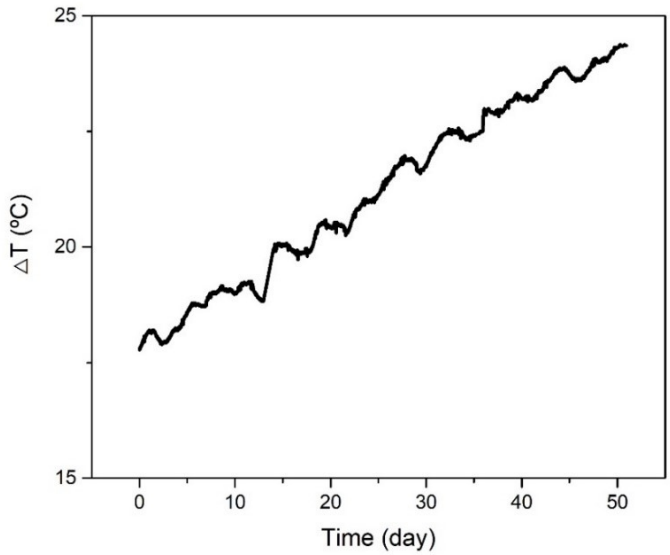

Figure 2-10. Profile of measured temperature difference between LNG and NG zones.

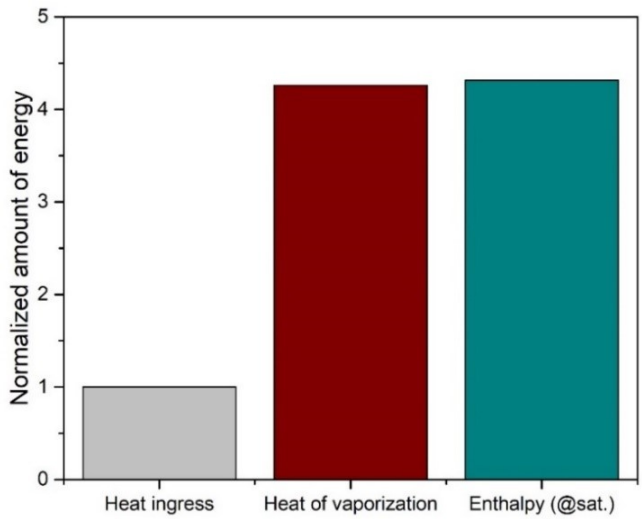

Figure 2-11. Comparison of removed energy from LNG with quantified BOG enthalpy at initial point.

2.3.3. Sensitivity analysis of parameter

In this study, the empirical constant parameter for BOR prediction (c) was determined based on the measured level change trend, i.e., the BOR. In an industrial storage tank, the BOR can be affected by the type, material, and specifications of the tank and its insulation. Therefore, the c needs to be adjusted based on the tank specifications. To examine this effect, sensitivity analysis was conducted on a change of ± 10% in c. It can be seen from Figure 2-12 that the trends of the level and LNG temperature change based on the variance in c. Increasing c results in an increasing slope of the level, i.e., more BOG generation; however, there is no compositional change due to the separated approach.

As explained in section 2.2, in this model, the value of K_{N_2} was selected as 20. Although determining the K_{N_2} value is not in the scope of this study, it is already known that there is a strong correlation between the LNG and BOG compositions when loaded in a tank. Therefore, to apply this model to another case having quite a different LNG composition, adjustment of K_{N_2} may be required. Because GIIGNL [95] suggested the range of K_{N_2} within 20 ~ 26, we performed a sensitivity analysis of K_{N_2} based on the measured initial information of the system. As shown in Figure 2-13, with the increase in K_{N_2} from 20 to 26 by 3, the molar composition of N_2 in the BOG increases. Moreover, more preferential evaporation of LNG lowered the saturation pressure of LNG; consequently, the BOR decreased.

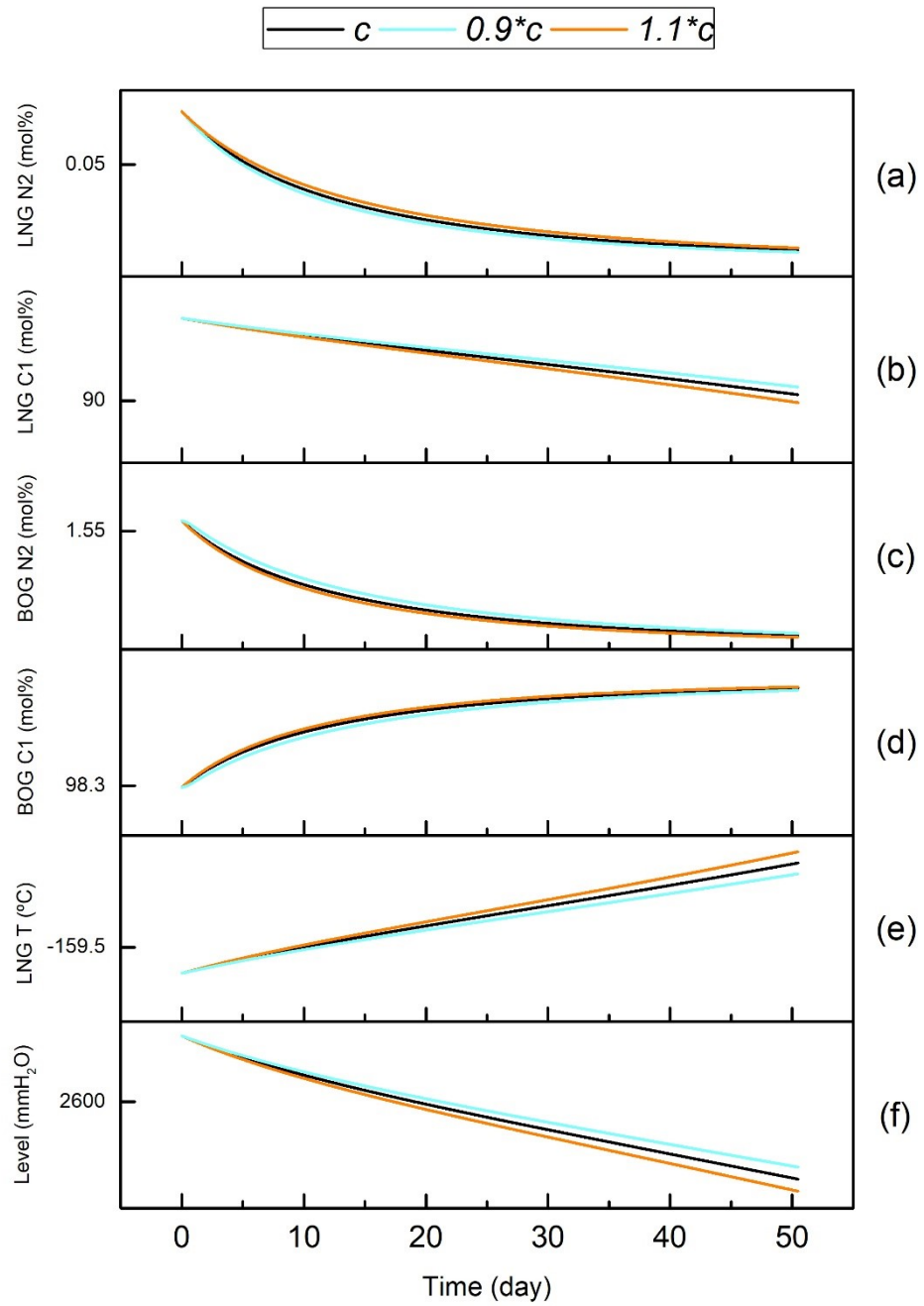

Figure 2-12. Profiles of simulated results based on sensitivity analysis of *c*.

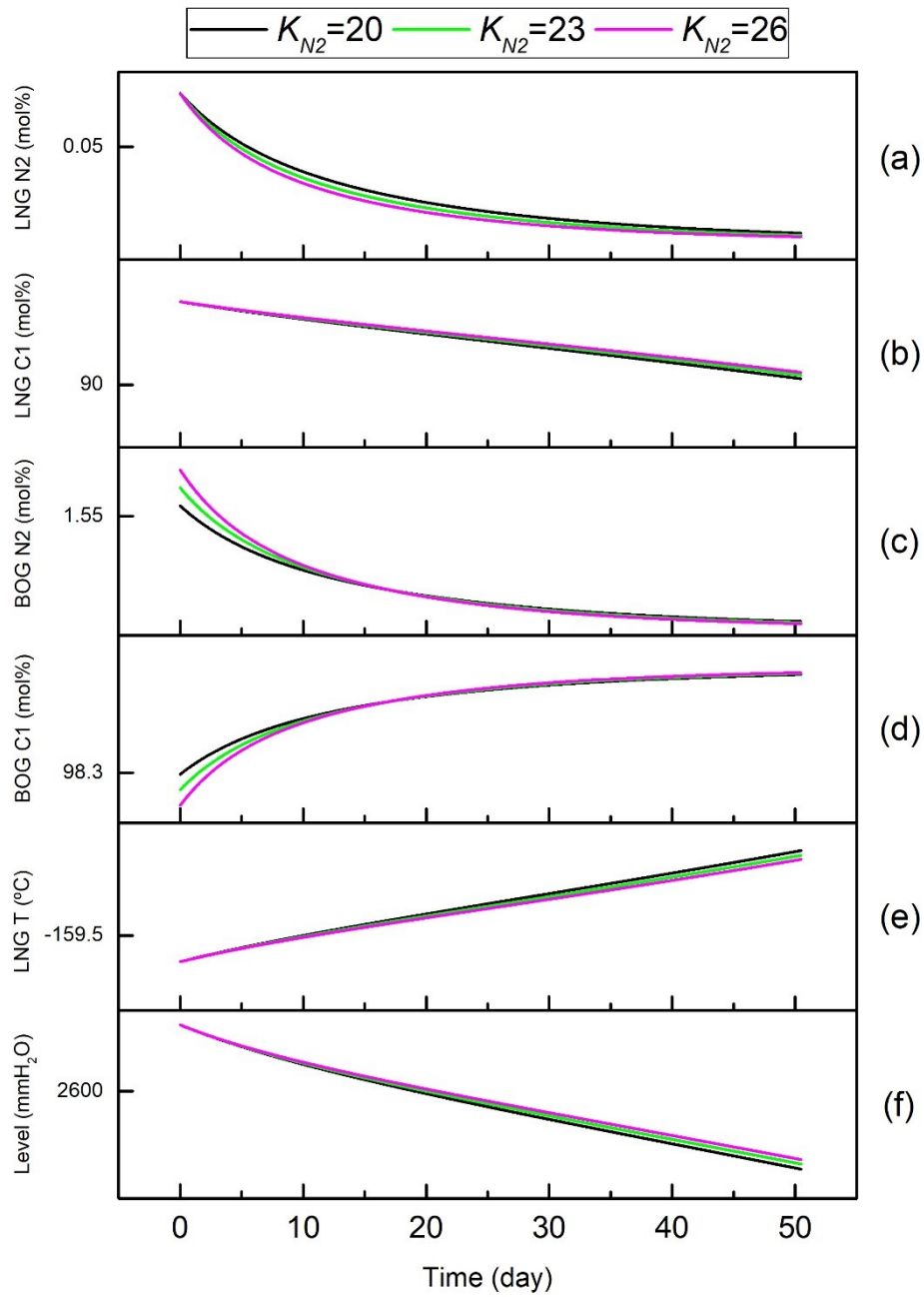

Figure 2-13. Profiles of simulated results based on sensitivity analysis of K_{N_2}.

2.3.4. Comparison of conventional and developed model

Figure 2-14 compares levels of observed data and two simulated data; one is the developed model, and the other is a conventional model i.e., the equilibrium approach. As discussed in section 2.3.1. and 2.3.2 that the slope of the level data means BOR. The developed model predicted the BOR well, however, the equilibrium state assumption in the storage tank results in a large difference in BOR which has an impact on designing a BOG handling system. In summary, as the size of the storage increases, the non-equilibrium state in the tank may increase, therefore, a more delicate analysis of BOR is required.

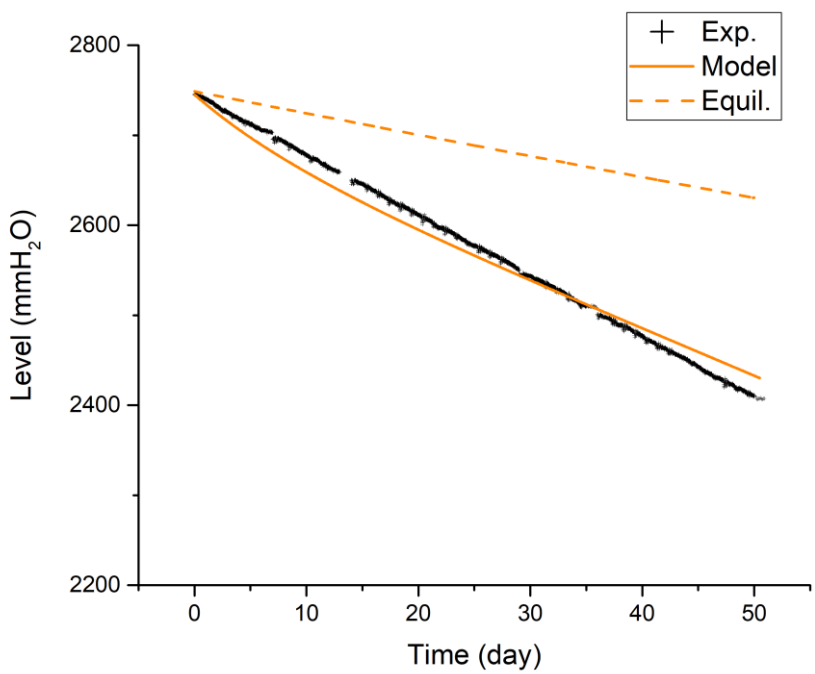

Figure 2-14. Comparison of conventional model and developed model.

2.4. Conclusion

This paper proposed a new model for the simulation of the weathering phenomenon of LNG storage tanks under isobaric storage. The proposed model implements a net mass transfer equation that uses the SRT with an empirical parameter and a net heat transfer equation that integrates heat exchange at the interface. The results were validated by an experiment, which was conducted using LNG in a vacuum-insulated cylindrical Type-C tank with a total capacity of 50 m^3 over the span of 50 days. Comparing with the experimental results showed that the proposed model predicted the BOR of LNG, the temperature change of LNG, and the composition change of the BOG successfully and could be used in a scenario in which there is a certain temperature difference between the phases. Because this model predicts storage tank behavior without modeling the NG zone, it has an advantage in industrial applications where it is impossible to install many thermocouples to measure the temperature of the interfacial phase at exact locations in all height ranges.

Chapter 3. Hydrogen Distribution

3.1. Computational model description

To solve ordinary differential equations, an explicit Euler method was applied. In this study, all thermodynamic and transport properties were calculated using REFPROP 10.0 released by the National Institute of Standards and Technology (NIST) [98], and the developed model was written in MATLAB. To simulate the thermodynamic behavior of HRS, the 0D developed model applied the law of conservation of mass and energy for the transient open system, which neglects macroscopic kinetic and potential energy [99]. Basically, all unit operation (e.g., compressor, heat exchanger, tank, and valve) developed in the model follows Eqs. (3-1) and (3-2) with proper assumptions.

$$\frac{dM}{dt} = \dot{m}_{in} - \dot{m}_{out} \tag{3-1}$$

$$\frac{dU}{dt} = \dot{m}_{in} \cdot h_{in} - \dot{m}_{out} \cdot h_{out} + \dot{Q} + \dot{W} \tag{3-2}$$

Since the specification of the compressor has a significant effect on the HRS operational performance, compressor modeling was performed rigorously based on the detailed thermodynamic equations below. The compressor represented here focused on the volumetric compressor (i.e., reciprocating compressor) that has a wide range of operating pressure that is satisfied with the operating range of a typical HRS. Work done on the hydrogen by the compressor was calculated by Eq. (3-3) with an adiabatic compression assumption.

$$\dot{W}_{comp} = \dot{m} \cdot (h_{dis} - h_{suc}) \tag{3-3}$$

The mass flow rate of the reciprocating compressor was calculated by Eq. (3-4)

which contains the volume of the compressor cylinder ($V_{cyliner}$), volumetric efficiency (E_V), and piston stroke per second (n).

$$\dot{m} = \rho_{suction} \cdot V_{cyliner} \cdot E_v \cdot n \tag{3-4}$$

Volumetric efficiency is an important variable that affects the capacity of the reciprocating compressor for a given compressor cylinder volume. Volumetric efficiency was given by Eq. (3-5), where a is the valve losses (4% in this study as manufacturer's recommendation), R is the compression ratio (P_{dis} divided by P_{suc}), C is the cylinder clearance as the percent of cylinder volume, k is the ratio of specific heats (C_p divided by C_v), Z is the compressibility factor [100]. According to Ref. [101], when the discharge pressure increases with the suction pressure remaining constant (compression ratio increases), the volumetric efficiency decreases (actual capacity decreases). On the contrary, when the suction pressure increases with the discharge pressure remaining constant, the volumetric efficiency increases.

$$E_V = 100 - a - R - C\left[\left(R^{\frac{1}{k}}\right)\left(\frac{Z_{suc}}{Z_{dis}}\right) - 1\right] \tag{3-5}$$

Typical isentropic efficiency was expressed by the function of compression ratio (Eq. (3-6)) [102]. The allowable range of compression ratio for this equation is about 1.1 to 5. Although this efficiency would be affected by other factors (e.g. oil-free type, rotating speed, valve characteristics), it is suitable for reflecting the trend of compressor characteristics influenced by the compression ratio [102].

$$\eta_{is} = 0.1091 \cdot \ln(R)^3 - 0.5247 \cdot \ln(R)^2 + 0.8577 \cdot \ln(R) + 0.3727 \tag{3-6}$$

The enthalpy of the discharge was calculated by Eq. (3-7) with isentropic compression work ($\dot{W}_{comp,is}$)

$$h_{dis} = h_{suc} + \frac{\dot{W}_{comp,is}}{\eta_{is}} \tag{3-7}$$

Note volumetric efficiency and isentropic efficiency, which have a great impact on the performance of the compressor are varied depending on the type of the compressor and manufacturer.

The discharged hydrogen from the compressor was cooled in the heat exchanger by cooling water. Required cooling energy ($\dot{Q}_c$) was given by Eq. (3-8) following newton's cooling law.

$$\dot{Q}_c = \dot{m} \cdot (h_{in} - h_{out}) \tag{3-8}$$

Eq. (3-9) transforms thermal energy into electric energy, where COP_w, the performance of the cooling water unit, was 3.125, when the evaporation temperature is 5ºC and the condensation temperature is 40ºC given by a manufacturer [62].

$$\dot{W}_w = \frac{\dot{Q}_c}{COP_w} \tag{3-9}$$

Likewise, the required cooling energy of the precooler was calculated by Eq. (3-10). Because we applied SAE J2601 refueling protocol of T40, where -40ºC cooling of the hydrogen is required, COP_p was expressed as Eq. (3-10) with ambient temperature (T_{amb}, ºC) [103].

$$COP_p = 1.6^{-0.018 \cdot T_{amb}} \tag{3-10}$$

Generally, the buffer storage tank follows Eqs. (3-1) and (3-2) as an open system equation without shaft work. However, the outlet boundary of the vehicle tank changes into the close system that has only inflow. Energy balance of the tank was implemented in the developed model by rewriting the equation into Eq. (3-11) using $U = H - PV$

$$\frac{dH}{dt} = \left(\dot{m}_{in} \cdot h_{in} + V \cdot \frac{dP}{dt} + \dot{Q}\right) \quad (3\text{-}11)$$

where flow work term in enthalpy transforms into internal energy [99]. Even though heat transfer ($\dot{Q}$) can be calculated by rigorous modeling with detailed dimension of the tank and material characteristics (e.g., thermal conductivity, density, heat capacity), we simply considered natural convection of the outer vehicle tank surface as external heat transfer coefficient ($5\ W/m^2\text{-}K$) corresponding to the ambient environment; The external heat transfer during refueling rarely affects the thermal behavior of the storage tank because of a short period of refueling [50].

According to the SAE protocols, when hydrogen is injected into the vehicle tank, APRR is generally constant. Thus, a proportional-integral (PI) controller for the dispenser was implemented so that valve can be manipulated automatically to maintain APRR. The ending line of the HRS (before break-away) was the spot of measuring pressure and feedback control was achieved using this pressure [104].

Pressure losses in the HRS were simplified into the prime two points. One is a control valve where a large pressure drop arises to maintain APRR from the buffer storage tank and the other is between break-away and nozzle before the vehicle tank. Since detailed information on pipes and fittings could not be obtained, and pressure loss due to the friction is negligible compared to the major pressure losses, only two pressure losses were considered. The pressure loss of the control valve which is a function of valve flow coefficient (CV), was determined dependently by the APRR. And the pressure loss between the break-away and nozzle was estimated as a CV value by examining the trend of the pressure difference between the station and the vehicle using the operating data shown in section 3.2.

3.2. Model validation using operational data

In this section, the developed thermodynamic equations and assumptions presented in section 3.1 were validated by comparing simulation results with operating data of HRS located in South Korea. For the sake of convenience, validation was performed using ASPEN HYSYS V11 Dynamic mode. In addition, the MBWR equation of state (EOS) was chosen for estimating the thermodynamic properties of normal hydrogen. The estimated value of density and enthalpy by the MBWR were sampled by increasing 50 bar from 50 bar to 1000 bar and increasing 5ºC from -40ºC to 80ºC. All the samples were compared with REFPROP calculation results, and the mean absolute percentage error (MAPE) is the average of the absolute difference between each estimated value divided by the REFPROP calculation value. To prevent the denominator of MAPE from being zero, the delta enthalpy values were compared, and the reference state is 1 bar and -50ºC. Because MAPE of density was 0.0946% and MAPE of enthalpy was 0.044%, using MBWR for the simulation was applicable instead of using REFPROP.

Figure 3-1 shows the simulation results as denoted by the solid lines, along with the operating data as denoted by the scattered circle and the values of each item were expressed in the same color. Figure 3-1(a) results show the pressure profile of the high pressure (HP), medium pressure (MP) tank, and tube trailer, and these values were normalized by the design pressure of the highest pressure tank. The yellow shaded area refers to the refueling period and the green shaded area refers to the pressure recovery period after finishing refueling. During the refueling period, both the pressure of the buffer storage tank decreased to fill the vehicle tank and the pressure of the HP tank oscillated. During the pressure recovery period, the

compressor replenished the buffer storage bank in the order of high to low pressure. Since the volume of the tube trailer was large enough, the pressure change of the tube trailer was small (less 5 bar) during the whole operation, so the operating data and simulation results were almost overlapped. When calculating the absolute percentage error (APE) of the simulation results at the last point of the graph with respect to the operating data, the APE of pressure for each HP, MP tank, and tube trailer was 0.73%, 1.36%, and 1.34%. Because, in the figure, the pressure of the buffer storage tank at the last point returned to near its initial state, the developed model can simulate pressure recovery of the buffer storage tank for the entire operating time frame.

Figure 3-1(b) shows the pressure profiles of the vehicle and station (ending line of HRS, before break-away). The pressure drops and small holdup volume (e.g., heat exchanger and pipe) were roughly fitted in the model by the matching pressure profiles of station and vehicle in operating data. During refueling, two horizontal lines were observed, and those are an intermediate pressure leak check which was performed twice, when a certain pressure rise, as specified in the SAE protocols. However, there was a slight difference in the timing of the leak check because the pressure increase rate in the simulation was different from the actual operating data.

Figure 3-1(c) shows the temperature profiles of the vehicle tank. At the beginning of filling, the difference in the temperature profile widened a bit, because only the isothermal discharge (T40) assumption of the precooler was applied in the model, which did not consider the effect of cooldown of the warmer process line until the thermal equilibrium reaches. However, the temperature gap narrowed as refueling continued.

Both simulation and operating data stopped filling at SOC 95%, which is a function of the pressure and temperature as shown in Figure 3-1(a-b). Technically the pressure and temperature in the vehicle tank are thermodynamically coupled. Although the trends of temperature and pressure in the vehicle tank were somewhat different, the amount of filling hydrogen was the exact same and there was a small difference in the filling time (less than 8 seconds, APE 3% in this simulation). This developed model, which simply calculated heat transfer, can be considered valid in analyzing the performance of the HRS, which was our main interest in this study.

In summary, the developed model showed good agreement with actual operating data and can evaluate the performance of HRS, which contained the whole sequence of hydrogen filling and the pressure recovery, for the entire operating time frame to investigate design variables and develop design methodology.

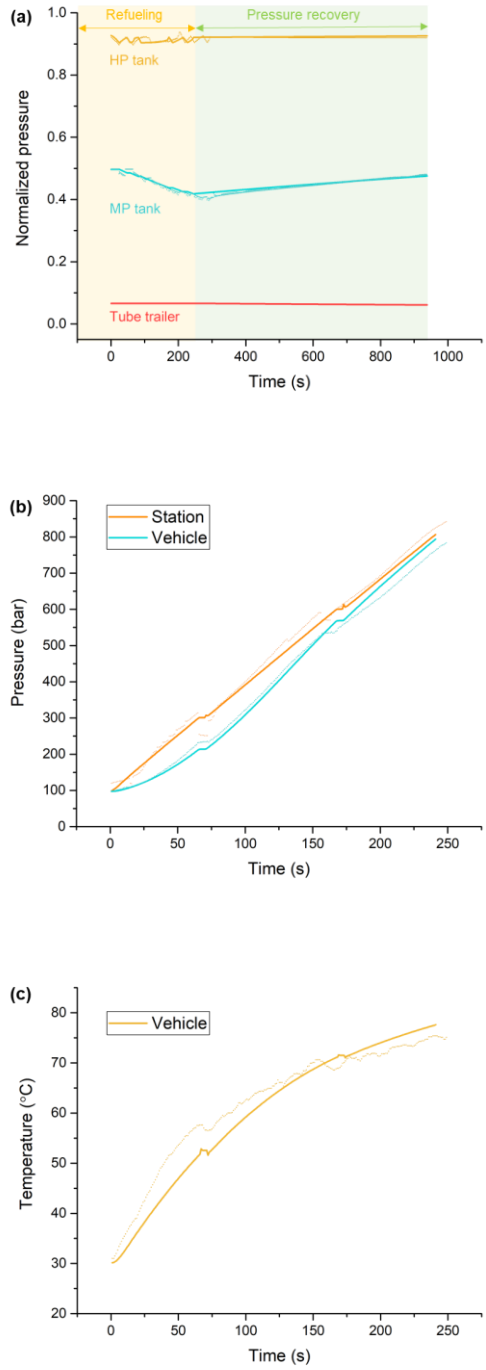

Figure 3-1. Profiles of operating data and simulation results (a) pressure of HRS facility (b) station and vehicle pressure (c) vehicle temperature.

3.3. Development of design methodology

3.3.1. Overall design methodology of HRS

This study proposed a novel design methodology using the design variables of main HRS components through extensive literature reviews, as shown in Figure 3-2. As discussed in the research background, previous studies identified compressor and buffer storage tank as the main HRS components, and the design variables of buffer storage tank were the number of stages, each stage pressure, and each stage volume.

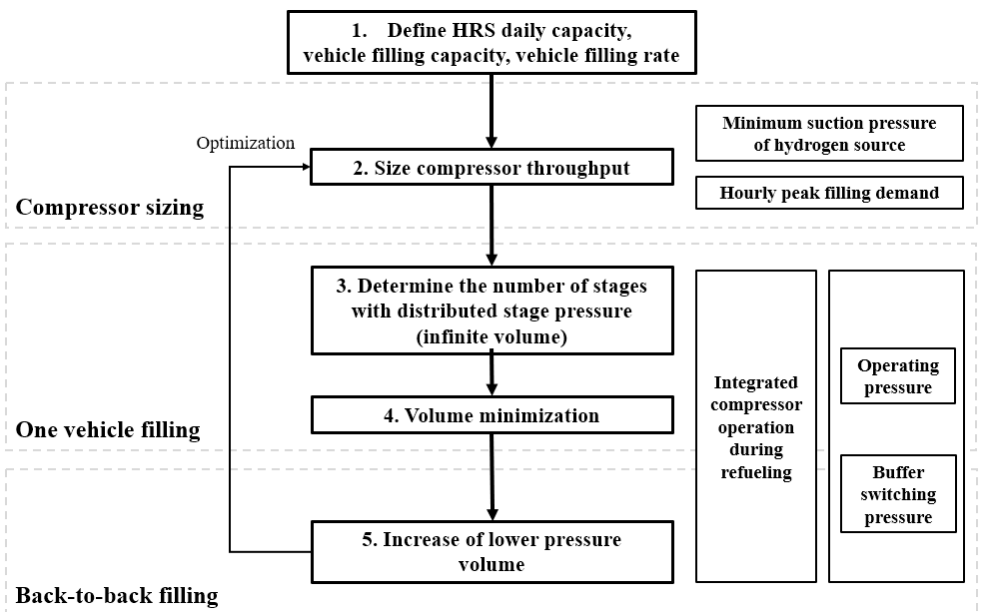

Figure 3-2. Overall HRS design procedure.

First, define HRS daily capacity and specification of FCEV (vehicle storage volume and filling rate given by SAE J2601 Protocols). Second, compressors should be sized properly according to the available supply pressure of the tube trailer and the required peak filling demand. Third, design a buffer storage system for one vehicle filling. It is performed by searching the number of stages with distributed

stages with infinite volume for reducing energy consumption. And then, the volume of each stage is reduced to decrease the capital investment cost. In this study, we proposed a method to increase the volume indirectly to maintain the filling pressure of the buffer tank by operating the compressor during refueling. Finally, the total volume of buffer storage can be estimated from the number of consecutive fillings of the vehicle, called a back-to-back filling. This scenario has insufficient pressure recovery time to return the initial status of a buffer storage tank. Thus, the size of the buffer volume is inevitably increased. Because all constraints are satisfied after this procedure, design optimization of HRS for saving CAPEX and OPEX could be performed.

3.3.2. Design variables of buffer storage system

Figure 3-3 shows the graphical description of the design variables of a buffer storage system. Design variables were as follows: the number of stages of the buffer storage tank, initial pressure of each tank, volume of each tank, switching pressure to the next tank, and operating pressure range of each tank. The design variables mainly have an impact on minimizing the pressure difference between the station and vehicle tank to reduce energy consumption concerning the filling rate given by SAE protocols. The major variables for reducing the pressure difference were the number of the stage with the initial pressure of each tank. And the volume of each tank played a role to create the slope of the pressure profile for each tank in Figure 3-3. However, the optimal volume of the tank should not be for filling one single vehicle, a back-to-back filling as an actual constraint should be considered with compressor capacity. As a most extreme case, a back-to-back filling scenario was assumed 3 minutes as a linger time when the next vehicle comes [50].

Besides the three design variables suggested in previous studies, two additional variables were added as design variables in this study: switching pressure to the next tank and the operating pressure range of each tank. Bai et al. [105] investigated the switching point of the cascade buffer system for fast filling concerning the initial condition of the vehicle. However, we assumed that a 50 bar pressure difference between the buffer storage system and vehicle tank is the time to switch to a higher pressure buffer; 50 bar was estimated from the validated model in section 3.2. If the pressure difference is less than 50 bar, it is difficult to overcome a pressure drop in the process line. Thus, the filling rate cannot follow the APRR, which causes a delay

in the refueling time, or a problem in the behavior of the control valve when replacing the pressure vessel with the higher pressure one late. Conversely, if the buffer tank is switched earlier, the total energy consumption became large because unnecessarily high-pressure hydrogen was used for refueling.

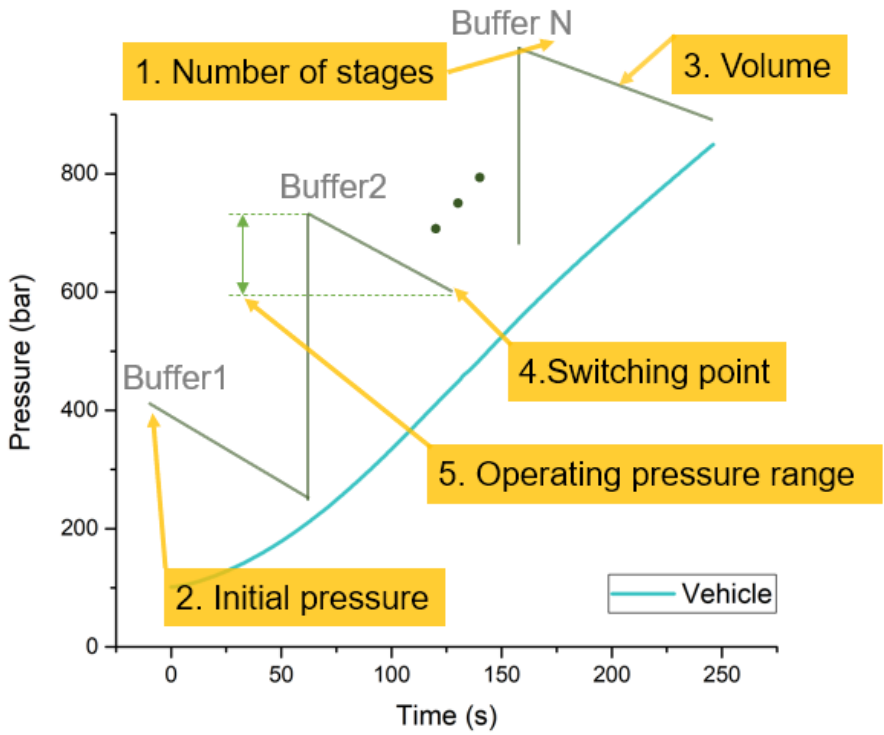

Figure 3-3. Graphical description of design variables of buffer storage system for one vehicle filling.

To improve the lifetime of the cylinder, the operating pressure limit of the cascade buffer system needs to be considered. Hydrogen reduces fatigue and fracture resistance of structural steels [106]. Typical gas cylinders experience less pressurization and depressurization cycle compared to the cylinders of buffer tanks which experience pressure cycle for every vehicle filling [107]. Moreover, the amplitude of pressure cycle influences the fatigue life of the cylinder; As the amplitude of the pressure cycle is greater, the tolerable fatigue life is reduced which

means the shallow pressure cycle of cylinders is a better option concerning design lifetime [108]. Figure 3-4 shows the average number of the allowable cycle of a Type 2 cylinder according to the pressure amplitude. Considering the assumed design life (20 years) of a 250 kg/day refueling station, where approximately 35,000 times of charging and discharging occur for 20 years, so 300 bar was the allowable pressure amplitude range obtained by using the regression equation fitted by the experimental data. Thus, when the operating limit of 300 bar reaches during refueling, the lower pressure cascade tank should be switched to a higher pressure level tank, otherwise, the cylinder will be failure earlier than its design life.

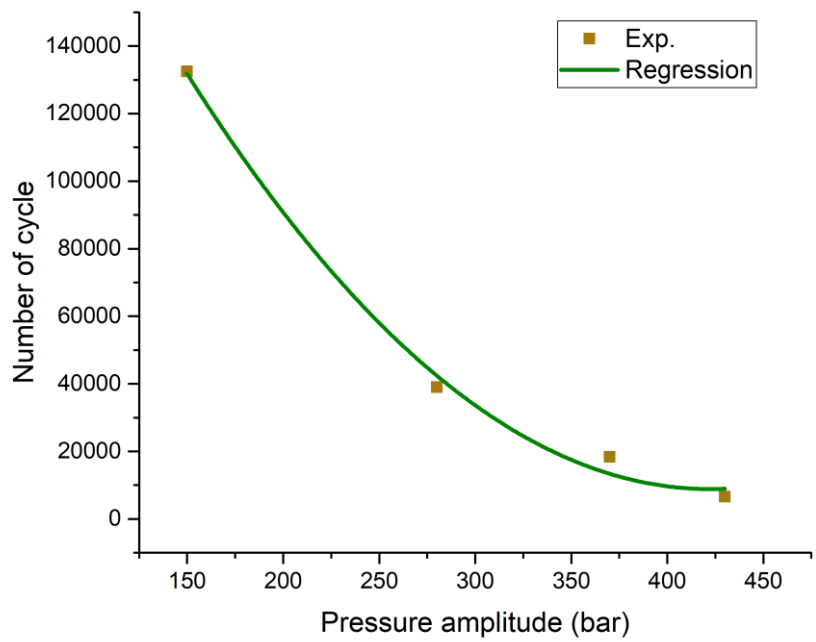

Figure 3-4. Average number of the allowable cycle with respect to pressure amplitude for Type 2 cylinder.

3.4. Investigation of design procedure

3.4.1. Compressor design

As a first design step, sizing of the proper capacity of the compressor was performed with respect to the hourly peak demand profile and hydrogen source availability concerning predefined daily HRS capacity. Note we did not consider any on-site hydrogen productions so that only a tube trailer can supply hydrogen to the HRS. Since the flow rate of discharged hydrogen decreases as the suction pressure of the compressor decreases, when the operating pressure range of the tube trailer is specified, the required throughput of the compressor is determined by consideration of an available lowest suction pressure of the tube trailer. For example, Ref. [109] showed that hourly peak filling demand can be assumed at 20 kg/hr for 250 kg/day HRS capacity. And an available lowest suction pressure can be assumed typically 50 bar, which was established from the minimum allowable suction pressure of compressor or optimization results between HRS capacity and tube-trailer delivery scenario. Thus, compressor capacity was calculated based on the required throughput (20 kg/hr) to recover the pressure of the buffer storage system. The reference case for compressor sizing assumed that compressor did not operate during refueling. During an hour, each vehicle will refuel the amount of 5 kg hydrogen as shown in Table 3-1 for 4 minutes according to the filling rate. Therefore, compressor capacity was calculated based on the idle time (no refueling time), and only 44 minutes would be an available time to recover the pressure of the buffer storage system at the peak demand.

In this study, this model was implemented in a two-stage reciprocating

compressor with a cylinder clearance (10%) and isentropic efficiency (Eq. (3-6)) that has a maximum compression ratio of up to 5. We set the proper capacity of the compressor by defining cylinder volume and rotating speed together with respect to the peak demand for a 250 kg/day station. Each stage cylinder volume ratio was 4:1 to avoid overheating of discharge and interstage temperatures. Because of the higher compression ratio from the lowest suction pressure (50 bar at the tube trailer) to 950 bar, two-stage reciprocating was connected as a series. Figure 3-5 shows a performance chart of the designed reciprocating compressor at the minimum suction pressure.

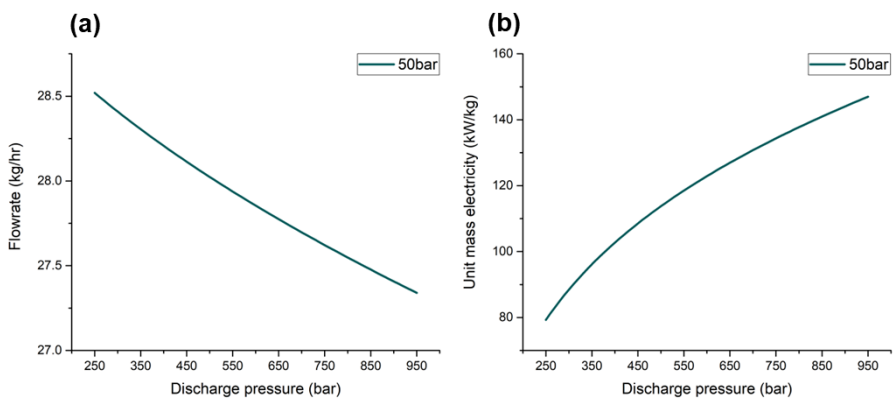

Figure 3-5. Performance chart of designed reciprocating compressor.

The simulation assumptions of each vehicle and station specification were summarized in Table 3-1. During filling one vehicle by 5 kg, the discharge pressure of the tube trailer decreased by approximately 5 bar. Therefore, the pressure of the tube trailer was assumed to be constant for simplicity of calculation for this study, as it did not significantly affect compressor throughput.

A suggested control logic for compressor operation during refueling was that the compressor started to operate when the pressure of the buffer tank decreased by 10

bar compared to the initial pressure of the buffer tank when the pressure of the tube trailer was near 50 bar. However, when the suction pressure of the tube trailer was high, the compressor can recover the pressure of the tank faster than the filling rate of the vehicle, so it is better to lower the starting pressure of the compressor. Pressure recovery sequence was performed from higher to lower pressure buffer tank to prepare the next coming vehicle.

Table 3-1. Simulation assumptions.

Vehicle information	
Initial vehicle pressure (bar)	100
Initial vehicle temperature (ºC)	25
Vehicle tank volume (m^3)	0.156
Filling amount (kg)	5
Station information	
HRS capacity (kg/day)	250
Precooler discharge temperature	T40
Maximum operating pressure of Tube trailer (bar)	200
Minimum operating pressure of Tube trailer (bar)	50
Ambient temperature (ºC)	25
Cascade buffer tank material	Type2
Cascade maximum operating range (bar)	300
Cascade switching pressure (bar)	50
Lingering time (min)	3

3.4.2. Number of stages and initial pressure

As a second design step, design a buffer storage system for one vehicle filling. First, we analyzed the most important parameters (the number of stages and each of these initial pressure) to reduce energy consumption. As the number of stages increased from 1 to 10, the pressure was increased by the following formula, where P_{min} is 200 bar, P_{max} is 950 bar, *i* is the *i*-th stage, and *N* is the total number of stages.

$$\mathrm{P_i} = P_{min} \cdot \left(\frac{P_{max}}{P_{min}}\right)^{\frac{i}{N}} \tag{3-12}$$

Figure 3-6 shows total energy consumption depending on the number of stages when the pressure of the tube trailer was 50 bar, and each volume of the tank was assumed 100 m^3 as an infinite volume. As the number of stages increased, total energy consumption was reduced logarithmically. The consumption of energy from the compressor accounted for more than 50% and decreased more compared to that of cooling as the number of stages increased. In addition, precooler energy consumption decreased with the increased number of stages. Because when hydrogen passed through the control valve, the amount of temperature rise was reduced which is caused by the negative Joule-Thomson coefficient. Thus, using a cascade storage system compared to one buffer storage tank was efficient from an energy consumption point of view when the cascade tank volume was enough.

As the number of stages increased, the influence on the initial pressure decreased. Compared to the one stage, the energy efficiency of the four stages was improved by 20%, but the energy saving portion from the four stages to the ten stages was enhanced only by 5%. Even if the number of stages of the cascade storage system was increased by investing more capital cost, there was a limit to the amount of

energy that can be saved. We agreed with the previous study demonstrating that 3 to 4 stages would be sufficient [63]. Therefore, this study decided that 4 stages with well-distributed initial pressure were sufficient for designing a buffer storage system.

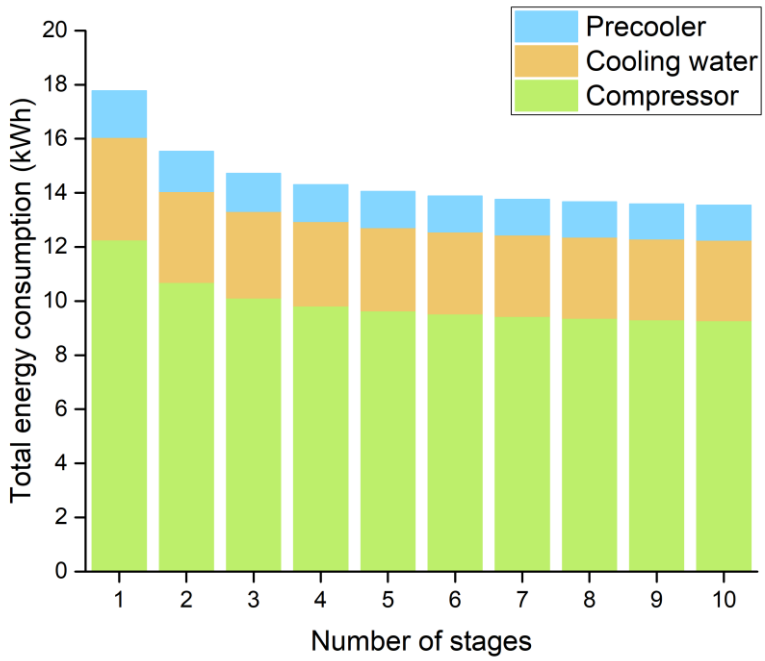

Figure 3-6. Total energy consumption depending on the number of stages.

3.4.3. Sizing volume of buffer tank for one vehicle filling

Even if the number of stages was sufficient and the initial pressure was distributed well, if the filling pressure of the buffer tank was not properly maintained, there will be a problem with filling completion. In addition, if the volume of each tank was small, it was replaced with a tank having a pressure of the next higher level, and therefore, the pressure difference between the buffer tank and the vehicle tank increased sharply in a state with a finite number of stages. Furthermore, the small volume threatened the fatigue life of the tank. However, increasing the volume of the buffer storage tank caused an increase in capital cost, so the appropriate volume should be designed carefully. Thus, this analysis applied a suggested method to increase the volume indirectly to maintain the filling pressure of the buffer tank by operating the compressor during refueling.

Table 3-2 shows the minimum required volume depending on compressor operation during refueling for one filling vehicle. As a suggested control logic, the compressor ran when the pressure of the buffer tank decreased by 10 bar compared to the initial pressure. The minimum required volume was determined by checking whether vehicle filling was complete while the volume was reduced by 0.1 m^3 for each stage.

Table 3-2. Minimum required volume and energy consumption depending on compressor operation during refueling.

Comp Off	Stage1 bar	Stage2 bar	Stage3 bar	Stage4 bar	Volume m^3	Energy kWh	Time min.
1	950				2.5	17.603	10.98
2	500	950			1.3	15.562	10.84
3	400	650	950		0.8	14.855	10.80
4	300	600	800	950	0.5	14.652	10.79

Comp On	Stage1 bar	Stage2 bar	Stage3 bar	Stage4 bar	Volume m^3	Energy kWh	Time min.
1	950				1.8	17.586	7.68
2	500	950			0.9	15.554	7.37
3	400	650	950		0.6	14.847	7.22
4	300	600	800	950	0.3	14.650	7.05

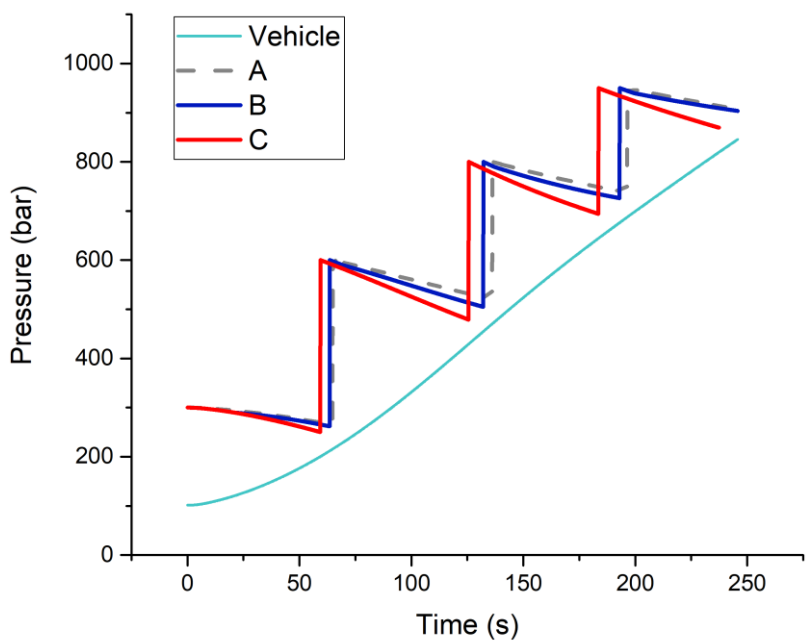

Figure 3-7. Pressure profile for analyzing the effect of compressor operation.

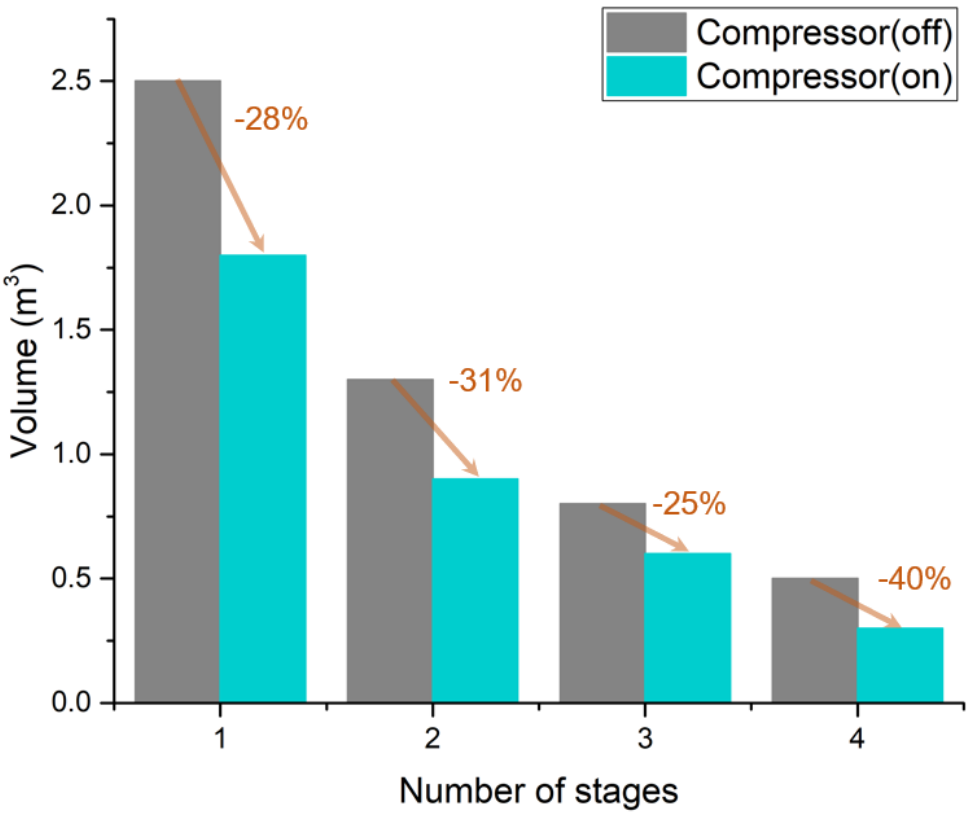

Figure 3-8. Results of volume analysis according to compressor operation.

Figure 3-7 shows the pressure profile for analyzing the effect of compressor operation. (A) was 4 stages without compression operation in Table 3-2, (B) was 4 stages with compressor operation, and (C) was the same as (B) except for compressor operation. Compared to (A) and (B), even if the volume in case (B) was reduced by 40%, it finished refueling completely by the compressor operation. As you can see in case (C) in Figure 3-7, Because the tank volume was small and the compressor did not run, tank switching occurred quickly, a higher pressure level tank was used early and it cannot refuel the vehicle completely.

Figure 3-8 shows the results of volume analysis according to compressor operation. By operating the compressor during refueling, it had the effect of

indirectly increasing the volume of the tank for each pressure level. The volume of the tank can be reduced by from 25 to 40% depending on the number of stages compared to no operation of the compressor during refueling. As shown in Table 3-2, the difference in energy consumption was almost the same whether the compressor was running or not. In addition, compared to the energy consumption of infinite volume shown in Figure 3-6, there was an increment in energy consumption by about 1%. Therefore, filling the vehicle by operating the compressor showed an advantage in reducing the capital cost due to a reduction in the volume of the buffer tank without a large energy consumption increase.

Figure 3-9 shows the pressure profile of 3 stages depending on the operation compressor. Another advantage of operating the compressor while the filling was well expressed in this figure. By using the compressor during refueling, the time it takes to return to the initial state after refueling was reduced. Also, when the compressor was used during refueling, the saving time can be used to reduce the size of the compressor. Roughly, the size of the compressor can be reduced by 22% for one vehicle analysis. Therefore, it was possible to reduce the size of the compressor by increasing the utilization rate of the compressor through simultaneous compressor operation during refueling.

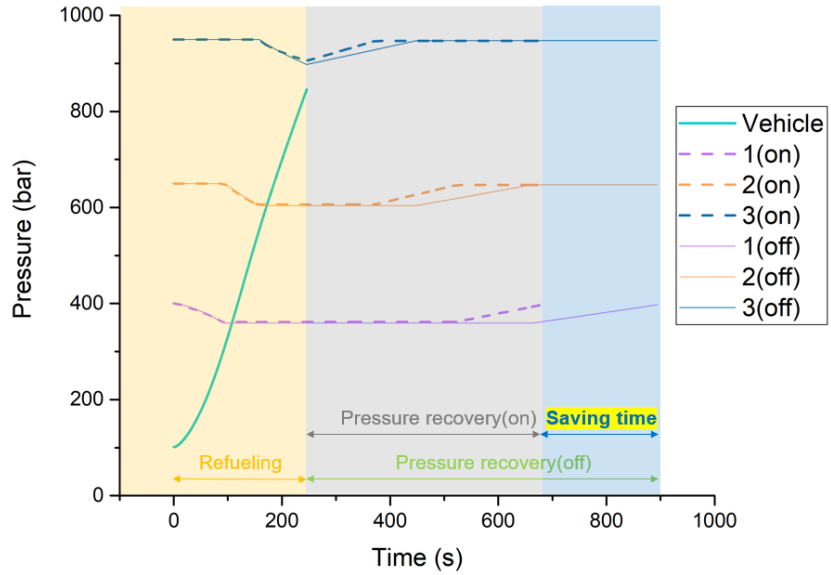

Figure 3-9. Pressure profile of 3 stages depending on operation compressor.

3.4.4. Sizing volume of buffer tank for back-to-back filling

According to Figure 3-9, after the vehicle refueling was completed, the compressor recovered the pressure from the high-pressure tank first and prepared to refuel the next vehicle. The highest pressure tank returned to the initial pressure during the lingering time (3 min.), but the remaining low-pressure tanks did not. So, in order to do back-to-back filling, it is necessary to increase the volume of the lower pressure tank that cannot be recovered by the compressor.

Thus, its step starts from each volume of buffer storage for 4 stages (0.3 m^3) given by one vehicle filling described in section 3.4.3. Figure 3-10 shows the pressure profile of back-to-back filling at the peak demand of 250 kg/day HRS with the 50 bar tube trailer. Back-to-back filling was performed at the lingering time interval of 3 minutes. Through analysis, each volume of tanks was defined as 0.9, 0.9, 0.3, and 0.3 m^3 from the lower level pressure tank, where only 1st and 2nd pressure vessels were increased compared to Table 3-2 (0.3 m^3 is a typical bundle of buffer volume). After the first vehicle refueling plus lingering time, the compressor can recover the high-pressure tank in the 4th and 3rd stages fully, and the 2nd stage was partially recovered at the time the next vehicle arrived. Thus, the volume of the lower level pressure tank must be increased inevitably. Compared to the study of Yu et al. [63], in this study, the HRS design that satisfied peak filling demand demonstrated the size of the compressor was reduced by 36%, and the total volume of buffer storage was decreased by 20%. Average energy consumption per vehicle compared to an infinite volume of 4 stages increased by 0.35%

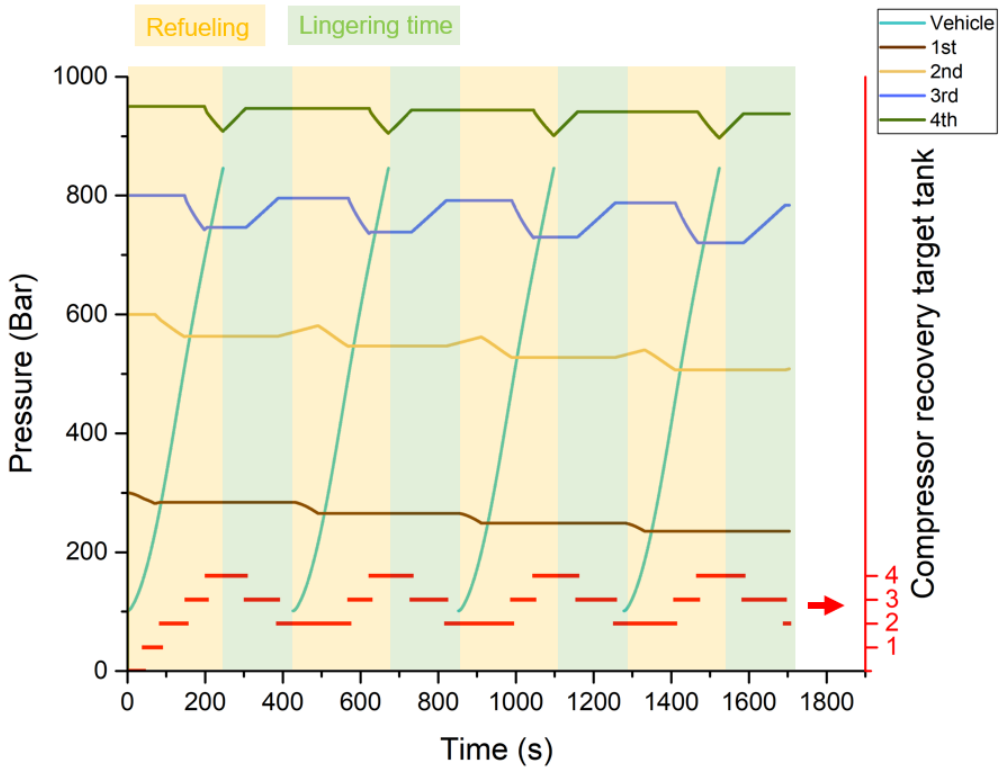

Figure 3-10. Pressure profile of back-to-back filling scenario (4 vehicles).

3.5. Conclusion

This study investigated the complicated interdependency of the design variables of main HRS components and proposed a novel design methodology for the improved design of the HRS considering all actual constraints. To verify the performance of the HRS, we develop a 0D dynamic simulation model covering the whole sequence of the HRS which was validated by operational data. Based on the validated model, we suggested a basic design guideline as follows.

1. With defined HRS capacity and vehicle, a compressor should be sized concerning fill-up demand and available pressure of hydrogen source and can operate during refueling to reduce the size of a buffer storage volume.
2. Next, a buffer storage system is designed using 5 variables to reduce energy consumption and complete back-to-back filling: the number of stages, initial pressure of each tank, volume of each tank, switching pressure to the next pressure level tank, and operating pressure range of each tank.
3. Depending on the performance of the compressor, it is not necessary to increase the whole volume of the buffer storage tank because it is recovered to some extent in the back-to-back filling scenario, and it is required to increase the size volume of the lower pressure level.
4. 4 stages of the cascade buffer system with well-distributed initial pressure levels are the efficient stages to reduce the capital and operating costs.

Chapter 4. CO_2 Conversion[2]

4.1. CFD modeling

4.1.1. Mesh generation

A CFD model for the flow channel and the GDL (Gas diffusion layer) is developed based on the finite volume method. First, the 3-dimensional grid elements are created to define the computational domain. A high-quality non-conformal mesh for two separate bodies of the flow channel and GDL was configured as shown in Figure 4-1. Two separate bodies for the flow channel and GDL were meshed with different topologies, and their contact surfaces were managed for interface boundary through which mass, momentum, and energy are interchangeable between two non-conformally shared surface meshes. With the base element size of 2×10^{-4} m, sweep methods were applied for mesh generation of the two bodies with the number of divisions of 15. By means of sweep methods, conformally constant meshes are generated from source surface to the target surface, and high accuracy solution with minimal cell counts can be achieved. In CO_2RR reactor modeling, abrupt momentum change is expected between two bodies and as a result, numerical instability can be encountered near the interface surface. The high orthogonality of the mesh obtained

[2] The work presented in Chapter 4 is based on Design methodology for mass transfer-enhanced large-scale electrochemical reactor for CO_2 reduction in *Chemical Engineering Journal 424 (2021): 130265* [110].

by the sweep method, therefore, can alleviate the instability issue with stable convergence of the numerical solution. The number of elements was 3,752,733 and the minimal orthogonal quality was 0.04636, confirming that the high-quality computational domain is generated.

4.1.2. Governing equations

The mass and momentum conservation in the computational domain are described with the Navier-Stokes equation:

$$\frac{\partial \rho}{\partial t} + \nabla \cdot (\rho \vec{v}) = 0 \tag{4-1}$$

$$\frac{\partial (\rho \vec{v})}{\partial t} + \nabla \cdot (\rho \vec{v} \vec{v}) = -\nabla p + \nabla \cdot (\bar{\bar{\tau}}) + \rho \vec{g} + \vec{F} \tag{4-2}$$

where ρ is the fluid density, $\vec{v}$ is a velocity vector, p is the static pressure, $\bar{\bar{\tau}}$ is the stress tensor, $\vec{g}$ is the gravity vector, and $\vec{F}$ is the external body forces. The last term in Eq. (4-2), $\vec{F}$, is used to describe the model-dependent source term for the porous GDL:

$$F_i = -(\frac{\mu}{\alpha} v_i + \frac{1}{2} C_2 \rho v_{mag} v_i) \tag{4-3}$$

where F_i is the ith (x, y, or z) component of the source term ($\vec{F}$) in the momentum equation, and α and C_2 are the permeability and the inertial loss coefficient per unit length, respectively. The first term on the right-hand side in Eq. (4-3) is the viscous loss term described with Darcy's law, and the second term is the inertial loss term. The inertial loss term can be neglected in our system due to low flow velocities ($\leq$ 5 cm/s) and the laminar characteristics (Re $\leq$ 4) in the porous media. The source term in Eq. (4-3) is incorporated only in the permeable GDL regime and set as 0 for the flow channel. The species transport equation and the energy conservation equation are also solved in the CFD model:

$$\frac{\partial(\rho Y_i)}{\partial t} + \nabla \cdot (\rho \vec{v} Y_i) = -\nabla \cdot \vec{J}_i \tag{4-4}$$

$$\frac{\partial(\rho E)}{\partial t} + \nabla \cdot (\vec{v}(\rho E + p)) = \nabla \cdot (k_{eff} \nabla T - \sum_i h_i \vec{J}_i) \tag{4-5}$$

where Y_i is the local mass fraction of species i, and $\vec{J}_i$ is the diffusion flux of species i due to gradients of concentration and temperature. In the energy equation, E is the total energy, k_{eff} is the effective conductivity, and h_i is the sensible enthalpy of species i. The species is transported through the GDL by advection and diffusion, the second term on the left-hand side and the right-hand side of Eq. (4-4), respectively. The source term for the transport of gas species has not been defined because the change in total moles is negligible ($\Delta \leq 0.8\%$), and the flow channel is operated under nearly isothermal conditions ($\Delta T \leq 0.3\ K$).

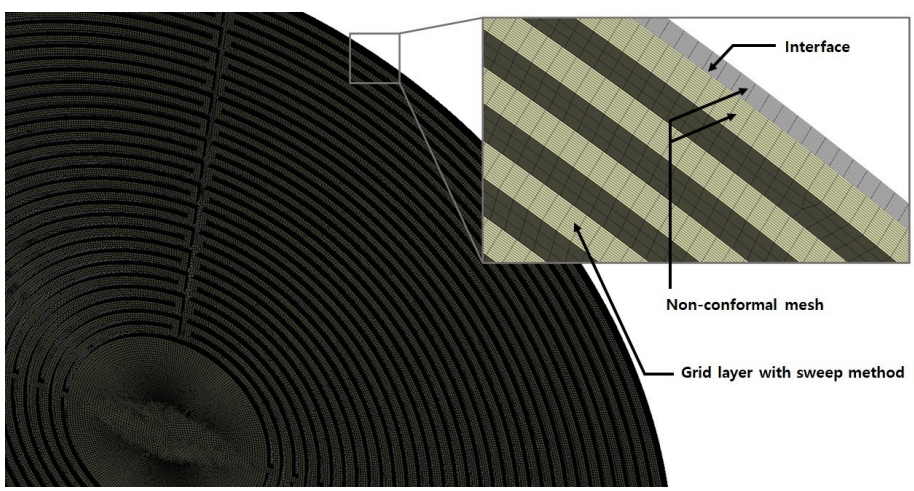

Figure 4-1. Computational domain for CFD simulation.

4.1.3. Boundary conditions

The mass flow inlet boundary conditions with constant species mass fraction (CO_2 : H_2O = 0.9872 : 0.0128) and the pressure outlet boundary conditions with zero gauge pressure were given to the inlet and outlet, respectively. The values of the mass fraction at the inlet boundary condition characterize the humid CO_2 feed, that is, fully saturated with H_2O under reaction conditions. The non-slip boundary condition (velocity = 0) was applied to all boundary walls except the interface contact between the flow channel and the GDL.

4.1.4. Solution methodology

The above-mentioned governing equations were solved using a commercial CFD simulator ANSYS FLUENT V19.2. The laminar model is adopted because low velocity ($\leq 5\ cm/s$) and low Reynolds number (≤ 4) are found elsewhere in the entire domain. The porous cell zone conditions were used to describe the viscous loss in GDL. The SIMPLE (Semi-Implicit Method for Pressure Linked Equations) algorithm with a second-order spatial discretization scheme was used for pressure-velocity coupling. Steady-state simulation was performed, and the area-weighted average of the velocity at the middle surface of the GDL (S_{mon}) was monitored during every iteration. The simulation was run until the relative residual error of the monitored value becomes less than 0.5%, and the solution converged within 3,000 iterations. The solution dependency on the mesh size (± 30%) was also investigated, and the results showed less than 0.25% differences. These mesh-size independent results confirm that the solutions obtained are numerically robust and accurate.

4.1.5. Design concept

In this study, several case studies were performed to obtain design philosophy as well as speculation of optimal design for the flow channel of the CO_2RR reactor. Eight representative designs shown in Figure 4-2, each of which possesses its own design concept, were selected for the case study, and their CFD simulation results are compared based on the established design criteria, where G_1 is a fractal structure, G_2 is flow retrace, G_3 is flow retrace with flow split, G_4 is flow segmentation with flow retrace, G_5 is one-path flow, G_6 is flow segmentation, retrace with GDL extension, G_7 is flow segmentation with one-way convection, and G_8 is intensified flow segmentation with convection enhancement. The color in the figure presents one individual flow channel, i.e., design G_1 to G_3 are comprised of four separate individual channels, whereas G_4 to G_8 consist of a single connected channel. In the figure, the alphabetic G_1 to G_8 numerically given with increasing u_{avg}. Therefore, resulting u_{avg} of design G_1 is minimal, the worst case, whereas the design G_8 is maximal, the optimal case.

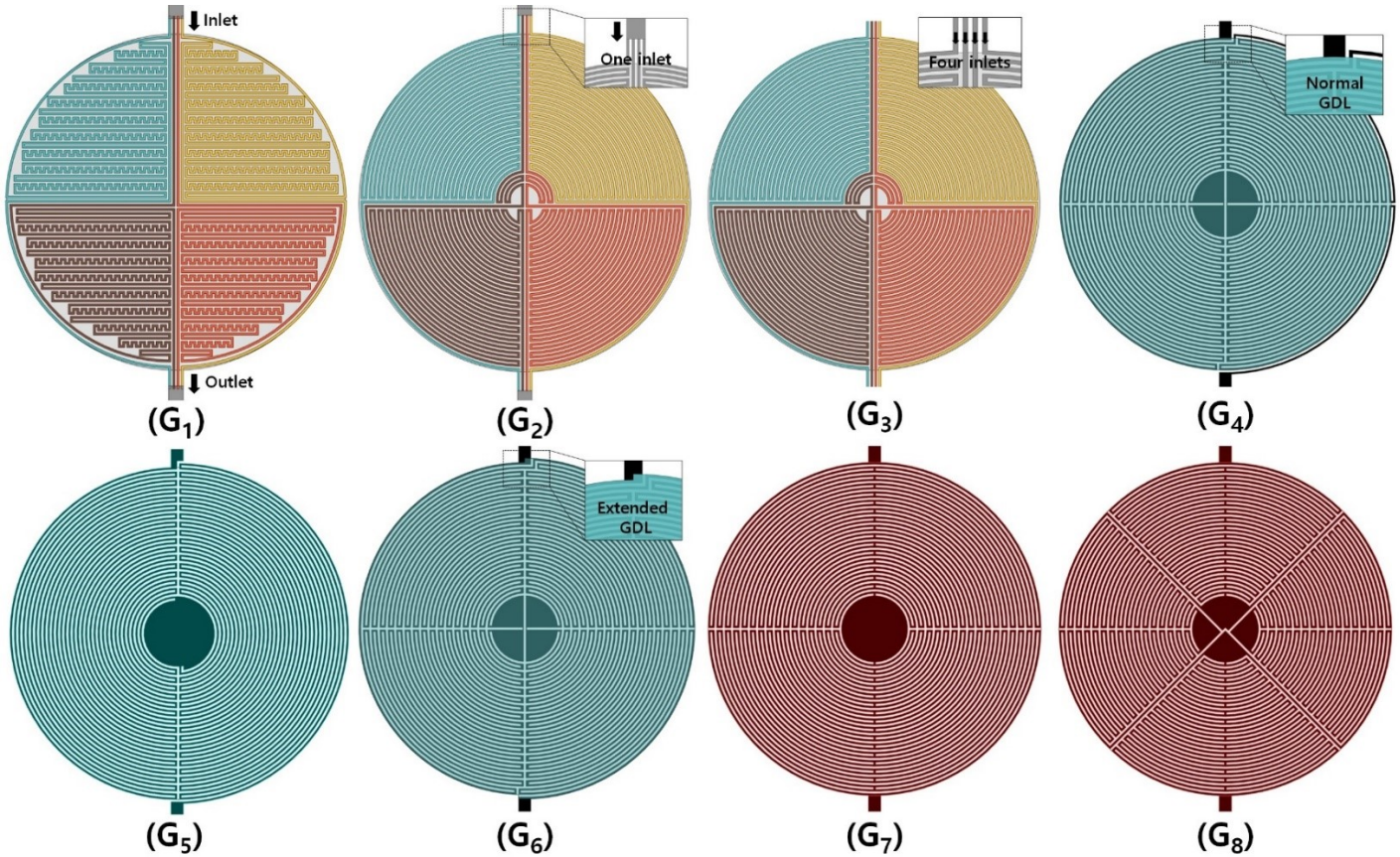

Figure 4-2. Flow channel designs selected for case studies.

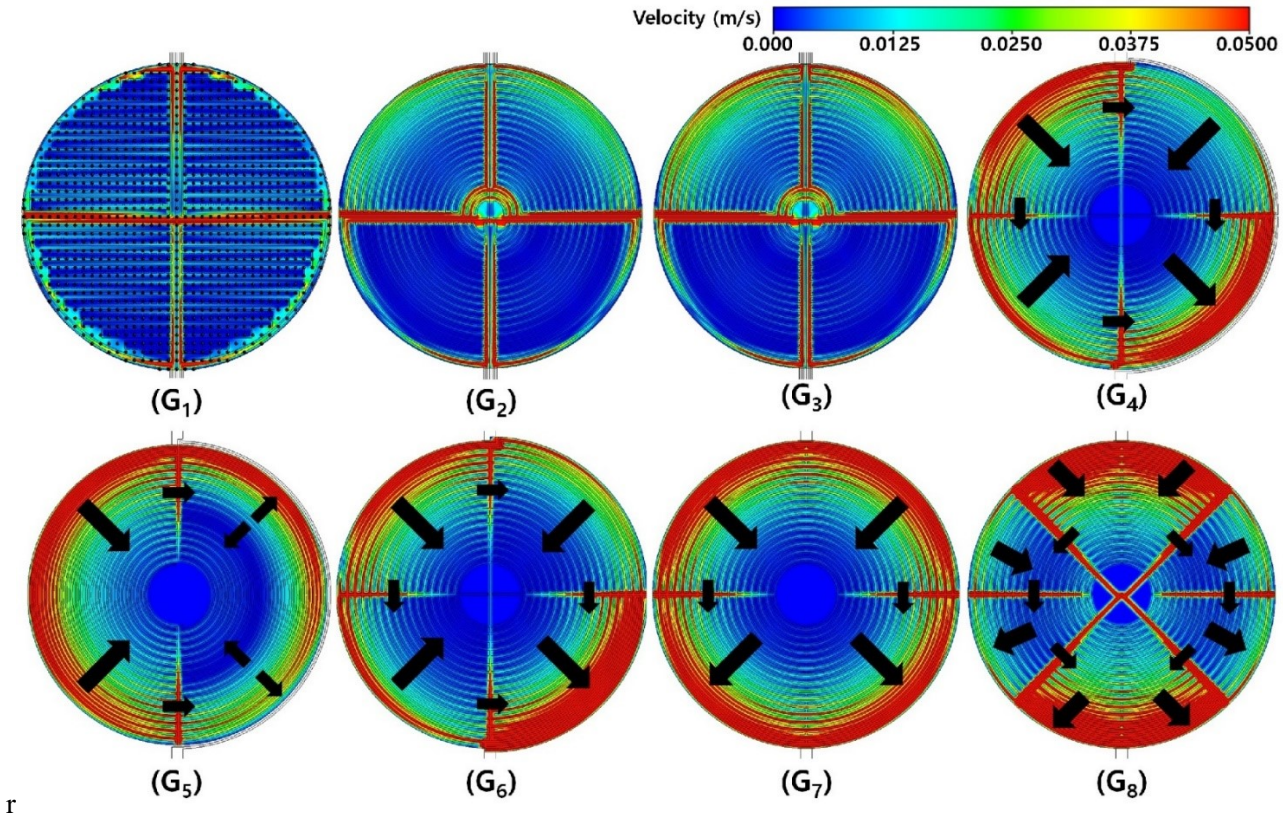

r

Figure 4-3. Results of CFD simulation: velocity contour for each design geometry.

4.1.6. Design case studies

First, the geometry G_1 is configured to investigate the effect of fractal structure on the convection and flow uniformity in GDL. This concept is referred to as the fuel cell geometry idea introduced in the work of Suresh et al. [111] and reproduced for the cylindrical CO_2RR reactor. The main advantage of the fractal arrangement is that it confirms higher flow uniformity with lower pressure drop compared to the one-path configuration. Four identical separate serpentine channels were configured symmetrically, and the convective mass transport is enhanced between the channels and also between the U-shaped serpentine fragment in the channel.

As shown in Figure 4-3, the velocity at the GDL is developed by the pressure difference at the flow channel side. Flow velocity is high at the location where ΔP is high and presented as red color in the contour, whereas the velocity is low when ΔP is low and presented as blue color in the contour. The maximum velocity comes from at the position where the two channels on the top and the two channels on the bottom cross each other, the horizontal red line of the circle shown in Figure 4-3. This is because the length of each channel segment is long enough that the difference between the pressure near the inlet and the outlet is clearly seen, as presented in Table 4-1 later. On the other hand, the convection induced by the U-shaped serpentine segment is not so large that the velocity in the quadrant region of each fractal channel is lower compared to that in the edge region. Diffusive transport rather than convective transport mainly occurs in this region because ΔP between each segment is low. As a result, the velocity in most of the areas of geometry is low compared to other geometries. The long straight serpentine shape could be

configured for the rectangular cell presented in the literature [111], however, the concept could not be fully realized for the circular shape presented in this research. Therefore, it is found that the fractal channel arrangement is not appropriate for circular CO_2RR reactor geometry in terms of the cell performance (high current density), although it shows good flow uniformity.

Geometry G_2 and G_3 is designed referring to the flow retrace concept presented in the literature [112]. This concept aims for achieving maximal ΔP between the channel by means of flowing the reactant to the position near the outlet and retracing back to the position near the inlet. In this way, the ΔP between the flow retracing back to the inlet (high P) and the flow directing to the outlet (low P) is maximized. The channels used for flow retrace are the two channels at the middle (brown and red) and the normal flow channels are at the outside (green and yellow) as shown in Figure 4-2 G_2 and G_3. The effect of flow retrace is identified by the contour shown in Figure 4-3 G_2 and G_3, where the velocity is maximized at the horizontal region of the GDL. At that position, the normal channels at the top and the retrace channels at the bottom cross each other so that the velocity is maximized with the increased ΔP between the channels. Geometry G_3 is distinctive from G_3 that the flow is split at the entrance to confirm the inlet flow uniformity as shown in Figure 4-2. The reactant is fed equally at the four inlets in design G_3, whereas flow is skewed to the center using one single inlet in design G_2. Uniform distribution at the inlet enhanced the convective mass transport at the upper region of the GDL as shown in Figure 4-3. G_3. It is also noted that geometry G_2 and G_3 shows better performance because of the densely configured flow channels compared to the sparsely patterned channels of geometry G_1. However, the velocity remains low at

the lower half of the GDL, because the pressure of the flow channel of that region is low. The concept of separate paths of the flow channel applied in geometry G_1, G_2, and G_3 is therefore not appropriate for maximizing the convective mass transport because of the lower pressure drop formed compared to the one-path flow configuration (geometry G_4 to G_8). It can be inferred from this result that the flow uniformity and the convection enhancement are in a trade-off relationship.

Geometries G_4 to G_7 in Figure 4-2 are intended to form one-path for the serpentine flow of the reactant gas. This concept is valid for maximizing pressure drop between the inlet and outlet of the flow channel. The velocity developed in the GDL is, therefore, higher and covers more area than the geometry of G_1 to G_3, as shown in Figure 4-3. The black arrows shown in Figure 4-4 denote the direction of the flow in the GDL, which is identified from the velocity vector analysis as shown in Figure 4-3. Flow segregation is discovered in geometry G_5 at the right side of the GDL, which reduced the convective mass transport in that area. This inefficiency is removed in geometry G_4, and additional improvement is attained by extra channel segmentation between the lower and upper part of the channel. But the upper right quadrant of the geometry G_4 shows poor performance because the outermost channel is not fully utilized. This is solved by extending the GDL in geometry G_6, but it also needs to be improved because the inefficiency is identified in the lower left quadrant. The flow in this region directs to the upward, whereas the flow in the other quadrants directs to the downward to the outlet, as shown in Figure 4-3 G_6. This phenomenon causes the inefficiency of convective mass transport in a way that the velocity vector vanishes when two reverse flows have encountered each other. This is resolved in geometry G_7, where all flow components consistently direct to

the downward outlet as shown in Figure 4-3.

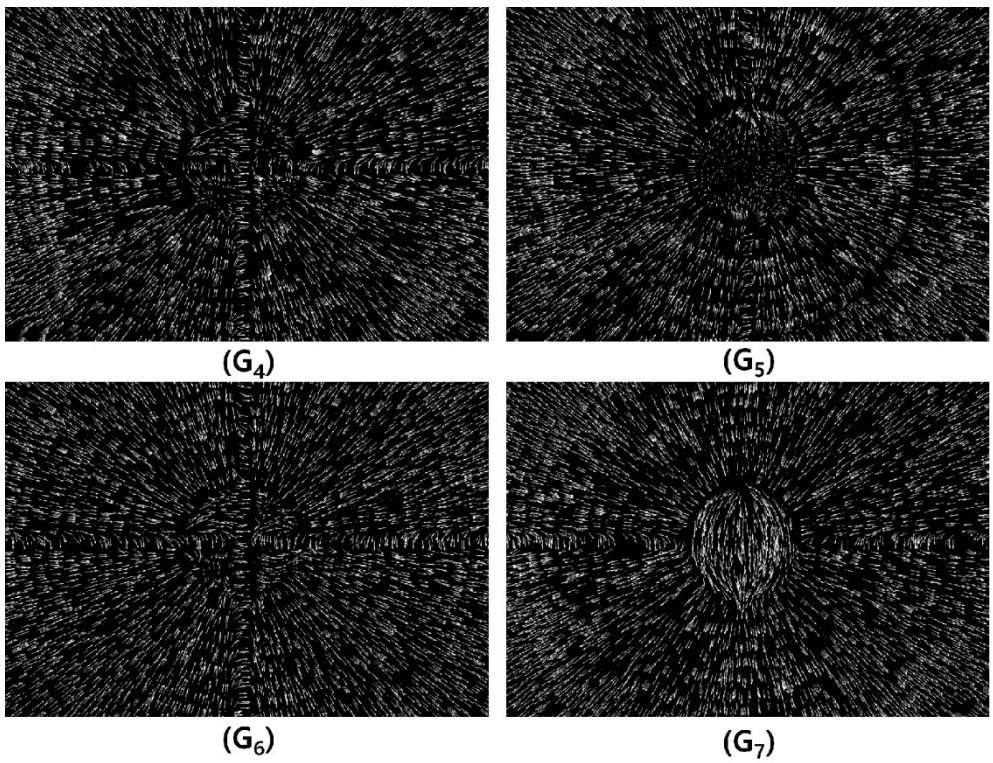

Figure 4-4. Velocity vector of the design geometry near the center of the GDL.

The final design G_8 reflects all the lessons learned from the case study of G_1 to G_7. It is one-path flow channel with increased pressure drop and patterned for inducing consistent flow direction from the inlet to the outlet. The convective flow is intensified by the channel segmentation as shown in Figure. 4-3 G_8. Surprisingly, the flow uniformity is also improved from the design G_7, implying that the flow segmentation concept can help both convection enhancement and catalyst utilization (by reducing local deactivation). Flow channel design therefore critically influences on cell performance. Fine-tuning of the channel geometry can dramatically improve the convective mass transfer, as well as overcome the trade-off relationship between convection enhancement and flow uniformity. The design G_8, however, still has

room for improvement. The convective mass transport is concentrated on the edge of the GDL and the velocity at the center remains low due to the low-pressure drop. The flow is also concentrated near the inlet and outlet, as well as the boundary between the segmented channel area. Too many segments will cause this local flow-concentration problem. High-pressure drop is also expected, which will cause a high energy consumption for pumping reactant gas and possibly local condensation of water in the flow channel. These effects are the main challenges encountered in CO_2RR design, which will further be investigated in future work.

4.1.7. Design criteria and case study selection

In the previous section, we briefly investigated a unidirectional uniform distribution flow pattern (UDF, G_8) in order to enhance mass transfer within an electrolyzer by CFD analysis. In this section, we discuss design criteria in more detail. In the UDF design, we considered an effective advection, a uni-direction gas flow, and a uniform distribution of the reactant through the pattern. The geometry of the reference cell consists of four flow segments, whereas the optimal cell geometry is intensified with eight segments, denoted as G_7 and G_8, respectively.

As shown in Figure 4-5(a), each channel is displayed in a different color, and the left and right sides of the channel are symmetrical. This design is a reconstructed version of the design idea proposed by Shresh et al. [111] assuming a similar inlet flow rate to each channel, the pressure difference between points A and B can be expressed using the Hagen-Poiseuille equation.

$$\Delta P_{AB} = P_A - P_B = \frac{128\mu(Q_{tot}/4)}{\pi D_{eff}^4}(\pi R_{cell}) = \frac{32\mu Q_{tot}}{D_{eff}^4} R_{cell} \qquad (4\text{-}6)$$

where μ is the dynamic viscosity ($Pa \cdot s$), Q_{tot} is the total volumetric flow rate of the feed gas (m^3/s), D_{eff} is the effective diameter of the flow channel (m), and R_{cell} is the radius of the cell (m). Eq. (4-6) represents the viscous loss of Newtonian laminar flow in the channel, producing a pressure difference between points A and B. As described by Darcy's law, this pressure difference is a driving force for the advection flow across the rib,

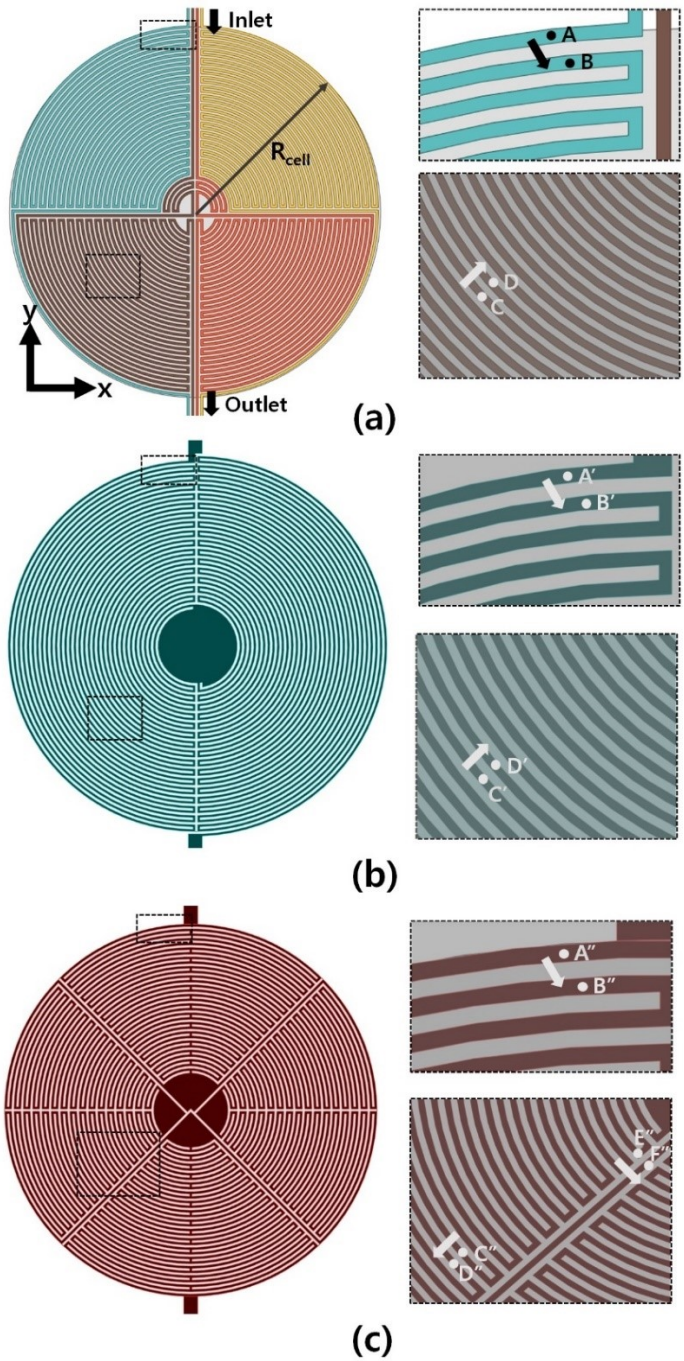

Figure 4-5. Design of flow channel of the electrochemical cell for CO_2RR: (a) separate paths, (b) single-path with flow retrace, and (c) unidirectional uniform distribution flow with segregation.

$$q = -\frac{K}{\mu}\nabla P \tag{4-7}$$

where q is the discharge per unit area (m/s), K is the permeability (m^2), μ is the dynamic viscosity ($Pa \cdot s$), and ∇P is the pressure gradient (Pa/m). Eq. (4-7) shows that the higher the pressure difference, the higher the convective flux in the porous GDE. Additionally, it can be inferred from Eq. (4-6) that the inefficiency of the design in Figure 4-5(a) arises because of the low volumetric flow rate ($= Q_{tot}/4$) and the short flow length (=πR_{cell}).

The design in Figure 4-5(b) improves the inefficiencies. This pattern is restructured according to the flow architecture proposed by Xu et al. [112]. Here, the gas first flows toward the outlet and then retraces back to the inlet. A longer trajectory increases the pressure difference, thereby enhancing convective mass transfer. A single-channel feed gas was used instead of separate channels; thus, the flow rate was not reduced by a factor of four. In addition, the length of the flow channel was doubled by the flow retrace configuration. The resulting $\Delta P_{A'B'}$ is eight times greater than that of ΔP_{AB}. Typical values of ΔP are summarized in Table 4-1. Accordingly, the convective flow and the electrochemical conversion of CO_2 could be significantly improved at the rib between A′ and B′. However, between C′ and D′, the flow retrace configuration in Figure 4-5(b) presents an inherent inefficiency. Notably, the flow between A′ and B′ is directed toward the outlet, that is, the -y direction, denoted as a vector in the figure. However, the flow between C′ and D′ is directed toward the inlet, that is, +y direction. These two opposing vectors vanish in the permeable GDE, thus causing a reduction in advection.

$$\left|\vec{(}A'B') + \vec{(}C'D')\right| = \sqrt{((x_{B'} - x_{A'}) + (x_{D'} - x_{C'}))^2 + ((y_{B'} - y_{A'}) + (y_{D'} - y_{C'}))^2} \quad (4\text{-}8)$$

Eq. (4-8) shows that the magnitude of the sum of the two vectors decreases owing to the cross-over of the gas in the y-direction, that is, $(y_{B'} - y_{A'})$ and $(y_{D'} - y_{C'})$ have the opposite signs. The flow will show nonuniformity when the components cancel out each other, and the overall conversion and catalyst activity will vary with location.

The flow structure in Figure 4-5(c) is devised to resolve this problem. This configuration has two distinctive characteristics: unidirectional flow and flow segregation. As shown in Figure 4-5(c), with this design, the flow could be directed in the -y direction everywhere in the cell. See the vectors between (A″ and B″), (C″ and D″), and (E″ and F″). The magnitude of the sum of the two vectors increases owing to the unidirectional flow of the gas in the y-direction, as indicated by the same signs as $(y_{B''} - y_{A''})$, $(y_{D''} - y_{C''})$, and $(y_{E''} - y_{F''})$ in Table 4-1.

Table 4-1. Analysis of pressure difference.

	Q	l_{ij}[a]	ΔP_{ij}[b]	$\vec{u}(2)/\lvert\vec{u}(2)\rvert$[c]
	sccm	mm	Pa	
AB	100	126	125	+1
CD	100	80	80	-1
$A'B'$	400	251	1004	+1
$C'D'$	400	160	640	-1
$A''B''$	200	63	125	-1
$C''D''$	200	40	80	-1
$E''F''$	200	616	1229	-1

[a] Channel length between points i and j.

[b] Pressure difference between points i and j.

[c] Sign of 2nd component of the vector $\vec{u}$.

As shown by the diagonal and horizontal lines in Figure 4-5(c), although the pressure difference between A″ and B″ is reduced because of the shorter flow length, it is compensated by the flow segregation. The pressure difference between E″ and F″, which is segregated by each compartment, is significantly larger than that between C″ and D″, which is located in adjacent flow channel. This is because the length of the channel is much longer, as summarized in Table 4-1.

It is expected that more segregation results in higher advection enhancement in the GDE. However, this leads to more deviation between each compartment as the pressure difference increases. In this study, considering such trade-off and

manufacturing difficulties, we proposed the flow configuration in Figure 4-5(c), as the final optimal design G_8. Notably, the geometry of the reference cell G_7 is the second-best in the case investigated, and it has fewer flow segments than G_8.

The high current density and FE of CO are pivotal design criteria based on the flow channel and GDE design. The flow channel and GDE affect the cell performance in such a way that the reactant gas is transported either through diffusion or through effective advection. Notably, the convection enhancement over diffusion increases the overall mass transfer rate [113], leading to a high current density. Possible design variables relevant to the mass transfer efficiency are the thickness of the channel and GDE, the porosity of the GDE, the total length of the channel, and flow channel configuration. The diffusion–advection equation at steady state in a porous media is described as

$$\varepsilon D \frac{d^2 c_i}{dz^2} - v \frac{dc_i}{dz} = r_i'' a = \frac{c_i}{1/k_c + 1/k_r} a \tag{4-9}$$

where ε is the porosity, D is the diffusion coefficient (cm^2/s), c_i is the concentration of species i (mol/cm^3) v is the superficial velocity (cm/s), r_i'' is the rate of reaction per unit surface area ($mol/cm^2 \cdot s$), a is the specific interfacial area of the bed (cm^2/cm^3), k_c is the mass transfer coefficient (cm/s), and k_r is the rate constant for the surface reaction (cm/s). The first and second terms on the left-hand side represent the diffusive and convective mass transfer, respectively. Rapid charge transfer reaction kinetics ($k_r \gg k_c$) reduce the right-hand side into $k_c c_i a$, thus presenting the system with a mass transport limitation. This is valid at a high current density, where the CO_2RR is affected by mass transfer limitation [78].

Therefore, the overall reaction rate of the system described in Eq. (4-9) is proportional to the mass transfer coefficient k_c, which is further empirically presented as follows:

$$\frac{1}{Sh_B} = \frac{1}{APe_B} + \frac{1}{B + C\left(\frac{\varepsilon}{aL}Pe_B\right)^D} \tag{4-10}$$

where $Sh_B = \varepsilon k_c/aD$ and $Pe_B = v/aD$ are the Sherwood and Peclet numbers, respectively. A, B, C, and D are empirical constants, and the typical values of these parameters in the low Reynolds regime ($Re \approx 1$) are 1.20, 0.914, 1.017, and 1/3, respectively [114]. Eqs. (4-9) and (4-10) indicate the importance of the convective mass transfer rate in achieving high cell efficiency. The overall mass transfer rate (Sh_B) will increase if convection is enhanced in the GDE, that is, at a high Peclet number. Therefore, maximizing the convective mass transfer rate is crucial, and it is the main criterion for the flow channel design in this research. In addition, the flow uniformity is monitored as a secondary criterion for evaluating the cell performances. This is because it is related to the total current of the cell and local catalyst deactivation, which is crucial for the long-term operation of the commercial CO_2RR reactor. Based on the CFD model, these two criteria are numerically expressed with the area-weighted average of the velocity (u_{avg}) for convection and the ratio of the maximal velocity to the area-weighted average of the velocity for the flow uniformity ($F_u = u_{max}/u_{avg}$), respectively. In addition, the standard deviation of the normalized velocity ($\sigma_{\bar{\bar{u}}} = \sqrt{\sum_{i=1}^{n} (\bar{\bar{u}} - \mu_{\bar{\bar{u}}})^2/n}$) is compared to remove the scale effect on the uniformity. The u_{avg} and u_{max} are calculated from the middle surface between the top and bottom of the GDE (S_{mon}). To evaluate the standard

deviation, the velocity values u_i are sampled from the predefined point cloud with equally spaced rectangular grids (n = 1005), as shown in Figure 4-3.

Therefore, two important design criteria were proposed for cell design: convection enhancement and flow direction uniformity. A CFD model describing mass transfer in a membrane cell reactor was developed for the quantitative analysis of different flow patterns.

4.1.8. Scale-up effect on u_{avg}

The scale effect on u_{avg} is numerically investigated by varying the cell size (5 cm^2, 10 cm^2, and 50 cm^2) of the geometry G_7 and G_8. Detailed geometry is shown in Figure 4-6, and the results are presented in Figure 4-7. As can be seen from the figure, the average velocity in S_{mon} increases with the cell size due to the large pressure drop induced by the long flow channels. It is noted that G_8 always shows better performance than G_7, revealing that the optimal geometry can apply to the wide operating window. The ratio of increment also increases with the cell size, indicating that the mass transfer limitation has a severe effect on the CO_2RR performance at a large production rate. This result reveals the importance of the flow channel design, especially for the large-scale process.

As shown in Figure 4-8, the scale effect on the cell performance with respect to standard deviation of normalized velocity ($\sigma_{\overline{\overline{u}}}$) was also investigated. The flow uniformity decreases with increasing cell size, as indicated by the increase in $\sigma_{\overline{\overline{u}}}$. This implies that the mass transfer effect is more crucial at a higher production scale, and the flow pattern design is crucial in removing the barrier. Additionally, maintaining flow uniformity is important in terms of catalyst utilization and long-term stability. Similarly, the optimal design G_8 exhibits better flow uniformity compared to the G_7 at all production scales, revealing that the flow structure is applicable to a wide operational window. The gap between the two designs decreases as the cell area increases. This indicates that a new optimal design with production rates higher than a flow rate of 400 sccm is required in this study.

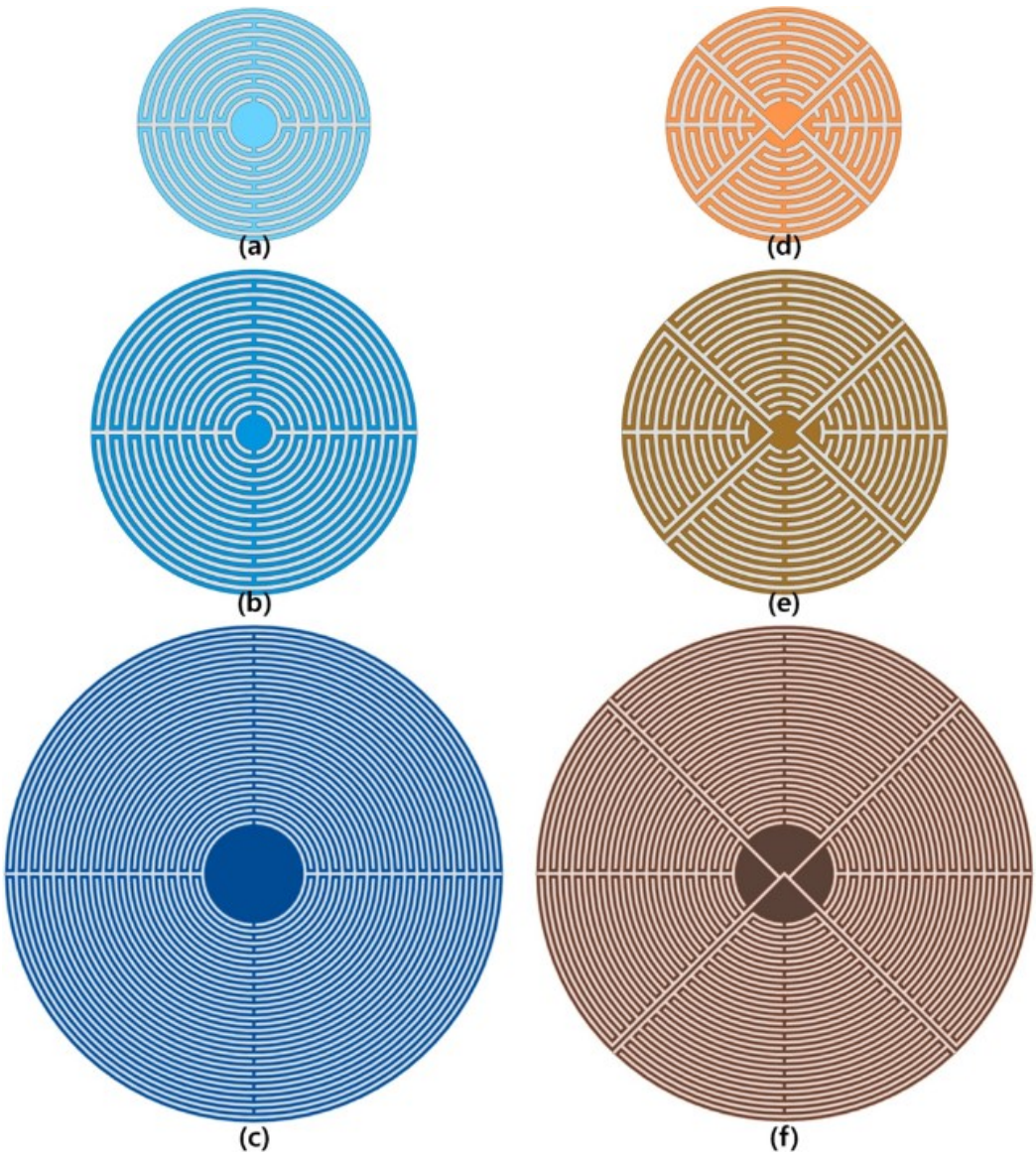

Figure 4-6. Cell geometries with different sizes (a) $G_7, 5cm^2$, (b) $G_7, 10cm^2$, (c) $G_7, 50cm^2$, (d) $G_8, 5cm^2$, (e) $G_8, 10cm^2$, and (f) $G_8, 50cm^2$.

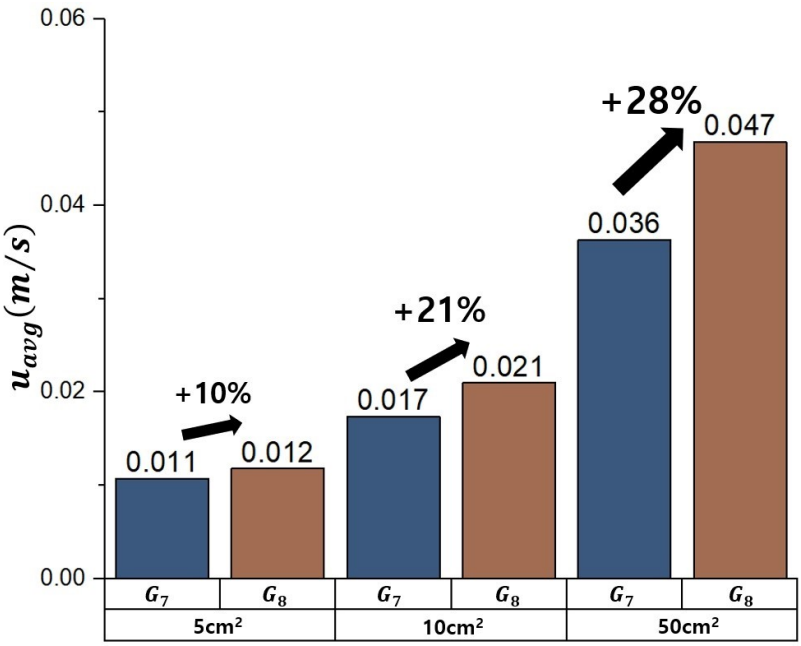

Figure 4-7. Scale effect on u_{avg}.

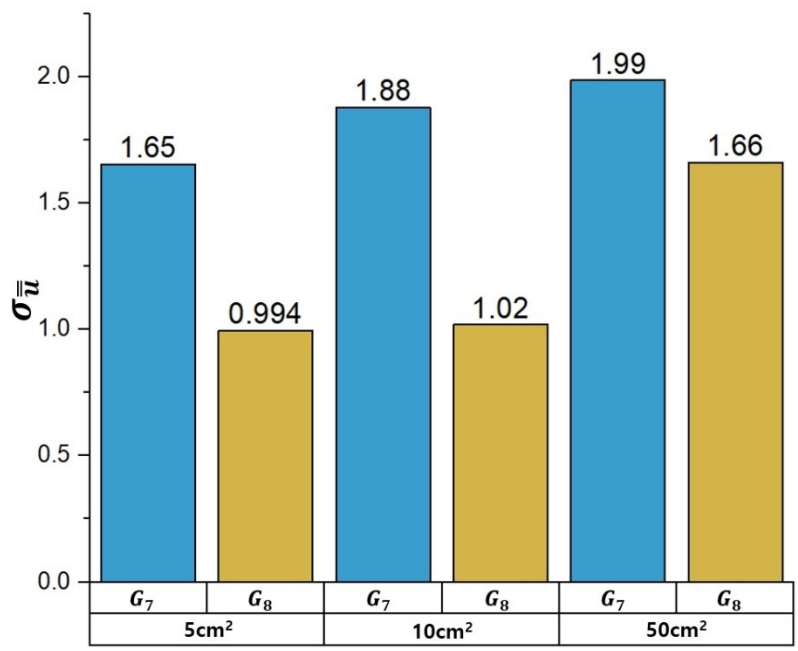

Figure 4-8. Scale effect on the flow uniformity according to standard deviation of normalized velocity ($\sigma_{\bar{u}}$).

4.1.9. Summary of CFD simulation

The results of the CFD simulation of all the cases are summarized in Table 4-2.

Table 4-2. Summary of CFD simulation results.

Geometry	Channel length[a]	ΔP_{in-out}[b]	u_{avg}[c]	u_{max}	$\frac{u_{max}}{u_{avg}}$	$\sigma_{\overline{\overline{u}}}$[d]	Pe
	mm	Pa	m/s	m/s			
G_1	4983	1391	0.0108	0.2918	27	1.4262	0.7221
G_2	5182	1511	0.0159	0.4305	27	1.7464	1.0590
G_3	5182	1682	0.0184	0.5417	30	1.5300	1.2240
G_4	5489	9290	0.0306	2.2883	75	2.0424	2.0376
G_5	5275	12320	0.0312	3.4197	109	1.8400	2.0827
G_6	5489	5973	0.0338	1.6818	50	2.5017	2.2531
G_7	5399	3781	0.0363	1.4518	40	1.9853	2.4215
G_8	5370	6052	0.0468	1.3695	29	1.6602	3.1193

[a]Total channel length between inlet and outlet.

[b]Total pressure drop from inlet to outlet.

[c]Area average velocity calculated from the surface of the monitoring S_{mon}.

[d]Standard deviation of normalized velocity values taken from the point clouds.

The velocity contours of the geometries obtained from S_{mon} are shown in Figure 4-3. The figure shows that the velocity in the GDE increases with the improvement of the flow path. As summarized in Table 4-2. geometry G_3 exhibits poor performance in terms of convection owing to the low-pressure difference (ΔP) along

the split channel. Notably, the velocity is maximized in the horizontal region of the GDE, where the channel compartments cross each other, indicating that the convective mass transfer is enhanced by the pressure difference across the rib of the serpentine channel. Despite the low Peclet number, G_3 has good flow uniformity owing to its separate channels.

Geometry G_5 forms a path for the serpentine flow of the reactant gas. This concept is valid for maximizing ΔP_{in-out} between the inlet and outlet of the flow channel. Therefore, as shown in Figure 4-3, the velocity formed in the GDE of G_4 is higher and covers more area than that in the G_3. However, maximal ΔP_{in-out} may require additional compression power to supply the feed gas, and it results in a high operational cost for a scaled-up process. Additionally, the flow segregation is established at the right side of the GDE owing to the effect of the low pressure at the center and serpentine flow configuration. The flow segregation reduces the convective mass transport and maximizes the flow deviation within the region. Although G_5 shows a higher convective flow than G_3, it is characterized by high ΔP and poor uniformity.

As presented in Figure 4-3, the presented optimal flow pattern, G_8, exhibits the best performance in convection. The inefficiency established in G_3 and G_5 is removed through unidirectional flow with a segregation concept. This is a one-path flow channel that is patterned to increase ΔP and guide a consistent flow direction from the inlet to the outlet. As shown in Figure 4-3 G_8, all flow components are consistently directed to the downward outlet. Convection is improved by channel segmentation, as shown by the red diagonal and horizontal contours. Moreover, as denoted in Table 4-2 the flow uniformity is improved with this geometry, which

implies that flow segmentation can enhance convection and utilize the catalyst by reducing local deactivation. Therefore, the flow channel design affects the cell performance significantly. Fine-tuning of the channel geometry can significantly improve the convective mass transfer (up to 430% in this study), as well as overcome the trade-off relationship between convection enhancement and flow uniformity. However, the design G_8 could be improved more. The convective mass transport is concentrated at the edge of the GDE, and the velocity at the center remains low owing to the low-pressure difference. In addition, the flow is concentrated near the inlet and outlet, as well as the boundary between the segmented channel areas. Too many segments will cause this local flow-concentration problem. These effects are the main challenges encountered in the design of CO_2RR, which will be investigated further in future work.

4.2. Experimental investigation

4.2.1. Experiments setup

Both electrodes were made on carbon diffusion layers (Sigracet 39BB). Ag nanopowder (Alfa Aesar) and IrO_2 nanopowder (Alfa Aesar) were used to make ink with 5 wt% Nafion (NR 50, Aldrich) based on the metal content respectively, and isopropanol. Each ink was agitated by ultrasonication for 20 min then was sprayed on GDL upon preheated hot plate at 70ºC. The amount of loading of each electrode was 1 mg/cm^2 with respect to the inorganic catalyst weight and the area of the electrode was 50 cm^2. Instead of using an anion exchange membrane (AEM), a porous filter membrane (Durapore, 0.45 μm pore size, hydrophilic PVDF) was used for zero-gap CO_2RR configuration between anode and cathode. It enables to prohibit electronic contact and have ionic conductivity like AEM. In addition, gas diffusion layers were filled in between each electrode and the current collector. Figure 4-9 and Figure 4-10 describe the electrocatalytic CO_2 reduction system designed for this study.

Figure 4-9. Picture of actual CO_2RR experimental device.

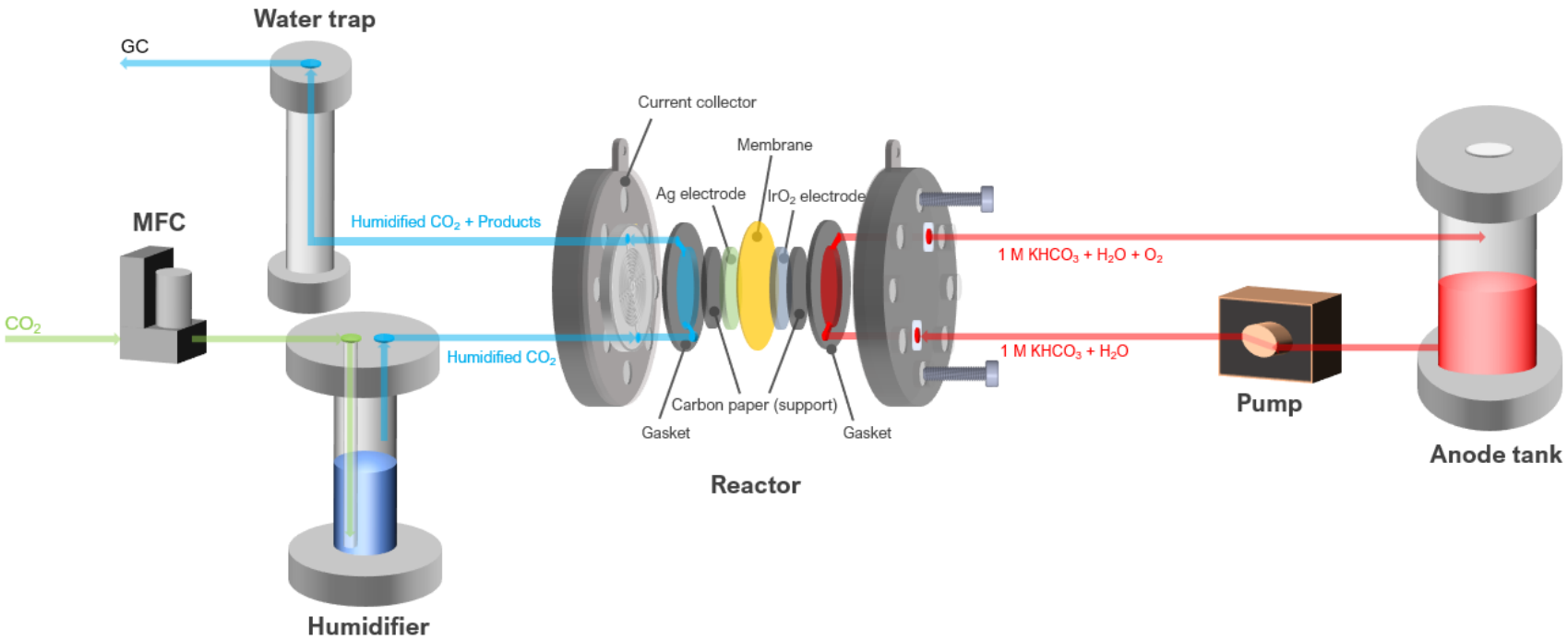

Figure 4-10. Process flow diagram of the electrochemical CO_2 reduction experiment in a large-scale electrolyzer (50 cm^2).

4.2.2. Flow pattern investigation

Before examining the extrinsic properties of CO_2RR in detail, we investigated each flow pattern G_7 (Reference design) and G_8 (UDF design). The water-saturated CO_2 gas was supplied to a 50 cm^2 electrolyzer operating at room temperature (25ºC). Thereafter, the CO_2 gas was transported to a current collector of the cathode section, which had a serpentine channel. The composition of the gas product was analyzed via gas chromatography (GC) (Agilent 7890 A) and partial current (j_i) and FE was calculated by Eq. (4-11)

$$j_i = x_i \cdot Q_{tot} \cdot \frac{n_i F P_O}{RT} \cdot (Electrode\ area)^{-1} \quad (4\text{-}11)$$

where x_i is the volume fraction of a certain product determined by GC that was calibrated using a diluted mixture of gases for calibration curves from the standard gas sample, Q_{tot} is the flow rate of CO_2, n_i is the number of electrons involved, P_O is atmospheric pressure, F is the Faradaic constant, T is the room temperature, and R is the universal gas constant. Also, FE was given through the observed current of a certain component divided by the total current. Figure 4-11 shows the chronopotentiometry results of two flow patterns. Current increased from 1000 mA to 3500 mA by 500 mA. The operating condition was 400 sccm of CO_2 flow rate, all experiments in this chapter were performed under the condition of 1 M of $KHCO_3$ electrolyte, and 1 mg/cm^2 of Ag and IrO_2 catalyst loading. Both designs received maximum FE at near 3 V. Figure 4-12 shows Linear sweep voltammetry (LSV) results with a range from cell voltage 0 to 3 V at v = 50 mVs^{-1} that UDF design obtained better performance compared to the reference design.

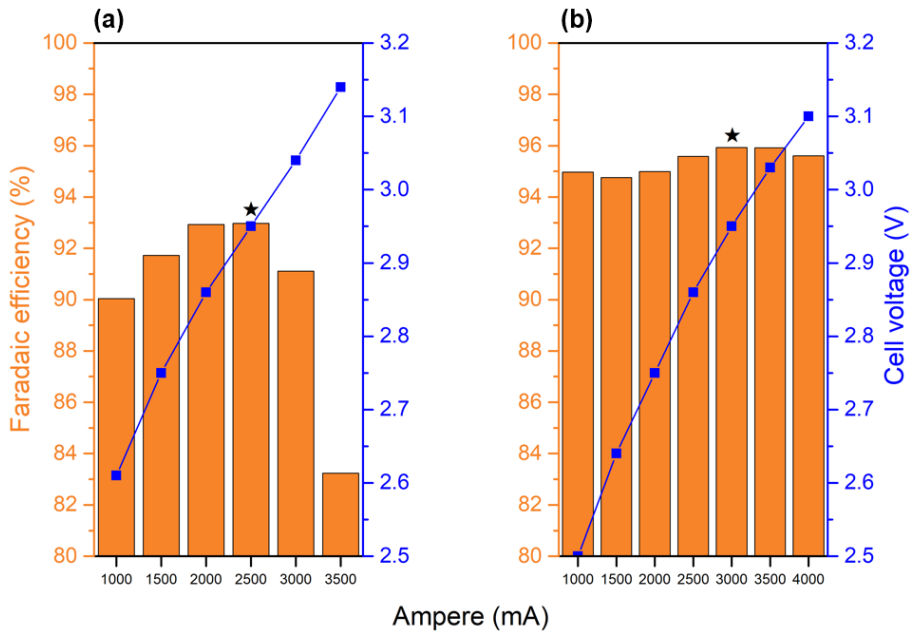

Figure 4-11. Chronopotentiometry results (a) reference design (b) UDF design.

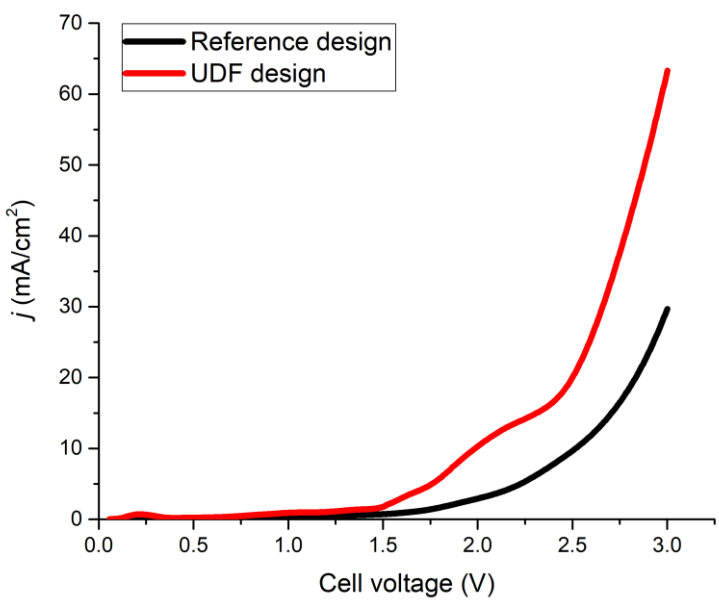

Figure 4-12. LSV results for reference design and UDF design with range from cell voltage 0 V to 3 V at v = 50 mVs^{-1}.

Figure 4-13 shows partial current density of reference design and UDF design with respect to flow rate variations. UDF design attained better partial current of CO over all ranges of CO_2 flow rate.

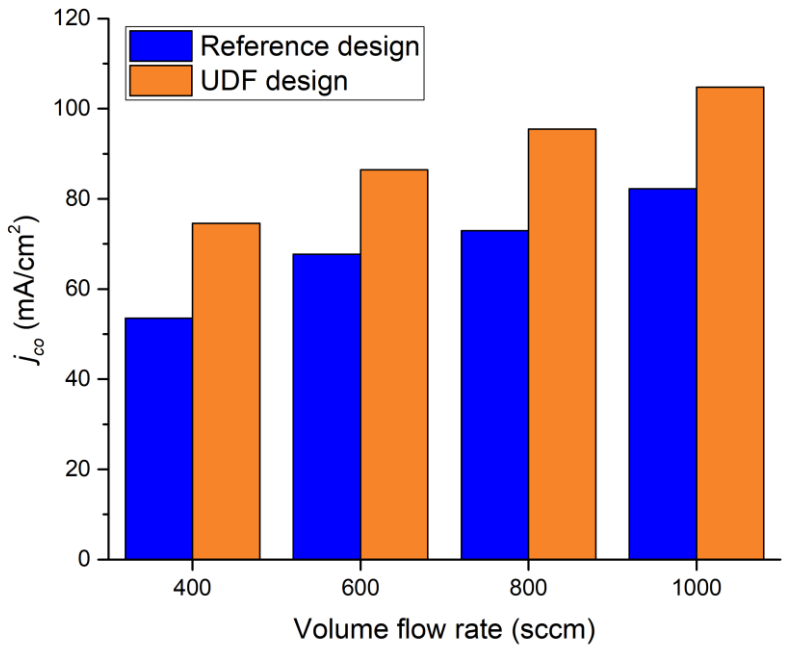

Figure 4-13. Partial current density of reference design and UDF design with respect to flow rate variations.

4.2.3. Investigation of extrinsic properties

In this study, we focus on the electrochemical reduction of CO_2 to CO. The electrochemical conversion of CO_2 on Ag catalyst is well known for its high FE of CO production compared to other competitive reactions [115]. Thus, the production rate changes are easily tractable compared to other CO_2RR reactions. Notably, the CO partial current density can further be improved by manipulating both intrinsic and extrinsic properties. However, this study mainly investigates extrinsic property effects rather than intrinsic properties. To evaluate the extrinsic properties of the CO production rate, we carried out case studies with varying electrolytes, catalyst/electrolyte interfaces, and serpentine flow patterns. Notably, we used the same Ag nanoparticle to fabricate the cathode catalyst; thus, we assume that the intrinsic kinetic properties of the electrocatalyst are not changed. The reference case employs a cell voltage of 3 V, 400 sccm of gaseous CO_2 flow rate, 1 M of $KHCO_3$ electrolyte, 1 mg/cm^2 of Ag catalyst loading, and the flow pattern G_7 introduced by Endrodi et al. [116]. The reference operating condition is a cell voltage of 3 V, 400 sccm of CO_2 flow rate, 1 M of $KHCO_3$ electrolyte, and 1 mg/cm^2 of Ag catalyst loading. The reference flow patterns (G_7) are in red bars and the UDF designs (G_8) are in blue bars.

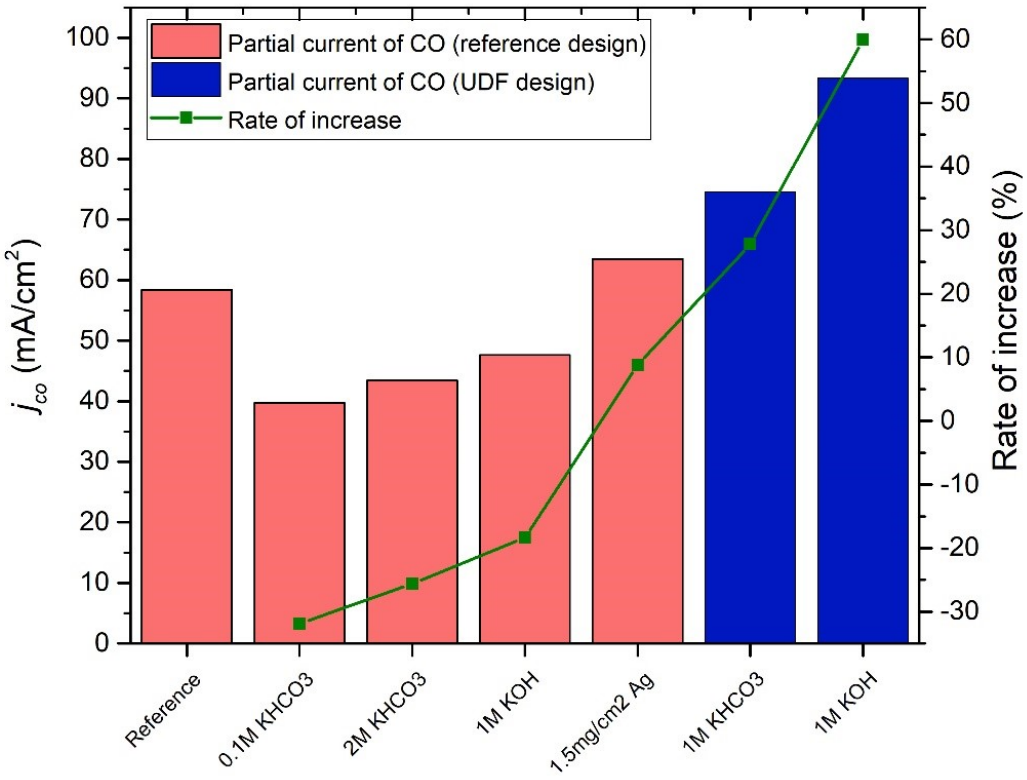

Figure 4-14. Experimental results of pH, interface, and flow pattern effect to mass transfer on CO_2RR.

Figure 4-14 summarizes the result of experimental studies. The UDF design exhibits a significant improvement in the partial current density of CO. As shown in Figure 4-14, the UDF design alone increased the CO partial current density by approximately 28%. Note that the UDF design can be operated in stronger basic electrolyte without salt formation, thus the more basic electrolyte exhibits the higher CO partial current density. This is because of the high average flow velocity and uniform flow distribution eliminating the dead zone within the electrolyzer. The experimental results and theoretical analysis should support the need for a 3D modeling approach when designing a large-scale electrolyzer. The pressure difference across the rib, flow segmentation, and flow direction established in the channel architecture play a significant role in advection, and in turn, the overall cell performance.

When Ag black was used as the cathode electrode in the experiments, only CO and H_2 were observed for the reduction product, which shows good agreement with previous studies [117]. In the reference case flow pattern, higher catalyst loading results in a higher CO production rate, whereas the change in electrolyte concentration exhibits an optimum at 1 M $KHCO_3$. The interface effect among the CO_2, electrolyte, and electrocatalyst was investigated by modifying the Ag catalyst loading on the GDE. The active site area for the reaction can be extended as the amount of catalyst loading increases. However, increasing the cathode catalyst loading results in a thicker electrocatalyst layer that may decrease its porosity [118]. In this experiment, 1.5 mg/cm^2 of Ag was sprayed on the diffusion layer, and it exhibited a higher CO reaction rate. However, experimental results indicated a limited amount of increment (< 8.8%) in CO production rate even

with a higher amount of catalyst loading. The pH effect was investigated by measuring the current density of CO using 0.1 M, 1 M, 2 M $KHCO_3$, and 1 M KOH. Note the CO_2 saturated 0.1 M and 1 M $KHCO_3$ solutions have pH of 7 and 7.8, respectively. As the $KHCO_3$ electrolyte concentration increased from 0.1 M to 1 M, the acid-base equilibria were shifted according to the proton concentration, and consequently, the concentration of the CO_2 and proton donor at the catalytic surface was changed. When KOH is used instead of $KHCO_3$, the porous separator causes a high pH on the electrode surface due to the constant supply of KOH, despite neutralization by dissolved CO_2. The higher basicity of the solution decreases the concentration of the proton donor, HCO^-, and the hydrogen evolution reaction (HER) can be suppressed. However, owing to the slow reaction rate of CO hydration, the concentration of the proton donor has a slight effect on the reactive CO_2 [79]. Ma et al. demonstrated that the pH increase in the electrode surface increased the partial current density significantly [119]. However, the CO_2 can be converted into electrochemically inactive carbonate in a strongly basic environment. Therefore, it is crucial to maintain the optimum pH in the catalyst layer to suppress the HER without affecting the CO_2RR. However, a high-concentration electrolyte often forms a bicarbonate salt and lowers partial current of CO_2RR. A recent study [120] has suggested a self-cleaning strategy to prevent salt precipitation using a pulsed applied voltage, which provides better stability than the conventional cell-rinsing methods [121].

4.2.4. Experimental verification

Finally, we experimentally performed a sensitivity analysis of the CO_2 inlet flow rate. As we previously highlighted, the convective mass transfer can be expressed using the area-weighted average of velocity u_{avg}, and u_{avg} increases as the inlet flow rate increases. Thus, we increased the feed flow rate from 400 to 1000 sccm by 200 sccm and measured the changes in partial current density. The partial current density of CO increased if the convective mass transfer rate has a significant contribution to the overall reaction rate, and the improvement in current density can be expressed in terms of the Peclet number. Figure 4-15 shows the result of the experiments, and current densities are normalized with the data of G_7 at 400 sccm and the overall convective transfer rates are fitted to Eq. (4-10). A higher current density was observed with a higher flow rate, indicating that the reactor was operated under a mass-transport limited regime. The slope of the graph gradually decreases as the flow rate increases, indicating that the convective mass transfer is less significant when the inlet flow rate is sufficiently high. Notably, the performance of the optimal reactor is better than that of the conventional design over the entire operating window. This is because the optimal design has a higher velocity in the GDE. Therefore, the mass transfer is enhanced by convection, leading to a higher CO_2 reduction.

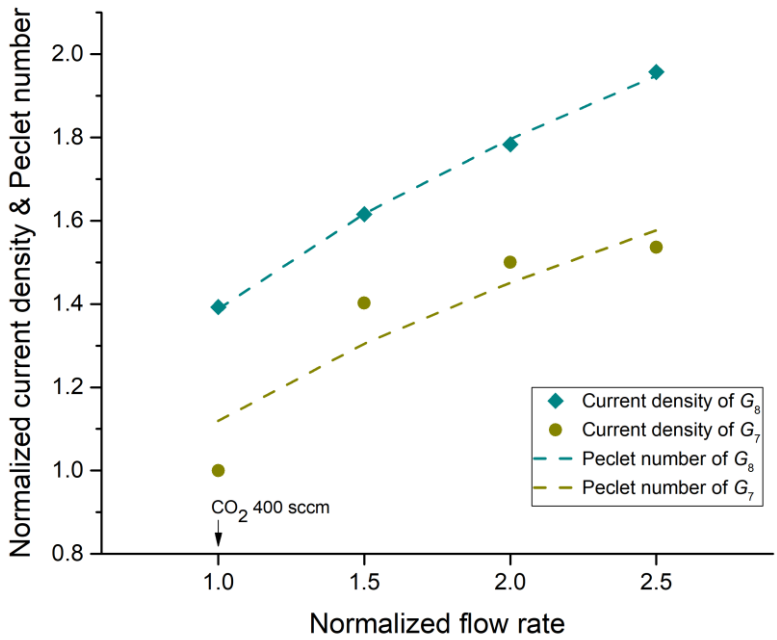

Figure 4-15. Experimental current density data (points) regressed with CFD simulation (dotted lines) under different flow rates.

In addition, as shown in Table 4-2, the data of the normalized current density are empirically interpolated with the normalized Peclet number based on the (u_{avg}) computed from CFD simulations. A nonlinear relationship between the rate of overall mass transfer (Sherwood number) and velocity (Peclet number) is described by Eq. (4-10). The right-hand side of the equation is dominated by the second term at the higher velocity. As a result, the Sherwood number is dependent on the Peclet number in this flow regime. Both the optimal and conventional designs of exponent D were 0.3728. The empirical value for exponent D in the general case is 1/3 [114], indicating that the values obtained in this study are consistent with the reference values. The slope of the Peclet number of G_8 reveals that it performs better at a

higher flow rate, and it is more suitable for the scale-up of the reactor compared to that of G_7. The higher value for the optimal design implies that the convective mass transfer is enhanced by the flow segmentation, and the larger area is affected by the convection enhancement at the high flow rate compared to the conventional design.

4.3. Conclusion

In this study, we investigated the effect of the extrinsic properties on the performance of a large-scale CO_2RR electrolytic cell. The proposed UDF design can enhance mass transfer through high convection and unidirectional flow pattern. In the large-scale cell design, the flow channel configuration is one of the critical factors for facilitating mass transfer which not only increases the production rate but also improves stability by avoiding salt formation. The results of the CFD simulation indicate that the CO partial current density increments are consistent with the convectional mass transfer increase, indicating that a high-performance design can be achieved through flow pattern optimization. This study contributes to general guidelines for scalable cell design by deriving design philosophies (i.e., Uni-direction and high average flow velocity) related to advection enhancement and flow uniformity.

Chapter 5. Concluding remarks

5.1. Summary of contributions

The main objective of this dissertation was to develop proper numerical simulation models for predicting the transport phenomena that occur in the energy supply chain of low carbon energy with actual measured data. And a design methodology for its system was suggested through the developed model. The contributions drawn from each chapter are as follows.

Chapter 2. LNG Storage

- A 1D prediction model of LNG weathering was developed from a long-term (50 days) experiment in a large-scale tank (50 m^3) containing nitrogen and hydrocarbons, under isobaric operation.
- Using measurable variables, this study implemented net evaporation equations of pressure base linearized SRT and empirical vapor-liquid equilibrium constant from the LNG terminal and net heat transfer equations integrated with heat exchange of BOG and NG at the interface, which reflect the actual phenomena; relatively constant liquid temperature in the height direction and thermal stratification of the vapor phase.
- Through the developed model, we found deviations of the conventional approach from the measured data and proposed a design methodology to apply this model to different tanks using the BOG generation parameter (c) and equilibrium constant (K_{N_2}) proposed by GIIGNL.

Chapter 3. Hydrogen distribution

- An 0D dynamic simulation model covering the whole sequence of the HRS was developed and validated by actual data of HRS located in South Korea.
- This study investigated the complicated interdependency of the design variables of main HRS components by the developed model. One is a compressor and 5 design variables of buffer storage systems: the number of stages, initial pressure of each tank, volume of each tank, switching pressure to the next pressure level tank, and operating pressure range of each tank.
- This study proposed a design methodology and suggested how to size a compressor considering both HRS and vehicle specification, peak demand, and available pressure of hydrogen sources, and how to control the compressor during refueling to reduce a buffer storage volume.
- It also suggested an improved design that has 4 stages buffer storage system with well-distributed initial pressure, proper volume sizing of lower pressure for back-to-back fillings, 300 bar operating pressure range of each tank, and 50 bar switching pressure to the next pressure level tank.

Chapter 4. CO_2 Conversion

- A three-dimensional computational fluid dynamic model was developed to quantify the effect of the flow pattern on mass transfer that has a great influence on the reaction performance at the three-phase interface.
- An optimal flow pattern design by CFD was investigated by measuring the production rate of CO experimentally, and it shows the optimal flow pattern enables boosting CO production.

- As a design methodology, this study proposed two important design criteria, enhanced convection with the uni-directional flow and uniform flow distribution, by designing the geometry of the flow pattern that influences flow direction and pressure drop.

5.2. Limitations and future works

The limitations of the research are summarized as follows.

Chapter 2. LNG Storage

- Although the developed model can be applied to other scenarios (different LNG compositions, a wide range of liquid fractions, and various types and geometry of storage tanks) using the BOG generation parameter (c) and equilibrium constant (K_{N_2}), further studies with experimental validation are required for the versatility and robustness of the developed model.
- This study was conducted under isobaric conditions as the basic. However, pressure in the storage increases in a scenario such as bunkering and self-pressurization, so further research on the effect of pressure is required.

Chapter 3. Hydrogen distribution

- This study presented a design methodology for saving CAPEX and OPEX. Actual optimization results can be obtained by developing a cost model that can accurately estimate the cost of equipment and energy consumption.
- In this study, only one vehicle refueling per one HRS was targeted, but research on simultaneous refueling with multiple dispensers is needed.

Chapter 4. CO_2 Conversion

- CFD simulations show that ΔP_{in-out} of G_8 is 0.0039 bar for 5 cm^2 and 0.06 bar for 50 cm^2. As the reactor area increases 10 times, the pressure drop

increases more than 10 times. Therefore, it is possible to change the design under an acceptable level of pressure drop later when the commercial size of the reactor and an available pressure drop is given.

- In this study, only the influence on mass transfer was investigated using CFD, but a model can be developed for solving multi-physics problems containing reaction and electron transfer.

Nomenclature

Acronyms & Abbreviations

AEM	anion exchange membrane
APE	absolute percentage error
APRR	average pressure ramp-up rate
BOG	boil-off gas
BOR	boil-off rate
CAPEX	capital expenditure
CFD	computational fluid dynamics
CO_2RR	carbon dioxide reduction reaction
COP	coefficient of performance
CV	valve flow coefficient
D	dimension
EOS	equation of state
EV	electric vehicle
FCEV	fuel cell electric vehicle
FE	Faradaic efficiency
GC	gas chromatography
GDE	gas diffusion electrode
GDL	gas diffusion layer
GIIGNL	International Group of Liquefied Natural Gas Importers
HP	high pressure
HRS	hydrogen refueling station
LNG	liquefied natural gas
LSV	Linear sweep voltammetry
MAPE	mean absolute percentage error
MBWR	modified Benedict-Webb-Rubin equation of state
MP	medium pressure
NG	natural gas
NIST	National Institute of Standards and Technology
OPEX	operational expenditure
SAE	the Society of Automotive Engineers
sccm	standard cubic centimeter per minute

SIMPLE	semi-implicit method for pressure linked equations
SRT	statistical rate theory
TPB	triple-phase boundary
TRL	Technology Readiness Level
UDF	uni-directional flow

Chapter 2

a	Helmholtz free energy
A	wetted surface area
c	BOR fitting parameter
d	thickness
h	heat transfer coefficient
H	extensive enthalpy
k	thermal conductivity
L	reference length
$Lev.$	level
M	mass
MW	molecular weight
$\dot{M}_{BOG}$	evaporation rate
Nu	Nusselt number
P_{Sat}	bubble point pressure
$\dot{Q}$	heat flow
R	universal gas constant
Ra	Rayleigh number
$S_{Interface}$	free surface area
U	overall heat transfer coefficient
Wo	outer wall
Wi	inner wall
t	time
y, x	mol fraction of vapor, liquid
$\hat{y}, \hat{x}$	mass fraction of vapor, liquid
ρ	density
ϵ	surface of emissivity
σ	Stefan-Boltzmann constant

Chapter 3

a	valve losses
C	clearance
E_v	volumetric efficiency
h	specific enthalpy
i	i th stage
k	specific heat ratio (C_p/C_v)
$\dot{m}$	mass flow
n	rotating speed
N	total number of stages
p	Precooler
P	pressure
$\dot{Q}$	heat flow
R	compression ratio
w	cooling water
$\dot{W}$	work
V	volume
z	compressibility
η_{is}	isentropic efficiency
ρ	density

Chapter 4

a	the specific interfacial area of the bed
c_i	concentration of species i
C_2	inertial loss coefficient per unit length
D	diffusion coefficient
D_{eff}	effective diameter of the flow channel
E	total energy
F	Faradaic constant
$\vec{F}$	external body forces
$\vec{g}$	gravity vector
h_i	sensible enthalpy of species i
j_i	partial current
$\vec{J}_i$	the diffusion flux of species i
k_c	mass transfer coefficient

k_r	rate constant for the surface reaction
k_{eff}	effective conductivity
K	permeability
l_{ij}	channel length between points i and j.
M	mole
n_i	the number of electrons involved
p	static pressure
P_O	atmospheric pressure
∇P	pressure gradient
ΔP	pressure difference
Pe	Peclet number
q	discharge per unit area
Q_{tot}	total volumetric flow rate of the feed gas
r_i''	rate of reaction per unit surface area
R	universal gas constant
R_{cell}	radius of the cell
Sh	Sherwood number
S_{mon}	area-weighted average of the velocity at the middle surface of the GDL
T	room temperature
u_{avg}	area-weighted average of the velocity
v	superficial velocity
$\vec{v}$	velocity vector
V	voltage
x_i	volume fraction of a certain product i
Y_i	local mass fraction of species i
α	permeability
$\sigma_{\overline{\overline{u}}}$	standard deviation of the normalized velocity
ρ	fluid density
μ	dynamic viscosity
ε	porosity
$\bar{\bar{\tau}}$	stress tensor

References

1. Giannikopoulos, I., et al., *Probing the Impact of an Energy and Transportation Paradigm Shift on the Petrochemicals Industry.* Industrial & Engineering Chemistry Research, 2022.
2. Ummalla, M. and A. Samal, *The impact of natural gas and renewable energy consumption on CO2 emissions and economic growth in two major emerging market economies.* Environmental Science and Pollution Research, 2019. **26**(20): p. 20893-20907.
3. Zhang, X., et al., *Climate benefits of natural gas as a bridge fuel and potential delay of near-zero energy systems.* Applied Energy, 2016. **167**: p. 317-322.
4. Al-Kuwari, O. and M. Schönfisch, *The emerging hydrogen economy and its impact on LNG.* International Journal of Hydrogen Energy, 2022. **47**(4): p. 2080-2092.
5. Chi, J. and H. Yu, *Water electrolysis based on renewable energy for hydrogen production.* Chinese Journal of Catalysis, 2018. **39**(3): p. 390-394.
6. Nikolaidis, P. and A. Poullikkas, *A comparative overview of hydrogen production processes.* Renewable and Sustainable Energy Reviews, 2017. **67**: p. 597-611.
7. Meinshausen, M., et al., *Greenhouse-gas emission targets for limiting global warming to 2 C.* Nature, 2009. **458**(7242): p. 1158-1162.
8. Ritchie, H., M. Roser, and P. Rosado, *CO_2 and greenhouse gas emissions.* Our world in data, 2020.
9. Thomas, H., *Options for producing low-carbon hydrogen at scale.* 2018.
10. Antonini, C., et al., *Hydrogen production from natural gas and biomethane with carbon capture and storage – A techno-environmental analysis.* Sustainable Energy & Fuels, 2020. **4**(6): p. 2967-2986.
11. Kearns, D., H. Liu, and C. Consoli, *Technology readiness and costs of CCS.* Global CCS institute, 2021.
12. Becker, R., *MARPOL 73/78: An overview of international environmental enforcement.* Georgetown International Environmental Law Review, 1997. **10**(2): p. 625-642.
13. Rogers, H.V., *Asian LNG demand: Key drivers and outlook.* 2016.
14. Hwang, C. and Y. Lim, *Optimal process design of onboard BOG*

re-liquefaction system for LNG carrier. Journal of Ocean Engineering and Technology, 2018. **32**(5): p. 372--379.
15. Kim, J.-W., J.-y. Jeong, and D.-J. Chang, *Optimal Shape and Boil-Off Gas Generation of Fuel Tank for LNG Fueled Tugboat.* Journal of Ocean Engineering and Technology, 2020. **34**(1): p. 19--25.
16. Pellegrini, L.A., et al., *LNG technology: the weathering in above-ground storage tanks.* Industrial \& Engineering Chemistry Research, 2014. **53**(10): p. 3931--3937.
17. Huerta, F. and V. Vesovic, *A realistic vapour phase heat transfer model for the weathering of LNG stored in large tanks.* Energy, 2019. **174**: p. 280--291.
18. Miana, M., R. del Hoyo, and V. Rodriglvarez, *Comparison of evaporation rate and heat flow models for prediction of Liquefied Natural Gas (LNG) ageing during ship transportation.* Fuel, 2016. **177**: p. 87--106.
19. Miana, M., et al., *Calculation models for prediction of Liquefied Natural Gas (LNG) ageing during ship transportation.* Applied Energy, 2010. **87**(5): p. 1687--1700.
20. Wood, D.A. and M. Kulitsa, *Weathering/Ageing of Liquefied Natural Gas Cargoes During Marine Transport and Processing on Floating Storage Units and FSRU.* Journal of Energy Resources Technology, 2018. **140**(10).
21. Dobrota, D.J. and Lali, *Problem of boil-off in LNG supply chain.* Transactions on maritime science, 2013. **2**(02): p. 91--100.
22. Kountz, K.J., *Weathering of LNG in On-board Storage Tanks: Project Final Report, August 1997-April 1999*. 1999.
23. Chen, Q.S., J. Wegrzyn, and V. Prasad, *Analysis of temperature and pressure changes in liquefied natural gas (LNG) cryogenic tanks.* Cryogenics, 2004. **44**(10): p. 701--709.
24. Migliore, C., C. Tubilleja, and V. Vesovic, *Weathering prediction model for stored liquefied natural gas (LNG).* Journal of natural gas science and engineering, 2015. **26**: p. 570--580.
25. Lin, Y., et al., *An approach to estimating the boil-off rate of LNG in type C independent tank for floating storage and regasification unit under different filling ratio.* Applied Thermal Engineering, 2018. **135**: p. 463--471.
26. Krikkis, R.N., *A thermodynamic and heat transfer model for LNG ageing during ship transportation. Towards an efficient boil-off gas management.* Cryogenics, 2018. **92**: p. 76--83.
27. Qu, Y., et al., *A thermal and thermodynamic code for the*

computation of Boil-Off Gas--Industrial applications of LNG carrier. Cryogenics, 2019. **99**: p. 105--113.
28. Niu, W.C., et al., *The daily evaporation rate test and conversion method for a new independent type B LNG mock-up tank.* Cryogenics, 2020. **111**: p. 103168.
29. Rose, L., et al., *Integrated refrigeration and storage of LNG for compositional stability*. 2020. p. 012003.
30. Perez, F., et al., *Measurements of boil-off gas and stratification in cryogenic liquid nitrogen with implications for the storage and transport of liquefied natural gas.* Energy, 2021. **222**: p. 119853.
31. Al Ghafri, S.Z.S., et al., *Advanced boil-off gas studies for liquefied natural gas.* Applied Thermal Engineering, 2021. **189**: p. 116735.
32. Saleem, A., et al., *A CFD simulation study of boiling mechanism and BOG generation in a full-scale LNG storage tank.* Computers \& Chemical Engineering, 2018. **115**: p. 112--120.
33. Ferrn, J.L. and L.J. Prez-Prez, *Numerical simulation of natural convection and boil-off in a small size pressurized LNG storage tank.* Computers \& Chemical Engineering, 2020. **138**: p. 106840.
34. Shi, J.Q., C. Beduz, and R.G. Scurlock, *Numerical modelling and flow visualization of mixing of stratified layers and rollover in LNG.* Cryogenics, 1993. **33**(12): p. 1116--1124.
35. Jeon, G.-M., J.-C. Park, and S. Choi, *Multiphase-thermal simulation on BOG/BOR estimation due to phase change in cryogenic liquid storage tanks.* Applied Thermal Engineering, 2021. **184**: p. 116264.
36. Kulitsa, M. and D.A. Wood, *Rigorous monitoring reduce FSRU cargo-rollover risks.* Oil \& Gas Journal, 2017. **115**(6): p. 74--81.
37. Adom, E., S.Z. Islam, and X. Ji, *Modelling of boil-off gas in LNG tanks: A case study.* International journal of engineering and technology, 2010. **2**(4): p. 292--296.
38. Wang, Z., A. Sharafian, and W. Mrida, *Non-equilibrium thermodynamic model for liquefied natural gas storage tanks.* Energy, 2020. **190**: p. 116412.
39. Heestand, J., C.W. Shipman, and J.W. Meader, *A predictive model for rollover in stratified LNG tanks.* AIChE journal, 1983. **29**(2): p. 199--207.
40. Migliore, C., A. Salehi, and V. Vesovic, *A non-equilibrium approach to modelling the weathering of stored Liquefied*

Natural Gas (LNG). Energy, 2017. **124**: p. 684--692.
41. Arjomandnia, P., *Simulation of rollover in stratified LNG storage tanks*. 2010.
42. Wang, B., et al., *Thermal analysis and strength evaluation of cargo tanks in offshore FLNGs and LNG carriers*. 2013. p. V003T03A050.
43. Nicoletti, G., et al., *A technical and environmental comparison between hydrogen and some fossil fuels.* Energy Conversion and Management, 2015. **89**: p. 205-213.
44. Mekhilef, S., R. Saidur, and A. Safari, *Comparative study of different fuel cell technologies.* Renewable and Sustainable Energy Reviews, 2012. **16**(1): p. 981-989.
45. Bourgeois, T., et al., *The temperature evolution in compressed gas filling processes: A review.* International Journal of Hydrogen Energy, 2018. **43**(4): p. 2268-2292.
46. Liss, W.E., et al. *Development and Validation testing of Hydrogen fast-fill fueling algorithms*. in *Proceedings of 15th World Hydrogen Energy Conference*. 2004.
47. Committee, F.C.S., *Fueling Protocols for Light Duty Gaseous Hydrogen Surface Vehicles*. 2020, SAE International.
48. Committee, F.C.S., *Fueling Protocol for Gaseous Hydrogen Powered Heavy Duty Vehicles*. 2014, SAE International.
49. Parks, G., et al., *Hydrogen station compression, storage, and dispensing technical status and costs: Systems integration*. 2014, National Renewable Energy Lab.(NREL), Golden, CO (United States).
50. Reddi, K., A. Elgowainy, and E. Sutherland, *Hydrogen refueling station compression and storage optimization with tube-trailer deliveries.* International Journal of Hydrogen Energy, 2014. **39**(33): p. 19169-19181.
51. Dicken, C.J.B. and W. Mérida, *Modeling the Transient Temperature Distribution within a Hydrogen Cylinder during Refueling.* Numerical Heat Transfer, Part A: Applications, 2007. **53**(7): p. 685-708.
52. Dicken, C.J.B. and W. Mérida, *Measured effects of filling time and initial mass on the temperature distribution within a hydrogen cylinder during refuelling.* Journal of Power Sources, 2007. **165**(1): p. 324-336.
53. Woodfield, P.L., M. Monde, and Y. Mitsutake, *Measurement of Averaged Heat Transfer Coefficients in High-Pressure Vessel during Charging with Hydrogen, Nitrogen or Argon Gas.* Journal of Thermal Science and Technology, 2007. **2**(2): p.

180-191.
54. Bourgeois, T., et al., *Optimization of hydrogen vehicle refuelling requirements.* International Journal of Hydrogen Energy, 2017. **42**(19): p. 13789-13809.
55. Bourgeois, T., et al., *Evaluating the temperature inside a tank during a filling with highly-pressurized gas.* International Journal of Hydrogen Energy, 2015. **40**(35): p. 11748-11755.
56. Woodfield, P.L., M. Monde, and T. Takano, *Heat Transfer Characteristics for Practical Hydrogen Pressure Vessels Being Filled at High Pressure.* Journal of Thermal Science and Technology, 2008. **3**(2): p. 241-253.
57. Zheng, J., et al., *Experimental and numerical study on temperature rise within a 70 MPa type III cylinder during fast refueling.* International Journal of Hydrogen Energy, 2013. **38**(25): p. 10956-10962.
58. Rothuizen, E., et al., *Optimization of hydrogen vehicle refueling via dynamic simulation.* International Journal of Hydrogen Energy, 2013. **38**(11): p. 4221-4231.
59. Sadi, M. and M. Deymi-Dashtebayaz, *Hydrogen refueling process from the buffer and the cascade storage banks to HV cylinder.* International Journal of Hydrogen Energy, 2019. **44**(33): p. 18496-18504.
60. Elgowainy, A., et al., *Tube-trailer consolidation strategy for reducing hydrogen refueling station costs.* International Journal of Hydrogen Energy, 2014. **39**(35): p. 20197-20206.
61. Rothuizen, E. and M. Rokni, *Optimization of the overall energy consumption in cascade fueling stations for hydrogen vehicles.* International Journal of Hydrogen Energy, 2014. **39**(1): p. 582-592.
62. Xiao, L., et al., *Effects of pressure levels in three-cascade storage system on the overall energy consumption in the hydrogen refueling station.* International Journal of Hydrogen Energy, 2021. **46**(61): p. 31334-31345.
63. Yu, Y., et al., *Optimization on volume ratio of three-stage cascade storage system in hydrogen refueling stations.* International Journal of Hydrogen Energy, 2022. **47**(27): p. 13430-13441.
64. Opus-12. We have developed a device that recycles CO_2 into chemicals and fuels.
65. EVONIK. For a climate-friendly industry: Using carbon dioxide and hydrogen as raw materials for sustainable chemicals.

66. CERT. *CERT systems Inc.*
67. Voiry, D., et al., *Low−dimensional catalysts for hydrogen evolution and CO 2 reduction.* Nature Reviews Chemistry, 2018. **2**(1): p. 0105.
68. Sun, Z., et al., *Fundamentals and challenges of electrochemical CO2 reduction using two−dimensional materials.* Chem, 2017. **3**(4): p. 560−−587.
69. Sa, Y.J., et al., *Catalyst−−electrolyte interface chemistry for electrochemical CO 2 reduction.* Chemical Society Reviews, 2020. **49**(18): p. 6632−−6665.
70. Kim, K., et al., *Data−driven pilot optimization for electrochemical CO mass production.* Journal of Materials Chemistry A, 2020. **8**(33): p. 16943−−16950.
71. Zheng, T., et al., *Large−scale and highly selective CO2 electrocatalytic reduction on nickel single−atom catalyst.* Joule, 2019. **3**(1): p. 265−−278.
72. Li, F., D.R. MacFarlane, and J. Zhang, *Recent advances in the nanoengineering of electrocatalysts for CO 2 reduction.* Nanoscale, 2018. **10**(14): p. 6235−−6260.
73. Lee, C.W., et al., *Defining a materials database for the design of copper binary alloy catalysts for electrochemical CO2 conversion.* Advanced Materials, 2018. **30**(42): p. 1704717.
74. Dinh, C.−T., et al., *CO2 electroreduction to ethylene via hydroxide−mediated copper catalysis at an abrupt interface.* Science, 2018. **360**(6390): p. 783−−787.
75. De Arquer, F.P.G., et al., *CO2 electrolysis to multicarbon products at activities greater than 1 A cm− 2.* Science, 2020. **367**(6478): p. 661−−666.
76. Salvatore, D. and C.P. Berlinguette, *Voltage Matters When Reducing CO2 in an Electrochemical Flow Cell.* ACS Energy Letters, 2019. **5**(1): p. 215−−220.
77. Vennekoetter, J.−B., R. Sengpiel, and M. Wessling, *Beyond the catalyst: How electrode and reactor design determine the product spectrum during electrochemical CO2 reduction.* Chemical Engineering Journal, 2019. **364**: p. 89−−101.
78. Zhang, F., et al., *CO2 reduction in a microchannel electrochemical reactor with gas−liquid segmented flow.* Chemical Engineering Journal, 2020. **392**: p. 124798.
79. Zhang, Z., et al., *pH matters when reducing CO2 in an electrochemical flow cell.* ACS Energy Letters, 2020. **5**(10): p. 3101−−3107.
80. Duhn, J.D., et al., *Optimization of a new flow design for solid*

oxide cells using computational fluid dynamics modelling. Journal of Power Sources, 2016. **336**: p. 261--271.
81. Krastev, V.K., et al., *3D CFD modeling and experimental characterization of HT PEM fuel cells at different anode gas compositions.* International Journal of Hydrogen Energy, 2014. **39**(36): p. 21663--21672.
82. Macedo-Valencia, J., et al., *3D CFD modeling of a PEM fuel cell stack.* International journal of hydrogen energy, 2016. **41**(48): p. 23425--23433.
83. Park, J. and X. Li, *An experimental and numerical investigation on the cross flow through gas diffusion layer in a PEM fuel cell with a serpentine flow channel.* Journal of Power Sources, 2007. **163**(2): p. 853--863.
84. Nguyen, D.L.T., et al., *Mass transport control by surface graphene oxide for selective CO production from electrochemical CO2 reduction.* ACS Catalysis, 2020. **10**(5): p. 3222--3231.
85. Upadhyay, M., et al., *Systematic assessment of the anode flow field hydrodynamics in a new circular PEM water electrolyser.* International Journal of Hydrogen Energy, 2020. **45**(41): p. 20765--20775.
86. Weng, L.-C., A.T. Bell, and A.Z. Weber, *Towards membrane-electrode assembly systems for CO 2 reduction: a modeling study.* Energy \& Environmental Science, 2019. **12**(6): p. 1950--1968.
87. Weng, L.-C., A.T. Bell, and A.Z. Weber, *A systematic analysis of Cu-based membrane-electrode assemblies for CO 2 reduction through multiphysics simulation.* Energy \& Environmental Science, 2020. **13**(10): p. 3592--3606.
88. Plawsky, J.L., *Transport Phenomena Fundamentals, Third Edition*. 2014: Taylor & Francis.
89. Tijani, A.S., D. Barr, and A.H.A. Rahim, *Computational modelling of the flow field of an electrolyzer system using CFD.* Energy Procedia, 2015. **79**: p. 195--203.
90. Jung, B., et al., *Prediction model of LNG weathering using net mass and heat transfer.* Energy, 2022. **247**: p. 123325.
91. Churchill, S.W. and H.H.S. Chu, *Correlating equations for laminar and turbulent free convection from a vertical plate.* International journal of heat and mass transfer, 1975. **18**(11): p. 1323--1329.
92. Radziemska, E. and W.M. Lewandowski, *Heat transfer by natural convection from an isothermal downward-facing round*

plate in unlimited space. Applied Energy, 2001. **68**(4): p. 347--366.
93. Cengel, Y. and T.M. Heat, *A practical approach*. 2003.
94. Badam, V.K., et al., *Experimental and theoretical investigations on interfacial temperature jumps during evaporation.* Experimental thermal and fluid science, 2007. **32**(1): p. 276--292.
95. GIIGNL, *Lng custody transfer handbook*. sixth ed. 2021.
96. Kunz, O. and W. Wagner, *The GERG-2008 wide-range equation of state for natural gases and other mixtures: an expansion of GERG-2004.* Journal of chemical \& engineering data, 2012. **57**(11): p. 3032--3091.
97. Peng, D.-Y. and D.B. Robinson, *A new two-constant equation of state.* Industrial \& Engineering Chemistry Fundamentals, 1976. **15**(1): p. 59--64.
98. Lemmon, E., et al., *NIST Standard Reference Database 23: Reference Fluid Thermodynamic and Transport Properties-REFPROP, Version 10.0, National Institute of Standards and Technology.* Standard Reference Data Program, Gaithersburg, 2018.
99. Koretsky, M.D., *Engineering and chemical thermodynamics*. 2012: John Wiley & Sons.
100. Maurice, S., *9 - Reciprocating compressors*, in *Surface Production Operations*, S. Maurice, Editor. 2019, Gulf Professional Publishing: Boston. p. 655-778.
101. Phillippi, G. *Basic thermodynamics of reciprocating compression*. in *Proceedings of the 45th Turbomachinery Symposium*. 2016. Turbomachinery Laboratories, Texas A&M Engineering Experiment Station.
102. Smith, R., *Chemical process: design and integration*. 2005: John Wiley & Sons.
103. Elgowainy, A., et al., *Techno-economic and thermodynamic analysis of pre-cooling systems at gaseous hydrogen refueling stations.* International Journal of Hydrogen Energy, 2017. **42**(49): p. 29067-29079.
104. Kuroki, T., et al., *Dynamic simulation for optimal hydrogen refueling method to Fuel Cell Vehicle tanks.* International Journal of Hydrogen Energy, 2018. **43**(11): p. 5714-5721.
105. Bai, Y., et al., *Modeling and optimal control of fast filling process of hydrogen to fuel cell vehicle.* Journal of Energy Storage, 2021. **35**.
106. Irani, R., *Hydrogen storage: high-pressure gas containment.*

MRS bulletin, 2002. **27**(9): p. 680-682.
107. San Marchi, C., et al., *Pressure cycling of type 1 pressure vessels with gaseous hydrogen.* 2011.
108. Barthélémy, H. and A. Agnoletti, *Cylinders and Tubes Used as Buffers in Filling Stations.* 2015.
109. Chen, T.-P., *Hydrogen delivey infrastructure option analysis.* 2010, Nexant, Inc., 101 2nd St., San Fancisco, CA 94105.
110. Jung, B., et al., *Design methodology for mass transfer-enhanced large-scale electrochemical reactor for CO2 reduction.* Chemical Engineering Journal, 2021. **424**: p. 130265.
111. Suresh, P.V., et al., *An improved serpentine flow field with enhanced cross-flow for fuel cell applications.* International journal of hydrogen energy, 2011. **36**(10): p. 6067--6072.
112. Xu, C. and T.S. Zhao, *A new flow field design for polymer electrolyte-based fuel cells.* Electrochemistry communications, 2007. **9**(3): p. 497--503.
113. Wang, X.-D., et al., *Effects of flow channel geometry on cell performance for PEM fuel cells with parallel and interdigitated flow fields.* Electrochimica Acta, 2008. **53**(16): p. 5334--5343.
114. Fedkiw, P.S., *Mass transfer controlled reactions in packed beds at low Reynolds numbers.* 1978.
115. Bhargava, S.S., et al., *System design rules for intensifying the electrochemical reduction of CO2 to CO on Ag nanoparticles.* ChemElectroChem, 2020.
116. Endrődi, B., et al., *Multilayer electrolyzer stack converts carbon dioxide to gas products at high pressure with high efficiency.* ACS energy letters, 2019. **4**(7): p. 1770--1777.
117. Jiang, K., et al., *Silver nanoparticles with surface-bonded oxygen for highly selective CO2 reduction.* ACS Sustainable Chemistry \& Engineering, 2017. **5**(10): p. 8529--8534.
118. Murawski, E., et al., *Decreased gas-diffusion electrode porosity due to increased electrocatalyst loading leads to diffusional limitations in cathodic H2O2 electrosynthesis.* Journal of Power Sources, 2021. **481**: p. 228992.
119. Ma, M., et al., *Selective and efficient reduction of carbon dioxide to carbon monoxide on oxide-derived nanostructured silver electrocatalysts.* Angewandte Chemie, 2016. **128**(33): p. 9900--9904.
120. Xu, Y., et al., *Self-Cleaning CO2 Reduction Systems: Unsteady Electrochemical Forcing Enables Stability.* ACS Energy

Letters, 2021. **6**(2): p. 809--815.
121. Nwabara, U.O., et al., *Durable cathodes and electrolyzers for the efficient aqueous electrochemical reduction of CO2.* ChemSusChem, 2020. **13**(5): p. 855--875.

Abstract in Korean (국문초록)

이 논문은 에너지 산업의 설계 방법론과 검증을 다룬다. 지속 가능한 에너지 자원을 확보하고 기후 변화를 대응하기 위해 화석 연료에서 재생 에너지로의 에너지 패러다임 전환이 진행되고 있다. 에너지 전환 중간 단계로써, 본 논문은 저탄소 에너지 시스템에서 발생하는 이동 현상을 화학 공정 시스템 공학의 관점에서 예측하기 위한 적절한 수치 시뮬레이션 모델 개발에 중점을 두었다. 개발된 각 모델은 측정된 데이터로 검증되었으며 각 시스템의 설계 방법론 개발에 적용되었다. 여기에는 1차원 액화천연가스 풍화 예측 모델, 수소 충전 시스템의 0차원 동적 시뮬레이션 모델, 이산화탄소 전기화학적 환원 유로의 3차원 전산 유체 역학 모델이 포함되었다.

액화천연가스 저장탱크에서는 증발가스가 발생하여 시간이 지남에 따라 액화천연가스의 조성이 변화하는데 이를 액화천연가스 풍화라고 한다. 이는 전체 액화천연가스의 가치사슬을 설계하는 데 있어 가장 중요한 특성이다. 액화천연가스는 탱크 내에서 비평형 상태로 존재하기 때문에 이 현상을 분석하기 위해 질소와 탄화수소가 담긴 대규모 탱크 (50 m^3)에서 등압 운전 하에 장기간 (50일) 실험을 수행했다. 그리고 본 연구에서는 기상 모델링을 배제한 액화천연가스 풍화의 1차원 예측 모델을 제안했다. 측정된 기상 온도는 열성층화로 인해 전체 기상을 나타낼 수 없기 때문에 대규모 탱크에서 계면에서의 열전달 및 열역학적 평형을 엄밀

하게 정량화 하는 것은 어렵다. 따라서, 접근을 용이하게 하기 위해 액화천연가스 터미널에서 도출된 경험적 기−액체 평형 상수와 온도 항을 압력으로 변환하는 통계 속도 이론을 도입하여 순 질량전달을 계산하고 계면에서의 순 열전달도 도입했다. 개발된 모델은 실험 데이터로 검증되었으며 실험과 좋은 일치를 보였다. 개발된 모델을 통해 기존 접근 방식의 편차를 발견하고 증발가스 생성 매개변수(c)와 평형 상수(K_{N_2})를 사용하여 다양한 시나리오에 예측 모델을 적용하는 설계 방법론을 제안했다.

연료전지 전기차의 수요 증가에 대응하기 위해 최적화된 수소 충전 설비 및 관련 인프라를 전국에 보급해야 할 필요성이 대두되고 있다. 따라서 본 연구에서는 주요 수소충전설비 구성요소에 대한 설계변수의 복잡한 상호의존성을 살펴보았다. 수소충전설비의 성능을 평가하기 위해 수소 충전 탱크 및 버퍼 저장 탱크의 압력을 회복하는 것이 포함된 수소충전설비 전체 공정을 0차원 동적 시뮬레이션 모델로 개발했다. 개발된 모델은 한국의 실제 수소충전설비 운영 데이터에 의해 검증되었다. 그리고 본 연구에서는 모든 실질 제약조건을 고려하여 자본 및 운영 비용을 줄이기 위한 새로운 설계 방법론을 제안했다. 첫째, 미리 정의된 수소충전설비와 차량의 사양에 따라 압축기는 충전 수요 및 수소 공급원의 가용 압력을 가지고 크기가 결정되며, 버퍼 저장 탱크 용량의 크기를 줄이기 위해 압축기는 차량 충전 중에 작동할 수 있게 설계한다. 다음으로, 버퍼 저장 시스템은 에너지 소비를 줄이고 완전한 연속 충전을 위해 5가

지 변수로 설계된다. 마지막으로, 고압탱크는 압축기의 성능에 따라 연속 충진 시나리오에서 어느 정도 회복되기 때문에 저압 탱크의 크기를 키우는 것에 중점을 둘 필요가 있다.

이산화탄소를 가치 있는 화학 물질로 전기화학적 전환하는 것은 온실가스를 줄이는 지속 가능한 화학 물질 생산 방법이자 재생 에너지 공급 및 수요 불일치를 해결하기 위한 잠재적인 방안이다. 본 연구에서는 3차원 전산 유체 역학 모델을 개발하여 CO 생산 속도를 개선하기 위한 물질 전달에 대한 유로의 영향을 정량화했다. 그리고 전산 유체 역학 기법으로 설계한 유로를 바탕으로 대규모 전기화학적 이산화탄소 환원반응기에서 일산화탄소의 생성 속도를 실험적으로 측정하고, pH와 계면을 변화시켜 물질 전달 속도를 촉진시키는 다른 외재적 특성을 살펴보는 실험도 수행하였다. 연구 결과는 대류 물질 전달이 생산 속도를 향상시킴을 보여주었고, 대규모 전기화학 반응기의 유로 설계에 대한 일반적인 지침으로 가스확산층을 통한 대류 물질 전달을 최대화하고 반응기 내 흐름을 균일하게 유지하는 것을 제안한다.

주요어: 에너지, 액화천연가스, 수소, 이산화탄소, 모델링, 설계방법론, 검증

학번: 2016-21139